Rotational Structures and High-K Isomerism in ^{248,250}Fm

by
Steffen Ketelhut

Academic Dissertation
for the Degree of
Doctor of Philosophy

To be presented, by permission of the
Faculty of Mathematics and Natural Sciences
of the University of Jyväskylä,
for public examination in Auditorium FYS-1 of the
University of Jyväskylä on December 3, 2010
at 12 o'clock noon

Jyväskylä, Finland
December 2010

Preface

The last five years have been an interesting and challenging time for me, coming as a foreign student to a Finnish research group. There have been many people who contributed to this work with their knowledge and experience, and helped me in adapting to the international working environment and Finnish lifestyle. Even if not mentioned personally, I am thankful to all of them.

I want to thank Professor Rauno Julin for taking me as part of his group, showing interest in my work, and giving me all the support I could wish for during the last five years. A warm thank you goes to my supervisor Research Professor Paul Greenlees. Thank you for sharing your knowledge on superheavy elements, for patience with my numerous questions, and for your support and guidance throughout the work. Furthermore, I would like to thank all the present and former group members of both the GAMMA and RITU groups, for their guidance, help and company, for providing answers to my questions, fruitful discussions and creating a nice working atmosphere. It has been a pleasure to work with you.

I am grateful to the reviewers Dr. Paul Campbell and Dr. Filip Kondev for their careful reading of the manuscript. Dr. Mikael Sandzelius is acknowledged for his critical proofreading.

The work on physics would be only half as efficient, if it would not be possible to get away from it from time to time. Asta, Maria, Mia, Sonja, Sanni, Sari, Ville, thank you for making Jyväskylä a nice place to live in.

Vielen Dank an meine Familie, insbesondere an meine Eltern Rüdiger und Heike, für ihre Unterstützung in all den Jahren. Finally, a warm thanks to Raisa for standing by my side, thank you for your support and encouragement during this time.

Jyväskylä, December 2010

Steffen Ketelhut

Author   Steffen Ketelhut
                  Department of Physics
                  University of Jyväskylä
                  Finland

Supervisors   Research Prof. Paul Greenlees
                  Department of Physics
                  University of Jyväskylä
                  Finland

                  Prof. Rauno Julin
                  Department of Physics
                  University of Jyväskylä
                  Finland

Reviewers   Dr. Paul Campbell
                  Schuster Laboratory
                  School of Physics and Astronomy
                  University of Manchester
                  United Kingdom

                  Dr. Filip Kondev
                  Physics Division
                  Argonne National Laboratory
                  USA

Opponent   Dr. David Jenkins
                  Department of Physics
                  University of York
                  United Kongdom

Abstract

The fermium isotopes ^{248}Fm and ^{250}Fm have been investigated in two experiments at the Accelerator Laboratory of the University of Jyväskylä. Both in-beam and focal-plane spectroscopy have been carried out using the germanium detector array JUROGAM at the target position and the spectrometer GREAT at the focal plane of the gas-filled recoil-separator RITU. The combination of JUROGAM with RITU and GREAT allowed for the powerful recoil-gating, recoil-alpha and recoil-electron tagging techniques to be applied. Isomer identification was possible by measuring the summed energies of electrons from highly converted transitions.

The rotational ground-state band in ^{248}Fm has been established for the first time, and that in ^{250}Fm could be extended up to spin $I = 22$. In ^{250}Fm, two isomeric states with half lives of 1.92(5) s and 8(2) μs have been measured, and the exact decay path of the longer-lived isomer could be reconstructed. Furthermore, a rotational band on top of the 1.92(5) s isomeric state was found. The 1.92 s isomer was assigned a 8^- $(7/2^+[624]_\nu \otimes 9/2^-[734]_\nu)$ two-quasiparticle configuration. In ^{248}Fm, one isomeric state has been measured with a half life of 10.1(6) ms.

A comparison is made of rotational bands and K isomers in ^{248}Fm and ^{250}Fm and other nuclei in the region, and also with theoretical calculations. Anomalities in the systematics at $Z = 98$ are discussed.

Publications

The author has also been involved and played a leading role in the production of the following publications related to the theme of this thesis:

Refereed Articles:

1. *γ-ray Spectroscopy at the Limits: First Observation of Rotational Bands in ^{255}Lr*
   S. Ketelhut, P.T. Greenlees, D. Ackermann, S. Antalic, E. Clement, I.G. Darby, O. Dorvaux, A. Drouart, S. Eeckhaudt, B.J.P. Gall, A. Görgen, T. Grahn, C. Gray-Jones, K. Hauschild, R.-D. Herzberg, F.P. Heßberger, U. Jakobsson, G.D. Jones, P. Jones, R. Julin, S. Juutinen, T.-L. Khoo, W. Korten, M. Leino, A.-P. Leppänen, J. Ljungvall, S. Moon, M. Nyman, A. Obertelli, J. Pakarinen, E. Parr, P. Papadakis, P. Peura, J. Piot, A. Pritchard, P. Rahkila, D. Rostron, P. Ruotsalainen, M. Sandzelius, J. Saren, C. Scholey, J. Sorri, A. Steer, B. Sulignano, Ch. Theisen, J. Uusitalo, M. Venhart, M. Zielinska, M. Bender, and P.-H. Heenen
   Phys. Rev. Lett. **102**, 212501 (2009)

2. *High-K Structure in ^{250}Fm and the deformed shell gaps at N=152 and Z=100*
   P.T. Greenlees, R.-D. Herzberg, **S. Ketelhut**, P.A. Butler, P. Chowdhury, T. Grahn, C. Gray-Jones, G.D. Jones, P. Jones, R. Julin, S. Juutinen, T.-L. Khoo, M. Leino, S. Moon, M. Nyman, J. Pakarinen, P. Rahkila, D. Rostron, J. Saren, C. Scholey, J. Sorri, S.K. Tandel, J. Uusitalo, and M. Venhart
   Phys. Rev. C **78**, 021302(R) (2008)

3. *Nuclear isomers in superheavy elements as stepping stones towards the island of stability*
   R.D. Herzberg, P.T. Greenlees, P.A. Butler, G.D. Jones, M. Venhart, I.G. Darby, S. Eeckhaudt, K. Eskola, T. Grahn, C. Gray-Jones, F.P. Heßberger, P. Jones, R. Julin, S. Juutinen, **S. Ketelhut**, W. Korten, M. Leino, A.-P. Leppanen, S. Moon, M. Nyman, R.D. Page, J. Pakarinen, A. Pritchard, P. Rahkila, J. Saren, C. Scholey, A. Steer, Y. Sun, C h. Theisen, J. Uusitalo
   Nature **442**, 896-899 (2006)

Conference proceedings:

1. *Spectroscopy of odd-proton nuclei in the region of ^{254}No*
   S. Ketelhut, P.T. Greenlees, A. Chatillon, E. Bouchez, P.A. Butler, E. Clement, O. Dorvaux, S. Eeckhaudt, B.J.P. Gall, A. Görgen, T. Grahn, R.-D. Herzberg, F.P. Heßberger, A. Hurstel, P. Jones, R. Julin, S. Juutinen, H. Kettunen, F. Khalfallah, W. Korten, Y. Le Coz, M. Leino, A.-P. Leppänen, S. Moon, P. Nieminen, M. Nyman,

J. Pakarinen, J. Perkowski, P. Rahkila, M. Rousseau, J. Saren, C. Scholey, Ch. Theisen, J. Uusitalo, J.N. Wilson, P. Bonche, P.-H. Heenen

(FINUSTAR 2 Conference Proceedings)

AIP Conf. Proc 1012, 368 (2008)

2. *Spectroscopy of Very Heavy Elements*

P.T. Greenlees, R.-D. Herzberg, **S. Ketelhut**, D. Ackermann, P.A. Butler, A. Chatillon, S. Eeckhaudt, B.J.P. Gall, T. Grahn, C. Gray-Jones, A. Görgen, F.P. Heßberger, U. Jakobsson, G.D. Jones, P. Jones, R. Julin, S. Juutinen, T.-L. Khoo, W. Korten, M. Leino, S. Moon, M. Nyman, J. Pakarinen, P. Papadakis, P. Peura, P. Rahkila, M. Richer, D. Rostron, C. Santos, J. Saren, C. Scholey, J. Sorri, S.K. Tandel, Ch. Theisen, J. Uusitalo, M. Venhart

(FINUSTAR 2 Conference Proceedings)

AIP Conf. Proc 1012, 56 (2008)

3. *Bridging the nuclear structure gap between stable and super heavy nuclei*

D. Seweryniak, T.L. Khoo, I. Ahmad, F.G. Kondev, A. Robinson, S.K. Tandel, M. Asai, B.B. Back, M.P. Carpenter, P. Chowdhury, C.N. Davids, S. Eeckhaudt, J.P. Greene, P.T. Greenlees, S. Gros, K. Hauschild, A. Heinz, R.-D. Herzberg, R.V.F. Janssens, D.G. Jenkins, G.D. Jones, **S. Ketelhut**, T. Lauritsen, C.J. Lister, A. Lopez-Martens, P. Marley, E.A. McCutchan, T. Nakatsukasa, P. Papadakis, D. Peterson, J. Qian, D. Rostron, I. Stefanescu, U.S. Tandel, X.F. Wang and S.F. Zhu

Nuclear Physics A **834**, 357c (2010)

Contents

List of Figures

List of Tables

Nomenclature

ADC   Analog-to-Digital Converter

ANL   Argonne National Laboratory

BGO   Bismuth Germanate

CFD   Constant Fraction Discriminator

DSSSD   Double-Sided Silicon Strip Detector

ENSDF   Evaluated Nuclear Structure Data File

FLNR   Flerov Laboratory of Nuclear Reactions

FMA   Fragment Mass Analyzer

FWHM   Full Width at Half Maximum

GSI   Gesellschaft für Schwerionenforschung

HFB   Hartree-Fock Bogoliubov

HPGe   High-Purity Germanium

JYFL   Jyväskylän Yliopiston Fysiikan Laitos (Department of Physics of the University of Jyväskylä)

LBNL   Lawrence Berkeley National Laboratory

MMM   Macroscopic-Microscopic Model

MWPC   Multi-Wire Proportional Counter

PHD   Pulse Height Defect

PTR   Peak-to-Total Ratio

RDT   Recoil-Decay Tagging

SHARC   Super Harvard Architecture Single-Chip Computer

SHE   Super-Heavy Elements

TDR   Total Data Readout

TFA	Timing Filter Amplifier
VME	Virtual Machine Environment
VXI	VME eXtensions for Instrumentation
DGFRS	Dubna Gas-Filled Recoil Separator
RITU	Recoil Ion Transport Unit
SASSY	Small Angle Separator System

Chapter 1

Introduction

The nuclear shell model was established in 1949 independently by Maria Goeppert-Mayer and Haxel, Jensen and Suess [1,2]. The model was able to explain shell closures, the so-called magic numbers, at $Z = 2, 8, 20, 28, 50, 82$, for protons, and at $N = 2, 8, 20, 28, 50, 82, 126$, for neutrons. A large amount of systematic data had to be collected before the final pattern emerged, which is why Maria Goeppert-Mayer said, that the finding of the shell model was based on the experimentalists approach [3]. The question arises of where the next shell closures are situated, if there are any. *How heavy can a nucleus be without fissioning spontaneously?* This question can be rephrased: *How do nuclear properties change for very heavy systems?*

Even if clear gaps would appear in the single-particle levels of superheavy elements (SHE), the concept of "magic" numbers is questionable for the heaviest nuclei. The binding energy of a nucleus, and thus its stability, can be expressed by a liquid drop term and a shell correction term, as explained in Section 2.1.3. For light nuclei, the shell effects are strongest at the position of the shell closures, where the level density is lowest, and therefore, there is a direct relation between stability and gaps in the level scheme. In heavy elements, single-particle levels with high spin j occur. If those are situated close to the Fermi surface together with levels of lower spin, the difference in degeneracies of the levels causes a drop in single-particle level density, which again causes a large shell correction without gaps in the level spacing [4]. For example, in the region of proton levels around $Z = 120$, where the next magic number is expected, levels with the harmonic shell quantum numbers $2f_{7/2}$, $2f_{5/2}$, $3p_{3/2}$, and $3p_{1/2}$ are surrounded by levels with $1i_{13/2}$, $1i_{11/2}$, and $1j_{15/2}$, as is illustrated in Figure 1.1. The shell effect caused by the drop in degeneracies is of the same order of magnitude as the one caused by gaps in the spectrum. A region of enhanced shell stabilisation arises, and distinct gaps in stability are washed out.

Despite this difficulty, theoretical predictions have been made based on the single-particle structure. They are still contradictory and give values for the proton magic number ranging from 114 for most macroscopic-microscopic models [5] to 120 and 126 for most relativistic and non-relativistic nuclear mean-field calculations [6,7]. The neutron magic number is predicted to be 184, with some parameterisations favouring 172 instead.

One difficulty in predicting gaps in the energy level systematics of SHE resides in the strength of the spin-orbit coupling, which has direct consequences for the level ordering. The influence of the spin-orbit splitting is larger in SHE than in lighter nuclei, because the level density is higher, and because the splitting is proportional to $2l+1$ and thus favours high-spin states, which are more abundant in heavier systems. Nilsson and Ragnarsson found a further
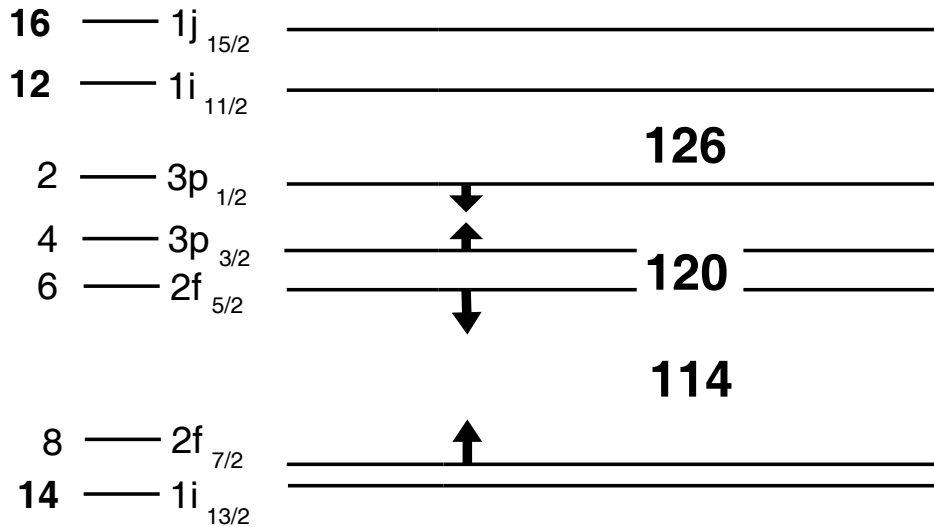
Figure 1.1: Degeneracy and spin-orbit coupling of the proton levels in the region of $Z = 114 - 126$. The level spacing is based on HFB calculations with SkI4 parametrisation for the nucleus $^{310}126_{184}$ [4]. The influence of a reduced spin-orbit force is shown by arrows. On the left the level assignment and level degeneracy is given. High degeneracy is marked by bold letters, illustrating the region of reduced single-particle level density between $Z = 114$ and $Z = 126$.

non-trivial dependence of the splitting on the position of the nucleus in the nuclear chart. They included this dependency by fitting the spin-orbit strength parameter depending on the oscillator-shell quantum-number N [8]. This causes an uncertainty when extrapolating into the unknown region of SHE, but only influences the width of the gap at $Z = 114$ and $N = 184$ in the macroscopic-microscopic models. A comparison of the single-particle structures for different non-relativistic and relativistic parametrisations in self-consistent models was given by Bender *et al.* [7]. In particular, they determine the density-distribution of the nuclear matter not to be flat in the centre, which feeds back to the spin-orbit potential in the self-consistent models. As a consequence, the spin-orbit coupling of the low-j $3p_{3/2}$ and $3p_{1/2}$ orbitals is much reduced in comparison to the high-j $2f_{7/2}$, $2f_{5/2}$ orbitals. Furthermore, some parametrisations underestimate the splitting by as much as 80 % for the doubly-magic ^{208}Pb, as they are adjusted for ^{16}O.

In Figure 1.1, the influence of spin-orbit splitting on the level structure is schematically demonstrated in the region around $Z = 114 - 126$. Spin-orbit partners are $2f_{7/2}$ and $2f_{5/2}$, $3p_{3/2}$, and $3p_{1/2}$ and $1i_{13/2}$, and $1i_{11/2}$. In the particular calculation the levels are ordered such that a shell closure appears at $Z = 114$. Depending on the strength of the spin-orbit spitting other shell closures might open up at $Z = 120$ or $Z = 126$ instead.

In experiments, nuclei up to $Z = 118$ and $N = 177$ have been synthesised at FLNR in Dubna, Russia, at GSI in Darmstadt, Germany, at RIKEN in Japan, and at LBNL in Berkeley, USA. The even-even nuclei $^{290}116$ and $^{294}118$ could be produced at FLNR with cross sections of $\sigma = 3.7^{+2.1}_{-1.8}$pb and $\sigma = 0.5^{+1.6}_{-0.3}$pb, respectively [9]. The decrease in cross section is interpreted as a decrease in survival probability caused by a lower fission barrier, which indicates a proton magic number below $Z = 118$. Recently, two isotopes of element 117 were found. $^{294}117$ and $^{293}117$ have cross sections of $\sigma = 0.5^{+1.1}_{-0.4}$pb and $\sigma = 1.3^{+1.5}_{-0.6}$pb,

respectively [10]. In this case, systematic studies of the α decay Q value and half life point towards a magic neutron number of $N > 177$. Anyway, these results are to be taken with care. Systematic data is scarce, and only basic properties like α decay half life and energy and cross sections are known. Furthermore, the data is subject to statistical and systematic uncertainties, one of which is the possible occurence of shape isomers in the vicinity of doubly-magic nuclei [11].

In contrast to the SHE, isotopes in the region of ^{248,250}Fm can be produced with relatively high cross sections, as is explained in Section 3.1. For example, the reaction ^{208}Pb$(^{48}$Ca, 2n$)^{254}$No has a cross section of 3 μb, which is six orders of magnitude higher than the ones to produce the heaviest nuclei. This allows extensive spectroscopy of structure phenomena, which are inaccessible or hardly accessible for heavier nuclei, and gives valuable input to the models describing SHE. Single-particle and collective properties such as spin, parity, energy and ordering of single-particle levels, configuration of many-quasiparticle excitations, and rotational bands with moment of inertia and deformation can be investigated for a wide range of nuclei.

Figure 1.2 presents details ofthe Nilsson diagram of Figure 2.3 and 2.4. Particular Nilsson orbitals are highlighted, which are close to the Fermi surface in ^{248,250}Fm. Deformation of nuclei in this region is $\epsilon \approx 0.25 - 0.3$ (see for example [13–15] for measurements), and deformed shell closures appear for neutrons at $N = 152$ and protons at $Z = 100$. The nucleus ^{252}Fm is thus a deformed doubly-magic nucleus in this particular calculation. It should be noted that the Nilsson levels are shifted for other calculations. Chatillon *et al.* present in their article a Hartree-Fock Bogoliubov (HFB) calculation using the SLy4 parametrisation [16]. In this calculation, deformed shell gaps appear at $Z = 98, 104$ and $N = 150$, and no gaps are visible at $Z = 100$ ad $N = 152$. The single-particle structure of neighbouring nuclei will shed light on the question, if and where the deformed shell closures are positioned.

Recently, spectroscopy in the fermium region has mainly been performed in three ways: Prompt spectroscopy of rotational bands, fine-structure α decay studies and delayed spectroscopy from isomeric states [17]. In this work, two of the three are applied, rotational bands and K-isomeric states are investigated using the techniques described in Section 3.3.

K-isomer spectroscopy gives direct insight into the single-particle structure close to the Fermi surface. In ^{250}Fm and ^{254}No, K isomers were found in 1973 by Ghiorso *et al.* [18]. A half life of 1.8(1) s was assigned to the isomeric state of ^{250}Fm and 0.28(2) s to the ^{254}No isomer. The isomers were suggested to form two-quasiparticle excitations with high K quantum number, but the exact energy and spin could not be observed in this experiment. The isomer in ^{254}No was confirmed in 2005 by Butler *et al.* and Mukherjee *et al.* by electron spectroscopy [19, 20]. In 2006, Herzberg *et al.* established the full decay path by applying the electron tagging method explained in Section 3.3 [21]. It was found to be a $K^{\pi} = 8^-$ isomer with a half life of 266(2) ms, within error bars similar to the result of Ghiorso *et al.*. The excitation energy is measured to be 1293 keV. The isomer has the two-quasiproton configuration $9/2^+[624]_{\pi} \otimes 7/2^-[514]_{\pi}$, and decays via a $K^{\pi} = 3^+$ intermediate band to the ground state. The confirmation and exact delineation of the decay path in ^{254}No started further investigation of isotopes in this area. The K isomers which have been found to date are marked in Figure 1.3. The figure includes the two isotopes ^{248,250}Fm investigated in this work.

From rotational bands, information on the moment of inertia and quadrupole moment can be deduced, and it can be used to test collective properties of theoretical models. Using recoil-decay tagging (RDT) combined with in-beam γ ray spectroscopy (see Section 3.3), bands
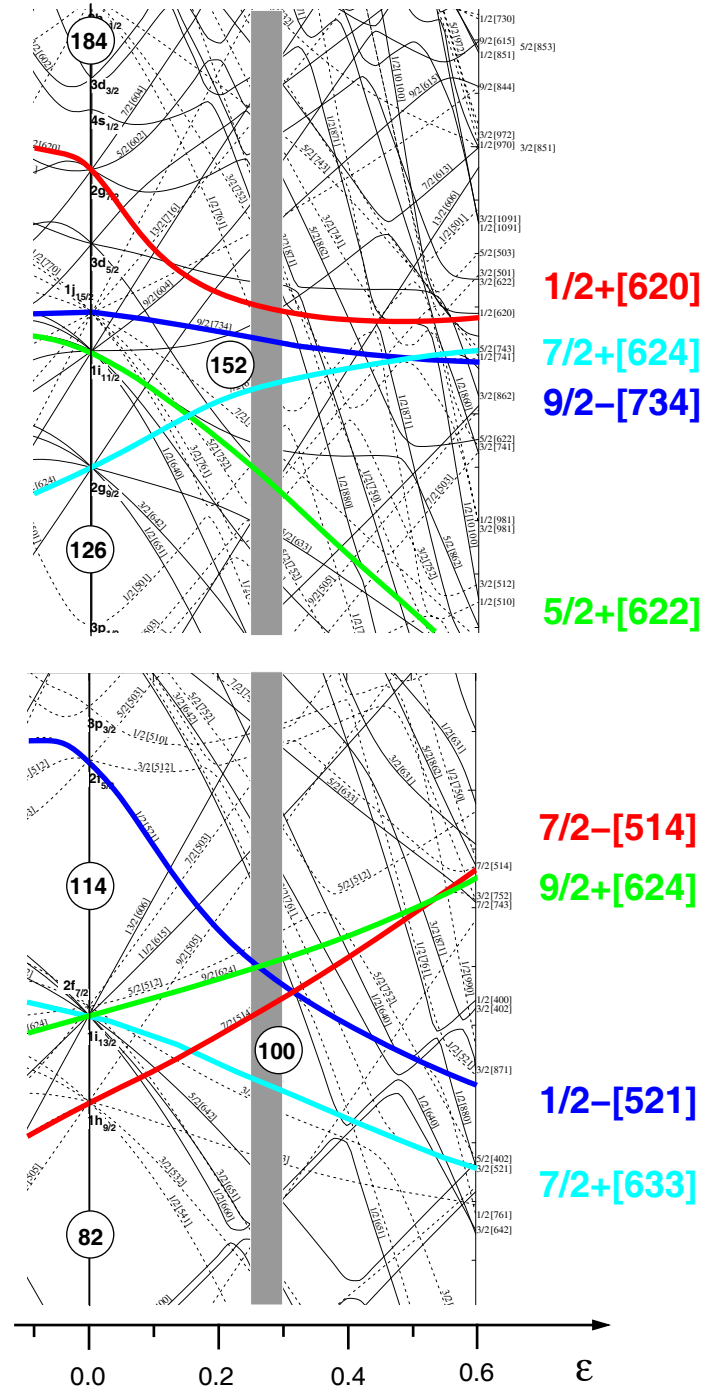
Figure 1.2: Detail of the Nilsson diagram for neutrons (upper figure) and protons (lower figure). The Nilsson diagram is taken from [12]. Orbitals close to the Fermi surface of ^{248,250}Fm are highlighted in different colours. Proposed spherical shell gaps at $N = 126, 184$ and $Z = 82, 114$ and deformed shell gaps at $Z = 100$ and $N = 152$ are indicated in the figure. The shaded grey part indicates the deformation of isotopes in the region around ^{254}No and ^{248,250}Fm. For detailed Nilsson diagrams see Figures 2.3 and 2.4.
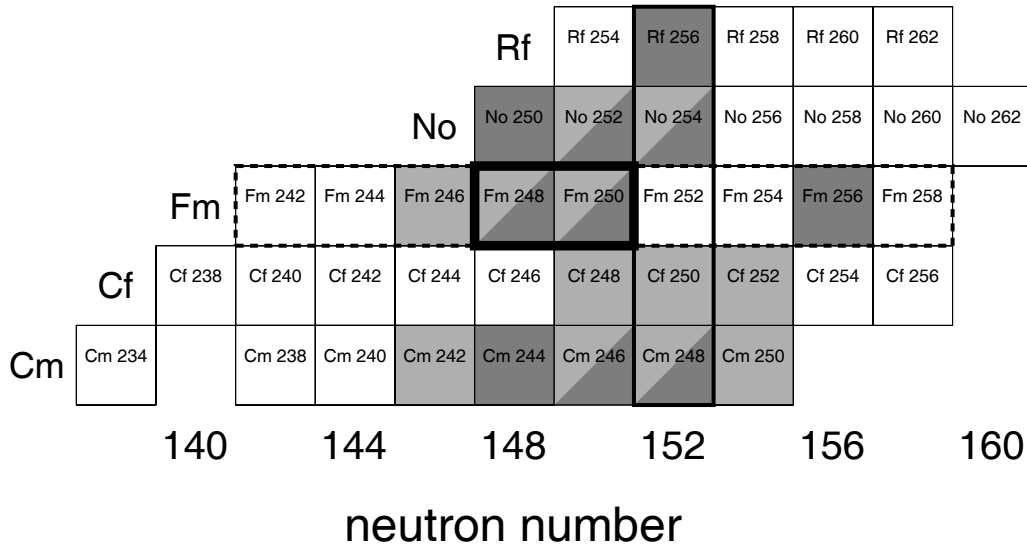
Figure 1.3: Detail of the Chart of Nuclides for even-even nuclei in the ^{254}No region. Isotopes with known K isomers are marked in dark grey. Isotopes in which rotational bands have been found in in-beam experiments, are marked in light grey. ^{248}Fm and ^{250}Fm are highlighted by a black box. For a detailed list of K isomers in the region and references see Table 5.4. References for ground-state bands can be found in the text.

in the even-even isotopes ^{254}No, ^{252}No, and ^{250}Fm [13–15, 22] and in the odd-even isotopes ^{251}Md, ^{253}No, and ^{255}Lr [23–26] have been found prior to this work. Furthermore, a rotational band in ^{246}Fm has recently been observed at the Accelerator Labratory of Jyväskylä [27]. At RIKEN in Japan, an alternative in-beam spectroscopy technique was used implementing transfer reactions, and selecting the channel of interest by analysing the scattered projectile in a Si $\Delta E - E$ telescope. In this way, rotational bands were found in the somewhat lighter, neutron-rich nuclei ^{236}Th, ^{240,242}U, ^{245,246}Pu, ^{250}Cm, and ^{248,250,252}Cf [28–32]. At ANL in Argonne, the rotational bands in ^{242}Cm, ^{246}Cm, and ^{248}Cm have been established by using Coulomb excitation and transfer reactions [33, 34]. The rotational bands in even-even nuclei in the region of ^{254}No found by in-beam γ ray spectroscopy are marked in Figure 1.3.

This work reports on the confirmation of K isomerism in ^{250}Fm, published in [35], and on a new isomer which has been found in ^{248}Fm. Furthermore, the rotational band in ^{248}Fm has been established for the first time, and the ground-state band of ^{250}Fm extended.

The text is divided into five parts: An introduction and motivation is given in this chapter. In the second chapter, the theoretical background is covered. This is followed in the third chapter by an introduction to the experimental methods and devices, which have been used in this work. In chapter four, the results of the data analysis are presented, which are discussed in chapter 5. Finally, a short summary and outlook are given in chapter 6.

Chapter 2

Theoretical Background

In this chapter the physics background to the following work is given. The first section gives a general introduction to the theoretical models used to describe properties of nuclei in the heavy and superheavy region. In Section 2.2, electromagnetic decay is discussed, including transition probabilities in the one-particle and collective case, selection rules, and internal conversion. Section 2.3 covers rotation, which is possible for deformed nuclei, and can be studied in terms of the moments of inertia. Magnetic dipole and electric quadrupole moments are described in Section 2.4. Finally, the nuclear g factor and isomerism in nuclei is discussed in Section 2.5, with focus on K isomerism, which is subject of this thesis. This section is based on references [36], [8], [37], and [38].

2.1 Nuclear Models

Different theories are used to predict the next magic shell closures and the properties of superheavy and heavy elements. The models are shortly introduced in this section, to give the background to these calculations and understand their ability and limitations in predicting nuclear properties.

The spherical shell model including a spin-orbit term was the first to successfully reproduce the known magic numbers for protons and neutrons. This model was extended to deformed shapes by the Nilsson model. Realistic level energies can be obtained by extending the shell model by the Strutinsky method, which is realised in the macroscopic-microscopic models. Self-consistent models use a variational approach instead by applying the Hartree-Fock method.

2.1.1 The Spherical Shell Model

The shell model was originally developed to calculate the electron states in the atomic shell. It is based on the assumptions that the electrons move (a) in orbits without colliding with each other, and (b) move in an external central potential. Both conditions are not self-evident, if the same model is applied to the nucleons of the atomic nucleus.

Nucleons are densely packed inside the nucleus. The matter radius of the nucleus is approximately $R = r_0 A^{1/3}$, where A is the atomic number and r_0 a constant with $r_0 = 1.3$ fm. A fermium nucleus with mass number 250 has thus a radius of 8 fm, only one order of magnitude larger than the charge radius of the proton, which is (0.877 ± 0.007) fm [39]. In
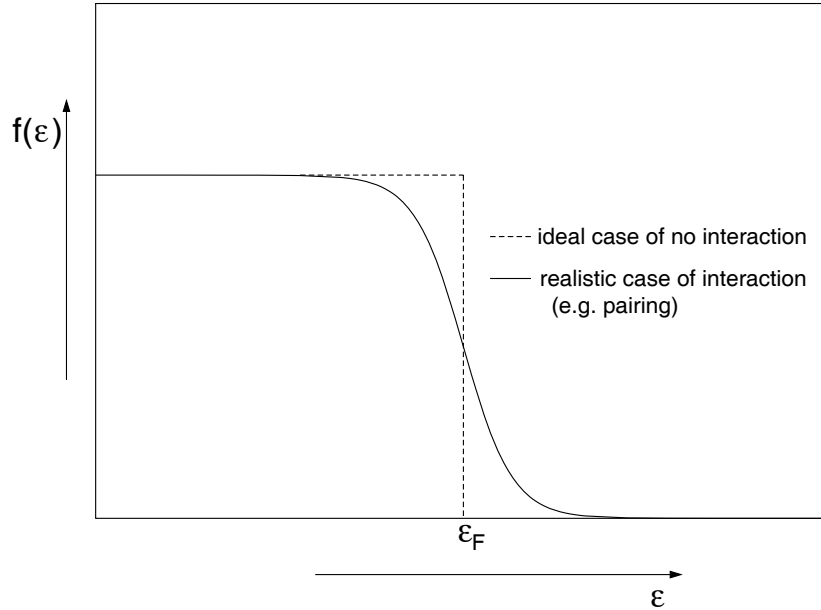
Figure 2.1: Fermi distribution of single-particle occupation probabilities $f(\epsilon)$. The single-particle energy is denoted ϵ. The Fermi energy ϵ_F is defined as the highest energy of an occupied orbit in the ideal case of no interaction.

a classical system, these particles would collide with each other. In the quantum-mechanical system, collisions are inhibited. If the nucleons are approximated as non-interacting particles moving inside a potential well, and if the system is in its ground state, the nucleons occupy the lowest states of the system. Scattering to other occupied states is forbidden by the Pauli principle, and scattering to unoccupied states would require external energy to be applied.

In Figure 2.1, the occupation probability $f(\epsilon)$ is drawn versus single-particle energy. The dashed line corresponds to the ideal case of non-interacting particles. The levels are fully occupied up to the Fermi energy ϵ_F, which is the energy of the last occupied state. Above ϵ_F, the occupation probability drops to zero. In the realistic case, pairing has to be taken into account. The pairing force is an attractive, short-range force, which couples pairs of like nucleons to spin and parity 0^+. As a consequence, the ground states of all even-even nuclei have spin and parity of $I^\pi = 0^+$. The pairing force can scatter pairs of nucleons to different orbits, and causes a smearing of occupation at the surface. The occupation probability takes the form of the Fermi distribution, which is shown as the solid curve in Figure 2.1.

In contrast to the atomic shell, the nucleus does not have an external central potential. The nuclear force is rather a two-body force, which has a repulsive core, is otherwise attractive and short-ranged. The nuclear Hamiltonian will be of the following general form (neglecting Coulomb repulsion):

$$\mathscr{H} = \sum_{i=1}^{A} T_i + \sum_{\substack{i,j=1 \\ i<j}}^{A} V_{ij}(|r_i - r_j|). \tag{2.1}$$

An exact solution for this many-body Hamiltonian can only be found for the lightest nuclei. In order for the shell model to work, a central potential has to be found which is an average
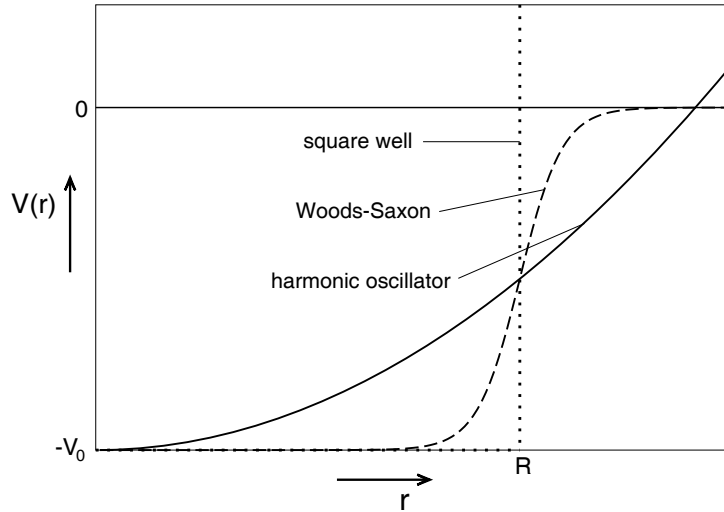
Figure 2.2: Examples of mean field potentials used in spherical-shell model calculations.

potential combining the effects of all nucleon-nucleon interactions, the so-called mean-field potential:

$$\mathscr{H} = \Big[\sum_{i=1}^{A}(T_i + U_i) \Big] + \Big[\sum_{i<j}^{A} V_{ij} - \sum_{i=1}^{A} U_i \Big] = \mathscr{H}_0 + \mathscr{H}_{res}. \tag{2.2}$$

This approach is suitable for potential shapes for which the residual interactions are minimised and can be treated as a perturbation of the mean-field potential U_i.

The shape of the mean-field potential is based on two assumptions: the potential is flat inside the nucleus, as the forces on the nucleons are approximately isotropically distributed. At the surface, a sudden drop has to occur because of the short range of the strong force. Evidence for such a shape is given by the charge and mass distribution of the nucleus, which has been measured in scattering experiments.

Three commonly used potentials are the *square-well*, *harmonic-oscillator*, and *Woods-Saxon potentials*, which are shown schematically in Figure 2.2. The former two potentials have the advantage, that they can be solved analytically. However, a more realistic potential has to be located in between these two cases, as the potential drop at the surface is too fast for the square-well, and too slow for the harmonic oscillator potential.

The *modified harmonic-oscillator potential* is an extension which corrects for this deficiency, and preserves the possibility of analytic solutions. A term proportional to $\big(-l^2 + \langle l^2 \rangle_N\big)$ is added to the oscillator potential. The $-l^2$ term compresses states with high angular momentum, which are situated close to the surface, while the $\langle l^2 \rangle_N$ term is a normalisation factor.

Another potential situated in between these extreme cases is the *Woods-Saxon potential*. It cannot be solved analytically, but the drop of the potential is included directly as a fitting

parameter, through the surface diffuseness a:

$$U(r) = \frac{-U_0}{1 + e^{\frac{r-R}{a}}}.$$ (2.3)

Here R is the nuclear radius and U_0 the potential depth.

In order to get realistic solutions, terms for spin-orbit and Coulomb forces have to be added to these potentials.

2.1.2   The Nilsson Model

Nuclei outside closed shells are generally not spherically symmetric, but deformed (see Section 2.3.1). As a consequence, the nucleons do not move in an isotropic potential, as is assumed in the spherical shell model, and degeneracy of states with the same angular momentum j, but different projection quantum number m is broken. In order to extend the shell model to deformed nuclei, Nilsson introduced a deformed potential in the Hamiltonian. Originally, he used a variation of the modified oscillator potential, so that the Hamiltonian takes following form [41]:

$$H_{Nilsson} = \frac{-\hbar^2}{2m}\nabla^2 + \frac{m}{2}\left(\omega_x^2 x^2 + \omega_y^2 y^2 + \omega_x^2 z^2\right) - C\vec{l}\cdot\vec{s} - D\left(l^2 - \langle l^2\rangle_N\right).$$ (2.4)

Here, C and D are constants to specify the strength of the $\vec{l}\cdot\vec{s}$ and $-\left(l^2 - \langle l^2\rangle_N\right)$ terms, and ω_x, ω_y, and ω_z are the oscillator frequencies along the three main axes of the nucleus. In an anisotropic potential, they are different from one another. Nilsson confined himself to axially symmetric nuclei, and introduced new oscillator frequencies $\omega_\perp$ and ω_z, which replace ω_x, ω_y and ω_z in following way:

$$\omega_x = \omega_y = \omega_\perp = \omega_o(\epsilon)\left(1 + \frac{1}{3}\epsilon\right),$$ (2.5)

$$\omega_z = \omega_o(\epsilon)\left(1 - \frac{2}{3}\epsilon\right).$$ (2.6)

The elongation parameter ϵ gives a measure of the deformation, and ω_0 is the oscillator frequency for the spherical harmonic oscillator, which is weakly dependent on ϵ to conserve the volume of the oscillator potential. Later, the model has been extended to include higher multipole orders of deformation, and more realistic potentials have been used, such as the deformed Woods-Saxon potential [42, 43].

Using the Nilsson Hamiltonian, the energies as well as eigenfunctions can be calculated as a function of ϵ. A plot of the single-particle energies versus deformation is called a Nilsson diagram. Figures 2.3 and 2.4 show the Nilsson diagram for neutrons with $N \geq 126$ and protons with $Z \geq 82$, respectively.

In a deformed potential, j is no longer a preserved quantum number, as $[H_{Nilsson}, j^2] \neq 0$. The only remaining preserved quantum numbers are the parity π and Ω, the projection of the angular momentum onto the symmetry axis. Ω is the sum of spin and orbital angular momentum projection quantum numbers of the valence nucleons, as is seen from Figure 2.5. Nilsson states are normally labeled with the so-called asymptotic quantum numbers:

$$\Omega^\pi[Nn_z\Lambda].$$ (2.7)

N is the principal quantum number, which defines the shells in the spherical case, n_z is the number of nodes of the wave function in the z direction, and Λ the projection of the orbital angular momentum onto the symmetry axis.
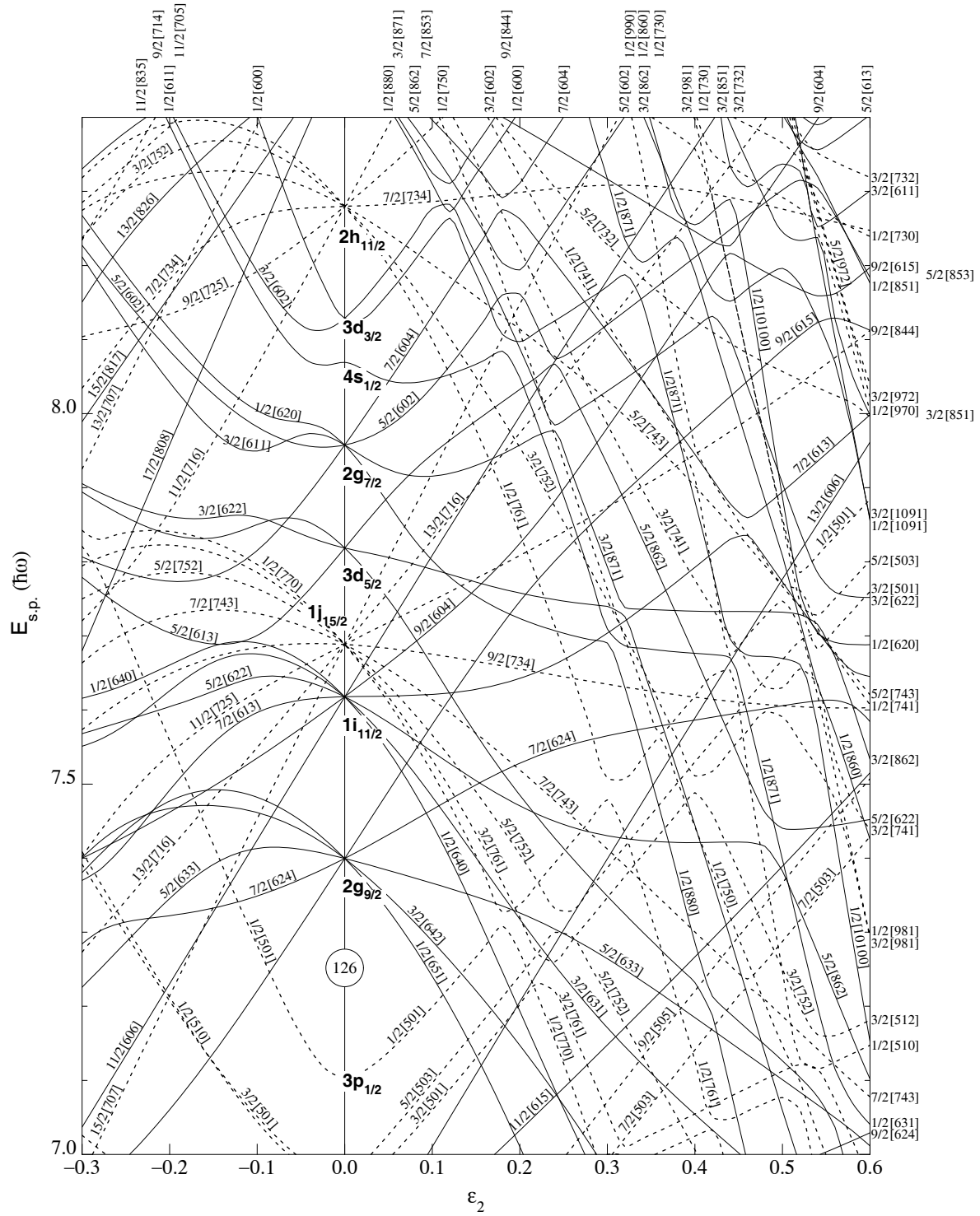
Figure 2.3: Nilsson diagram for neutrons with $N \geq 126$. The levels are calculated using the MHO potential [40]. Taken from the Table of Isotopes [12].
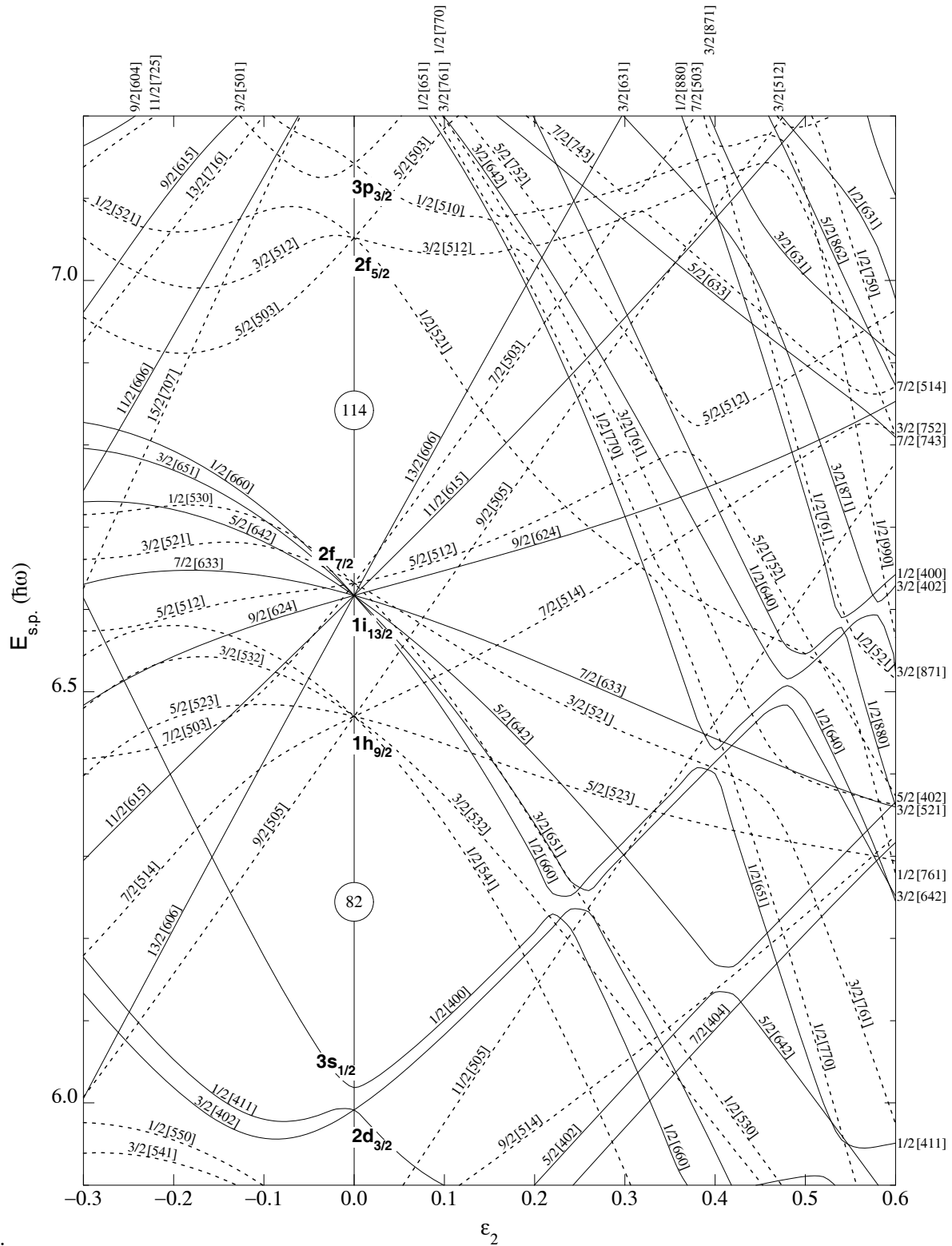
Figure 2.4: As Figure 2.3, but for protons with $Z \geq 82$.
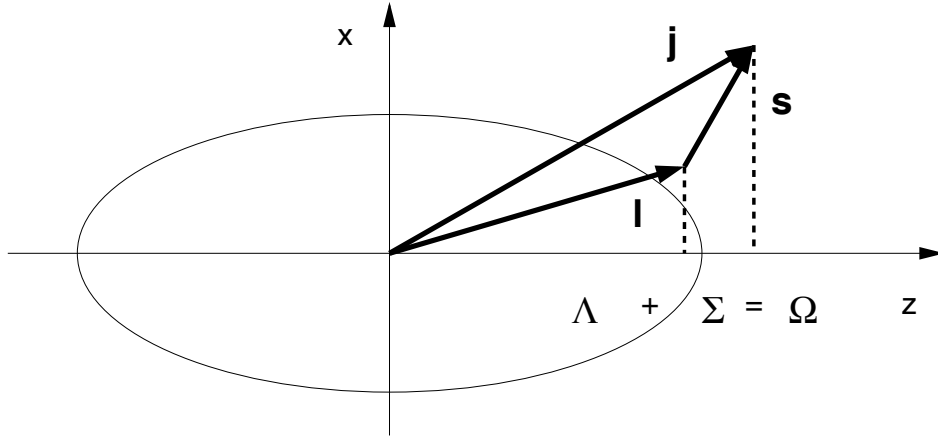
Figure 2.5: The single-particle angular momenta $\mathbf{s}, \mathbf{l}, \mathbf{j}$, and their projection on the symmetry axis Σ, Λ, Ω in an axially deformed potential.

2.1.3   Macroscopic-Microscopic Model

The shell model is a microscopic theory, which reproduces the single-particle energy spectrum as well as ground-state spins and parities. But it is not able to reproduce the total energy of a nucleus, and thereby correct binding energies, masses, and fission barriers. The liquid drop model and similar macroscopic theories on the other hand are able to predict these properties in an average way, but are not sensitive to the single-particle energies. For example, they are unable to explain the stability of transfermium elements against fission, which is due to a gain in stability from shell effects. The macroscopic-microscopic models (MMM) combine both approaches with help of the Strutinsky shell-correction method to solve these deficiencies [44].

In the MMM, an average total energy E_{LD} is defined by the liquid-drop model (or by similar models), and a shell correction energy E_{sh} for protons and neutrons is added to this bulk energy:

$$E_{tot} = E_{LD} + E_{sh}(neutrons) + E_{sh}(protons)\,. \tag{2.8}$$

The shell correction energy is derived by taking the difference between the sum over the discrete energy levels of the shell model and a smeared energy function in the same energy range. The result is the difference of the single-particle energies from an average behaviour.

The level density $g(e)$ in the discrete case reads:

$$g(e) = \sum_\nu \delta(e - e_\nu)\,, \tag{2.9}$$

where the sum goes over all energy levels ϵ_ν. It is smeared out by an exponential function over the range of the order of the shell spacing, $\gamma = \hbar\omega_0$, which results in a smeared level density $\tilde{g}(e)$:

$$\tilde{g}(e) = \frac{1}{\gamma\sqrt{\pi}} \sum_\nu f_{corr}\left(\frac{e - e_\nu}{\gamma}\right) exp\left(-\frac{(e - e_\nu)^2}{\gamma^2}\right)\,. \tag{2.10}$$

A correction function f_{corr} is included in order not to affect fluctuations over a range bigger than γ by the smearing function. The shell correction energy finally reads:

$$E_{sh} = 2\sum e_\nu - 2\int e\tilde{g}(e)de\,. \tag{2.11}$$

The shell correction is negative, if the sum of the single-particle energies in Equation 2.11 is below average, or, in other words, if there is a low level density. Negative shell corrections in turn lead to a decrease in total energy, and an increase in binding energy, the nucleus is more stable. This is the case at the position of the spherical shell closures. Note that a drop in level density can be caused by a drop in degeneracies of neighbouring levels, which has consequences for the position of the next shell closure (see Section 1).

2.1.4 Self-Consistent Mean-Field Models

The self-consistent mean-field model is based on the idea that the two-body interactions between the nucleons can be substituted by independent particles moving in an external potential, similar to the shell model. In contrast to the shell model, it does not use a phenomenological potential, but derives the potential and wave functions directly from the two-body force with help of the Hartree-Fock method.

The Hartree-Fock method is a variational method. The goal is to find an antisymmetric product wave-function, which replaces the true wave-function, which is the solution of the many-body Hamiltonian of Equation 2.1. The variational principle states that the total energy functional $E^{HF}[\{\psi_{\alpha_i}\}]$ (the total energy as function of a set of single-particle product wave functions ψ_{α_i}) is minimal for the best approximating wave function ψ_{α_k}. Here, the subscript α_k stands for one set of basis states of the single particle k. This is called the *Ritz variational principle* and leads to the following wave equation:

$$\frac{\partial E^{HF}[\{\psi_{\alpha_i}\}]}{\partial \psi_{\alpha_k}(\vec{r})} = \left[-\frac{\hbar^2}{2m}\Delta\psi_{\alpha_k} + U^H\psi_{\alpha_k} + U^F\psi_{\alpha_k} \right](\vec{r}) - \epsilon_{\alpha_k}\psi_{\alpha_k}(\vec{r}) = 0\,. \qquad (2.12)$$

The energy ϵ_{α_k} is the difference of the total energy before and after removing the particle in state α_k. It can be approximated as single-particle energy assuming the other particles are unaffected by removal of this particle. There are two potentials in the equation, the local Hartree potential U^H and the non-local Fock potential U^F, which can be expressed in the following way, when acting on a wave function ψ_{α_k}:

$$\left[U^H\psi_{\alpha_k}\right](\vec{r}) = + \int d\vec{r}' \sum_{j=1}^{N} \psi_{\alpha_j}^*(\vec{r}')v^{NN}(\vec{r};\vec{r}')\psi_{\alpha_j}(\vec{r}')\psi_{\alpha_k}(\vec{r})\,, \qquad (2.13)$$

$$\left[U^F\psi_{\alpha_k}\right](\vec{r}) = - \int d\vec{r}' \sum_{j=1}^{N} \psi_{\alpha_j}^*(\vec{r}')v^{NN}(\vec{r};\vec{r}')\psi_{\alpha_j}(\vec{r})\psi_{\alpha_k}(\vec{r}')\,. \qquad (2.14)$$

Here, $v^{NN}(\vec{r};\vec{r}')$ is the two-body interaction between particles at $\vec{r}$ and $\vec{r}'$.

Non-locality is a consequence of the fact that two particles are non-distinguishable under exchange. It has the consequence that ψ_{α_k} has to be integrated over in the Fock potential, which complicates the solution of the equations.

In order to solve these equations an iterative procedure is used, as the potentials are themselves dependent on the single-particle states. At the convergence of this procedure the Hartree-Fock single-particle basis is found. As input parameters, the equations require effective two-body interactions. Different interactions are chosen to fit properties in different regions of the nuclear chart, but are in principle used globally for all nuclei. Most commonly used effective interactions are the Skyrme interaction, which has zero-range, and the finite

σL	$T_W(\sigma L)(s^{-1})$	σL	$T_W(\sigma L)(s^{-1})$
$E1$	$1.023 \cdot 10^{14} E^3 A^{2/3}$	$M1$	$3.184 \cdot 10^{13} E^3$
$E2$	$7.265 \cdot 10^7 E^5 A^{4/3}$	$M2$	$2.262 \cdot 10^7 E^5 A^{2/3}$
$E3$	$3.385 \cdot 10^1 E^7 A^2$	$M3$	$1.054 \cdot 10^1 E^7 A^{4/3}$
$E4$	$1.065 \cdot 10^{-5} E^9 A^{8/3}$	$M4$	$3.316 \cdot 10^{-6} E^9 A^2$

Table 2.1: Weisskopf estimates $T_W(\sigma L)$ for the single-particle transition probabilities of transitions up to multipole order $L = 4$. The energies are to be given in MeV.

range Gogny force. The Hartree-Fock Bogoliubov method is a generalisation of the Hartree-Fock method and includes the pairing interaction. The relativistic mean field theory is based on the same concept, but using relativistic Dirac particles instead.

2.2   Electromagnetic Decay

A nucleus in an excited state can emit part or all of its excitation energy by electromagnetic radiation. Electromagnetic transitions are classified in terms of multipole orders of electric and magnetic fields. For each multipole transition, single-particle transition probabilities can be calculated, and are approximated by the Weisskopf estimates. The leading multipole order of a transition can be deduced from spin and parity differences with the help of selection rules. An alternative process to emission of γ radiation is the emission of electrons after internal conversion.

2.2.1   Transition Probability and Weisskopf Estimates

Classically, electromagnetic radiation is emitted by fluctuating electric and magnetic fields. These fields can be expanded in multipoles σL of either electric ($\sigma = E$) or magnetic ($\sigma = M$) type. L stands for the multipole order: 0 for monopole, 1 for dipole, 2 for quadrupole, and so on. In the quantum mechanical case, the multipole moments are replaced by multipole operators $\mathcal{M}(\sigma L)$, which allow a transition from the initial to the final state of the nucleus $M_{fi}(\sigma L) = \langle \psi_f | \mathcal{M}(\sigma L) | \psi_i \rangle$. The total transition probability $T_{fi}^{(\sigma L)}$ can then be calculated with the help of the golden rule for time-dependent perturbation theory as:

$$T_{fi}^{(\sigma L)} = \frac{2}{\epsilon_0 \hbar} \frac{L+1}{L\left[(2L+1)!!\right]^2} \left(\frac{E_\gamma}{\hbar c}\right)^{2L+1} B(\sigma L; I_i \to I_f), \qquad (2.15)$$

where ϵ_0 is the electric constant. $B(\sigma L; I_i \to I_f)$ is the reduced transition probability:

$$B(\sigma L; I_i \to I_f) = \frac{1}{2I_i + 1} |(I_f \| \mathcal{M}(\sigma L) \| I_i)|^2, \qquad (2.16)$$

where $|(I_f \| \mathcal{M}(\sigma L) \| I_i)|$ is the reduced matrix element. The reduced transition probability can be approximated to give simple single-particle transition probabilities, the so-called *Weisskopf estimates*. These are used to compare to experimental transition rates. Indication of a collective contribution to a transition can be seen from rates, which are much stronger than their Weisskopf estimate.

Weisskopf estimates are plotted for mass number $A = 250$ in Figure 2.6, and their values are given in Table 2.1. If transitions are allowed by the selection rules, they follow the general
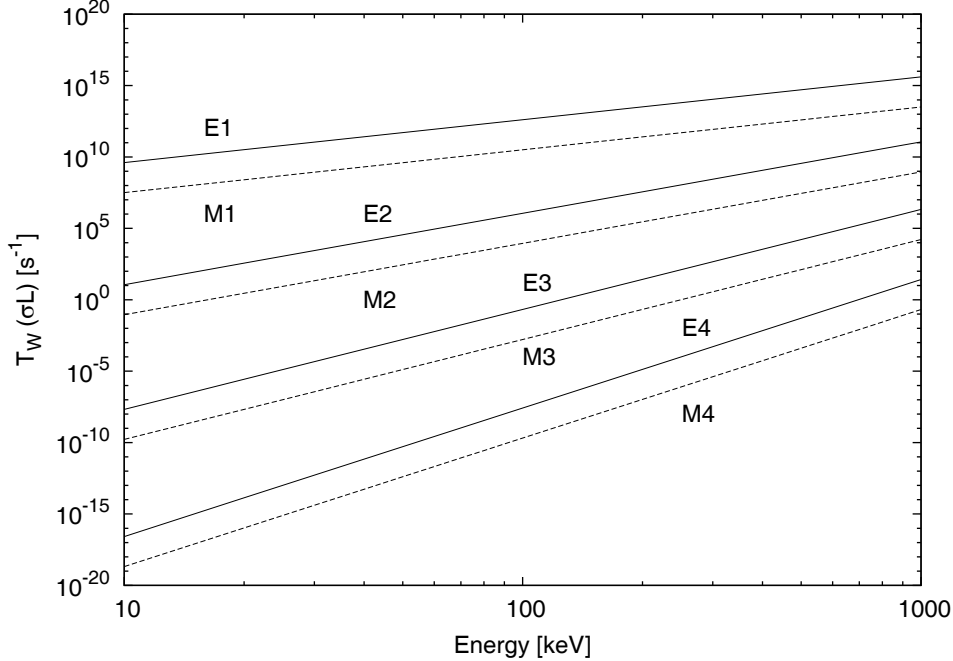
Figure 2.6: Weisskopf estimates $T_W(\sigma L)$ for the single-particle transition probabilities of transitions up to multipole order $L = 4$ for mass $A = 250$. Note that the estimates are not corrected for internal conversion.

trend, that each increase in multipole order decreases the transition probability by four to five magnitudes. For the same multipole order, transition probabilities of electric transitions are approximately two orders of magnitude stronger than those of magnetic transitions.

2.2.2 Selection Rules

During the emission of electromagnetic radiation, the angular momentum and the parity are conserved, leading to the so-called *selection rules*. If I_i and I_f are the angular momenta of the nuclear states, L is restricted in the following way:

$$|I_f - I_i| \leq L \leq |I_f + I_i| \ . \tag{2.17}$$

From the Weisskopf estimates, it is obvious that transitions with lower multipole order L are strongly favoured over higher ones. For the same multipole order, the probability for electric transitions is higher than for magnetic transitions. There are two parity selection rules, one for electric and one for magnetic transitions:

$$\pi_f^{(EL)} = (-1)^L \pi_i^{(EL)} \ , \tag{2.18}$$

$$\pi_f^{(ML)} = (-1)^{L+1} \pi_i^{(ML)} \ , \tag{2.19}$$

where π_i and π_f denote the initial and final parities.

If the spin is known, it is possible to predict the kind of radiation which is emitted with highest probability. $E2$ and $M2$ radiation dominate for example for a spin difference of

spin change	ΔI	0 (no $0 \rightarrow 0$)	1	2	3	4
parity change	yes	$E1/(M2)$	$E1/(M2)$	$M2/E3$	$E3/(M4)$	$M4/E5$
	no	$M1$	$M1/E2$	$E2/(M3)$	$M3/E4$	$E4/(M5)$

Table 2.2: Dominant γ-decay transition multipolarities depending on spin and parity change.

$|\Delta I| = 2$. But only $E2$ is possible, if the parity remains unchanged, and $M2$ will occur, if the parity changes. A list of dominant radiation types depending on spin and parity change is given in Table 2.2.

2.2.3   Internal Conversion

Instead of emission of γ radiation, the energy of an electromagnetic transition can be transferred directly to an electron of the atom. The electrons originate from the K-, L-,... shell, and they are labelled accordingly K-, L-,... electrons. The probability for internal conversion to occur has to be added to the probability of emission of a γ ray to get the total transition probability:

$$\lambda = \lambda_\gamma + \lambda_e \,. \tag{2.20}$$

The conversion coefficient α is the ratio of the internal conversion decay probability to the γ-decay probability.

$$\alpha = \frac{\lambda_e}{\lambda_\gamma} \,. \tag{2.21}$$

The total decay probability of a transition is then:

$$\lambda = \lambda_\gamma \cdot (1 + \alpha) \,. \tag{2.22}$$

The conversion coefficient increases as Z^3 and internal conversion is therefore an important process in heavy elements. Furthermore, it increases with decreasing transition energy and increasing multipolarity of the transition, and is stronger for magnetic than for electric multipole transitions. Conversion coefficients are tabulated and can be calculated [45, 46].

2.3   Rotational Motion of Nuclei

Nuclear rotation is a form of collective excitation, which is detectable for deformed nuclei. Rotated states of spherically symmetric nuclei only differ by a phase factor and are therefore undistinguishable. The nuclei in the region of ^{250}Fm are quadrupole deformed, which can be quantified by the ratio of the energies of the first 2^+ and 4^+ energies. These nuclei show very regular rotational bands, which have an energy spacing dependent on the moment of inertia.

2.3.1   Deformation

Residual interactions get stronger with a growing number of valence nucleons outside closed shells. If scalar and spin-independent, the two-nucleon force can be expanded into a series of multipole orders, generating collective quadrupole, octupole, hexadecapole, etc. deformation. Of these, quadrupole deformation is most common due to the strong quadrupole term in the expansion.

The shape can be expressed by the radius vector R, which points towards the nuclear surface. When expanded into spherical harmonics $Y_{\lambda\mu}^*(\theta, \phi)$, it reads:

$$R(\theta, \phi) = R_0 \left(1 + \sum_{\lambda\mu} \alpha_{\lambda\mu} Y_{\lambda\mu}^*(\theta, \phi) \right) . \tag{2.23}$$

Here θ and ϕ are the polar angles, R_0 is the radius vector of a sphere of the same volume, and λ denotes the multipolarity. As the monopole term corresponds to a sphere, and the dipole $\lambda = 1$ term corresponds to displacement of the sphere, the lowest order of deformation is $\lambda = 2$ or quadrupole deformation. Following orders are octupole ($\lambda = 3$) and hexadecapole ($\lambda = 4$) shapes.

A purely quadrupole deformed nucleus depends on the five variables $\mu = -2, ..., 2$. Three variables determine the position of the nucleus in the laboratory system. The two intrinsic variables can be expressed in terms of the parameters β and γ, which are defined by $a_{20} = \beta \cos \gamma$ and $a_{22} = a_{2-2} = \frac{1}{\sqrt{2}} \beta \sin \gamma$ in the body-fixed frame. β is a measure of the extent of the deformation, while γ gives the strength of axial asymmetry. If the nuclei are furthermore axially symmetric, the sum of Equation 2.23 simplifies to one term with $\alpha_{20} = \beta$. β is related to ϵ via the expression $\epsilon \approx \frac{3}{2} \left(\frac{5}{4\pi} \right)^{1/2} \cdot \beta \approx 0.95 \cdot \beta$ for small deformations.

2.3.2 Rotation

The nuclear γ-ray spectrum of quadrupole-deformed nuclei contains transitions from single-particle excitations, vibrational and rotational excitations. Pure single-particle excitations are observed in spherically-symmetric or doubly-magic nuclei. Vibration is dominant over rotation for nuclei with few valence nuclei outside the spherical core. Pure rotational spectra are only observed for nuclei with a large number of valence nucleons, which can correlate to form stable deformation. The general case is a mixture of all three, but as a first approximation they can be separated, and treated independently.

The ratio of the energies of the 4^+ and 2^+ states E_{4+}/E_{2+} is an indicator of the type of collective phenomenon. It is close to zero for closed-shell nuclei, as the pairing force drives the first excited states close to each other, and approximately 2 for purely vibrational nuclei, as the 2_1^+ state corresponds to a one- and the 4_1^+ to a two-phonon excitation. For purely rotational excitations, the ratio is 3.33, because the rotational energy is proportional to the square of the angular momentum $\hat{I}^2$. In the case of a mixture of rotation and vibration, E_{4+}/E_{2+} can take any value in between the two extremes. In Figure 2.7 the ratio is plotted for even-even isotopes between lead and nobelium. The three regions with closed-shell nuclei ($Z = 82$ and $N = 126$), vibrational nuclei near the closed shells and rotational nuclei with a large number of valence nuclei are clearly separated from each other in terms of E_{4+}/E_{2+}. The fermium isotopes are purely rotational, with a ratio of close to 3.33 for all nuclei in the same region. The assumption of separability is therefore well justified for them.

The *particle-rotor model* deals with the coupling of rotational and intrinsic excitations. If the rotation is fast, the motion of the single particle aligns with the rotational axis, classically described by the Coriolis force, and called *rotational alignment*. If on the other hand the rotation is slow, the motion of the particle in the deformed field is approximately independent of the rotation, and both can be treated independently. This is the so-called *deformation-aligned* case.
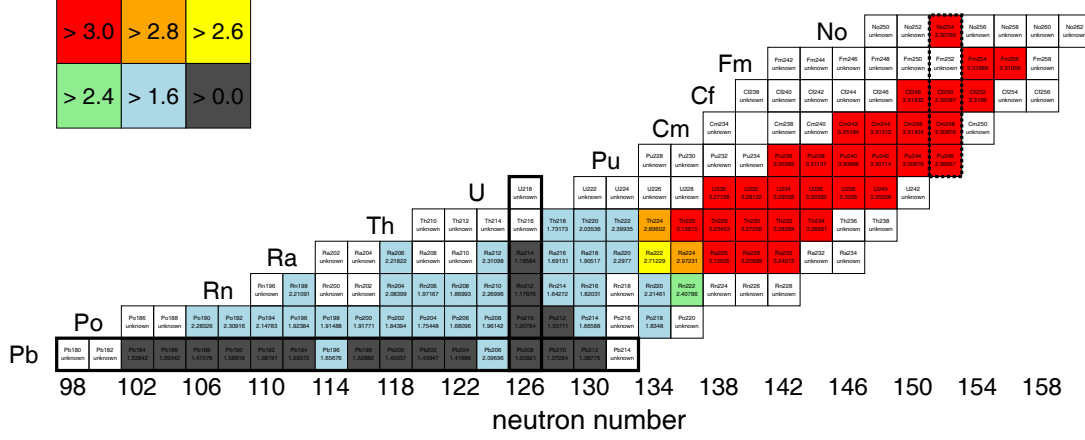
Figure 2.7: Energy ratio of the first 2^+ and 4^+ states E_{4+}/E_{2+} in even-even nuclides between lead and nobelium. The data is taken from the ENSDF database [47]. If no data is avaliable, the boxes are left white.

The coupling of the angular momenta is shown in Figure 2.8 for the deformation-aligned case. The quantum numbers of rotational nuclei can be defined relative to the laboratory and body-fixed coordinate system, labeled in the figure by letters and numbers, respectively. Angular momenta are labeled by $\mathbf{I}$ for the total angular momentum, $\mathbf{R}$ for the rotational angular momentum and $\mathbf{J} = \sum_{n=1}^{A} j_n$ for the sum of the intrinsic angular momenta of the valence nucleons outside the deformed core. $\mathbf{R}$ and $\mathbf{J}$ sum up to $\mathbf{I}$:

$$\mathbf{I} = \mathbf{J} + \mathbf{R}\,. \tag{2.24}$$

The projection of the angular momentum of one valence nucleon to the symmetry axis is called Ω_n, so the projection of $\mathbf{J}$ is $\Omega = \sum_{n=1}^{A} \Omega_n$. Rotations around the symmetry axis are indistinguishable, because the rotated wave function differs from the original one only by a phase factor. Therefore, $\mathbf{R}$ is perpendicular to the symmetry axis, and Ω coincides with K, the projection of the total angular momentum $\mathbf{I}$:

$$K = \Omega = \sum_{n=1}^{A} \Omega_n\,. \tag{2.25}$$

The total Hamiltonian can be separated into an intrinsic single-particle and a collective rotational part $H_{int} + H_{rot}$. The expression for rotational motion is found in analogy to the classical rotational energy, $E_{rot} = I^2/2\mathscr{I}$, where I is the angular momentum and $\mathscr{I}$ the moment of inertia:

$$H_{rot} \;=\; \frac{\mathbf{R}^2}{2\mathscr{I}} = \frac{1}{2\mathscr{I}}[\mathbf{I}^2 - I_3^2 + (J_1^2 + J_2^2) - (I_+J_- + I_-J_+)]\,. \tag{2.26}$$

In the second step, $\mathbf{R}^2$ is expressed in terms of the components of the total and orbital angular momentum, I_i and J_i, respectively. The raising and lowering operators $I_\pm$ and $J_\pm$ are defined as $I_\pm = I_1 \pm iI_2$ and $J_\pm = J_1 \pm iJ_2$.
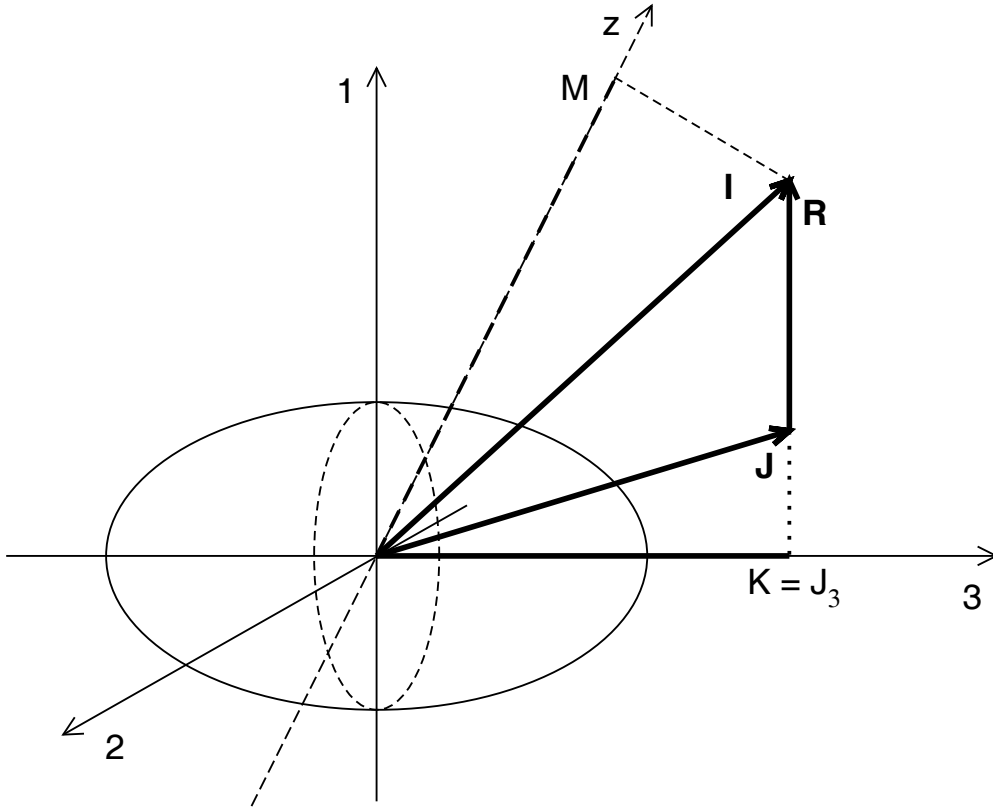
Figure 2.8: Coupling scheme of the nuclear angular momenta in the deformation-aligned case. The body-fixed coordinate system is labeled with numbers 1,2,3, where 3 coincides with the symmetry axis of the nucleus. The 3-axis of the laboratory system is labeled z. The total angular momentum is denoted **I**, the rotational angular momentum **R**, and the intrinsic angular momentum **J**. K is defined as the projection of the total angular momentum onto the symmetry axis.

In Equation 2.26, a general description would require different moments of inertia $\mathscr{I}$ for the different main axes of the nucleus. However, no rotation is possible around the symmetry axis, and in a quadrupole deformed nucleus, the remaining two main axes have identical moments of inertia, therefore $\mathscr{I}_1 = \mathscr{I}_2 = \mathscr{I}$.

Equation 2.26 can be simplified in the case of deformation alignment. The second term $J_1^2 + J_2^2$ depends only on single-particle wave functions and can be included into the intrinsic wave function, and the third term $I_+ J_- + I_- J_+$ corresponds classically to Coriolis mixing. The Coriolis force couples single-particle motion and collective rotation, and can be neglected for a slowly-rotating nucleus with large deformation and $K \neq 1/2$. The projection onto the symmetry axis I_3 can be replaced by the K quantum number, so that the rotational energy is calculated as follows:

$$E_{IK} = |e_\nu - \lambda| + \frac{\hbar^2}{2\mathscr{I}}[I(I+1) - K^2 + \delta_{K\frac{1}{2}} a(-1)^{I+\frac{1}{2}}(I + \frac{1}{2})]. \qquad (2.27)$$

Here e_ν are the single-particle energies, λ is the Fermi energy, and a the decoupling parameter discussed below. Spin eigenvalues are $I = K, K+1, K+2, \ldots$, as $K \leq I$ (see Figure 2.8).

Rotational band states can be ordered into two families according to their signature. The signature is related to the operator for rotation around the 1 axis, which is defined as $R_1 = e^{-i\pi I_1}$. Here, the 1 axis is an axis perpendicular to the symmetry axis (see Figure 2.8). The signature α is defined through the eigenvalues r of the operator by the equation $r = e^{-i\pi\alpha}$, and takes the values:

$$
\begin{array}{lll}
\text{even mass} & \alpha = 0 & \text{spin sequence } 0,2,4,6.. \\
& \alpha = 1 & \text{spin sequence } 1,3,5.. \\
\text{odd mass} & \alpha = \frac{1}{2} & \text{spin sequence } \frac{1}{2},\frac{5}{2},\frac{9}{2}.. \\
& \alpha = -\frac{1}{2} & \text{spin sequence } \frac{3}{2},\frac{7}{2},\frac{11}{2}..
\end{array}
$$

Each band has thus two signature partners.

Bands with $K = 0$ and $K = 1/2$ are exceptional with respect to the signature partners. Bands with $K = 0$ only show the even branch of the rotational band, a sequence with spins of $I = 0, 2, 4, \ldots$. The states with odd spin vanish because of the reflection symmetry of the system. For $K = 1/2$ bands and for fast rotation, signature splitting occurs. In the case of $K = 1/2$ bands, the signature splitting is defined by the decoupling parameter a, as is indicated in the last term of Equation 2.27.

Fast nuclear rotation is treated in the cranked-shell model. Rotation is introduced in the form of a rotating potential. The cranked Hamiltonian H^ω is derived from the time-dependent Hamiltonian in the laboratory frame H by transformation of the wave functions to rotating coordinates. The rotation operator is $R_1 = e^{-iI_1\omega t}$, where ω denotes the rotational frequency, and I_1 the spin projection operator onto the 1 axis. The 1 axis is defined as an axis perpendicular to the symmetry axis, by choice the rotational axis:

$$H^\omega \Phi^\omega = i\frac{\partial}{\partial t}\Phi^\omega = (H_{int} - \omega I_1)\,\Phi^\omega\,. \tag{2.28}$$

Here, $\Phi^\omega = R_1\Phi_{lab}$, where Φ^ω and Φ_{lab} are the wave functions in the rotated internal and the laboratory system, respectively. $H_{int} = R_1^{-1}HR_1$ is the static Hamiltonian in the rotating system. The solutions of the cranked Hamiltonian E^ω are called *Routhians*.

The real single-particle energies can be calculated from the Routhians in the following way (e_ν, e_ν^ω, h_{int}, j_1 are the single-particle values of E_ν, E_ν^ω, H_{int}, J_1):

$$e_\nu = \langle\nu|\,h\,|\nu\rangle = \langle\nu^\omega|\,h_{int}\,|\nu^\omega\rangle = e_\nu^\omega + \hbar\omega\,\langle\nu^\omega|\,j_1\,|\nu^\omega\rangle\,. \tag{2.29}$$

The quantum numbers of the rotated and laboratory system are represented by ν^ω and ν, respectively.

The Routhians are an important tool to calculate alignments in rotational bands. Alignment of protons and neutrons along the rotational axis is caused by the Coriolis force, which can break nucleon pairs, if the rotation is fast enough. The frequency at which the particles align, can be deduced from a Routhian plot. The alignment i_1, i.e. additional spin along the rotational axis, is directly related to the slope of the Routhians by the relation:

$$i_1 = \frac{de_\nu^\omega}{d\omega} = -\hbar\,\langle\nu^\omega|\,j_1\,|\nu^\omega\rangle\,. \tag{2.30}$$

Therefore, especially orbits with large angular-momentum components along the rotational axis are energetically favoured and most affected. Alignment can be blocked for a state if it is occupied by a single unpaired particle, as is the case in two-quasiparticle excitation, and for the unpaired nucleon in odd-mass nuclei.

2.3.3   Moment of Inertia

The relation between energy E_{IK} and spin $I(I+1)$ in Equation 2.27 is not purely quadratic, but shows a steeper increase even in the absence of mixing. The moment of inertia lies between two extreme cases. One extreme corresponds to surface-waves, where one assumes a fluid of valence nucleons on top of an inert core. The other extreme is the rigid body, analoguous to the classical case. The measured moment of inertia is closer to the former for small rotation, and moves towards the rigid-body value as rotation increases.

An explanation of this effect was given by Bohr, Mottelson, and Pines [48], who applied pairing to the nucleus. At rest and slow rotation, all nucleons are paired, such that they move like a superfluid. As the rotation increases, the Coriolis force breaks pairs, which causes the moment of inertia to increase, until it reaches the rigid body value at very fast rotation. The effect of pairing on the moment of inertia in terms of the BCS theory was studied by Belyaev, who found following formula for $\mathscr{I}$ [49]:

$$\mathscr{I} = 2\hbar^2 \sum_{\nu_1 \nu_2} \frac{|<\nu_2|I_x|\nu_1>|^2}{E(\nu_1) + E(\nu_2)} \left(U(\nu_1)V(\nu_2) - V(\nu_1)U(\nu_2)\right)^2 \tag{2.31}$$

The sum in this equation goes over all possible two-quasiparticle excitations $\nu_{1,2}$. I_x denotes the projection of the spin onto the rotational axis, and U and V are the emptiness and fullness factors, such that U^2 and V^2 give the unoccupancy and occupancy probability, respectively. The pairing correlations reduce the moment of inertia in two ways: by decreasing the factor with U and V, which is 1 when neglecting pairing, and smaller otherwise. And by increasing the quasiparticle energies, which is $\geq 2\Delta$.

An alternative approach was found by Davydov and Chaban [50,51], who assume coupling of β-vibrations and rotational motion, leading to centrifugal stretching and thus an increase in $\mathscr{I}$.

The variation in moment of inertia can be included into the rotational energy equation 2.27 by allowing higher-order terms of spin $I(I+1)$. Alternatively, an expression for the rotational energy in terms of an expansion series of angular velocity ω was found by Harris [52].

$$E_{rot} = \frac{1}{2}\omega^2 \left(\mathscr{I}_0 + 3C\omega^2 + 5D\omega^4 + \cdots\right) . \tag{2.32}$$

The expression is based on the cranking model, but uses higher-order correction terms. A similar expression is found for the moment of inertia, and combining both equations they can be used to fit the energies of rotational states depending on spin I. The variable moment of inertia (VMI) model is equivalent to Harris' expression [53], but the starting point is a phenomenological expression for the rotational energy. It depends on the moment of inertia as a free variable which has to be fitted for each spin value I.

To visualise the variation of the moment of inertia with spin, the kinematic moment of

inertia $\mathscr{I}^{(1)}$ and the dynamic moment of inertia $\mathscr{I}^{(2)}$ are introduced as follows [1]:

$$\mathscr{I}^{(1)} = \hat{I}\left(\frac{dE(\hat{I})}{d\hat{I}}\right)^{-1} = \frac{\hat{I}}{\omega(\hat{I})} \, . \tag{2.34}$$

$$\mathscr{I}^{(2)} = \left(\frac{d^2 E(\hat{I})}{d\hat{I}^2}\right)^{-1} = \frac{d\hat{I}}{d\omega} \, . \tag{2.35}$$

Experimental measurement values in a typical rotational band with spin difference $\Delta I = 2$ are transition energy E_γ and spin I. The moments of inertia $\mathscr{I}^{(1)}$ and $\mathscr{I}^{(2)}$ depend on these values in following way:

$$\mathscr{I}^{(1)} = \hat{I}\left(\frac{dE}{d\hat{I}}\right) \approx \frac{\hat{I}\Delta\hat{I}}{\Delta E} = \frac{\Delta(\hat{I})^2}{2\Delta E} = \frac{\hbar^2(2I-1)}{E_\gamma(I \to I - 2)} \, , \tag{2.36}$$

$$\mathscr{I}^{(2)} = \left(\frac{d^2 E}{d\hat{I}^2}\right)^{-1} = \frac{dI}{d\omega} \approx \frac{\Delta I}{\Delta E_\gamma/2\hbar} = \frac{4\hbar^2}{\Delta E_\gamma} \, . \tag{2.37}$$

Values for the dynamic and the kinematic moment of inertia are given in units of $\hbar^2/MeV$.

Usually, the moments of inertia are plotted versus the rotational frequency. The rotational frequency is the derivate of rotational energy with respect to spin:

$$\omega(I) = \frac{1}{\hbar}\frac{dE(I)}{dI} \approx \frac{\Delta(E)}{\Delta(I)} = \frac{E_\gamma}{2\hbar} \, . \tag{2.38}$$

As $\mathscr{I}^{(2)}$ is defined for a state, i.e. in between the γ transitions, the average of the transition energies has to be taken to derive the rotational frequency corresponding to $\mathscr{I}^{(2)}$:

$$\omega(I - 1) = \frac{1}{2\hbar}\frac{E_{\gamma 1} + E_{\gamma 2}}{2} \, . \tag{2.39}$$

2.4 Nuclear Electromagnetic Moments

As most nuclei are deformed, and as nucleons are moving inside the nucleus, charge and current distributions result. These can be expanded into series of electric and magnetic moments. For this study, the electric quadrupole and magnetic dipole moments are of particular interest and will be discussed in the following.

2.4.1 Electric Quadrupole Moment

If a nucleus is deformed, its charge distribution $\rho(\vec{r})$ will also be non-spherical. Is is assumed that this charge distribution $\rho(\vec{r})$ is a smooth function of the points $\vec{r}$ within the volume, which is justified for nuclei with a sufficiently large number of nucleons. The general expression for a potential $\Phi(\vec{R})$ of a point at position $\vec{R}$ caused by $\rho(\vec{r})$ is given by following expression:

$$\Phi(\vec{R}) = \frac{1}{4\pi\epsilon_0}\int\frac{\rho(\vec{r})}{|\vec{R}-\vec{r}|}d\vec{r} \tag{2.40}$$

---

[1]The correct form of the equations requires the aligned angular momentum I_x, since rotation is defined on this axis. For $I \gg K$ one can approximate I_x:

$$\hat{I}_x = \hbar\sqrt{I(I+1) - K^2} \approx \hbar\sqrt{I(I+1)} = \hat{I} \, . \tag{2.33}$$

This formula can now be studied in terms of multipole moments, if the distance of the measurement point $|\vec{R}|$ is large compared to the points within the distribution, $|\vec{r}|$. Expanding in a series for $|\vec{r}|/|\vec{R}|$ gives:

$$
\begin{aligned}
\Phi(\vec{R}) &= \frac{1}{4\pi\epsilon_0}\left(\frac{q}{R} + \int \frac{\rho(\vec{r})r\cos\theta}{R^2}d\vec{r} + \frac{1}{2}\int \frac{\rho(\vec{r})(3\cos\theta - 1)r^2}{R^3}d\vec{r} + \cdots\right) \\
&= \frac{1}{4\pi\epsilon_0}\left(\frac{q}{R} + \sum_i \frac{p_i x_i}{R^3} + \sum_{ij}\frac{1}{2}\frac{Q_{ij}x_i x_j}{R^5} + \cdots\right).
\end{aligned}
\tag{2.41}
$$

Here, x_i (with $i \in 1,2,3$) stand for the Cartesian coordinates, and θ is the angle between $\vec{R}$ and $\vec{r}$. The monopole term $q = \int \rho(\vec{r})d\vec{r}$ corresponds to the whole charge of the system. Dipole and quadrupole terms are given by p_i and Q_{ij}, respectively. The quadrupole term is a 3x3 tensor, which can be simplified by transformation into the body-fixed frame, such that the non-diagonal terms vanish. The *intrinsic quadrupole moment* is defined along the symmetry-axis, and takes following form, if the symmetry axis is chosen to be the z axis:

$$
Q_0 \equiv Q_{\bar{z}\bar{z}} = \int \rho(\vec{r})(3z^2 - r^2)d\vec{r}.
\tag{2.42}
$$

The quadrupole moment vanishes for spherical distributions, is negative for oblate, and positive for prolate distributions.

By solving Equation 2.42 for a rotational ellipsoid and expressing the result in terms of the deformation parameter β, the intrinsic quadrupole moment takes following form:

$$
Q_0 = \frac{3}{\sqrt{5\pi}}ZR_0^2\beta(1 + 0.16\beta + \dots).
\tag{2.43}
$$

The radius R_0 is defined as the radius of a sphere of same volume as the deformed nucleus (see as well Equation 2.23), and Z is the atomic number of the nucleus. Equation 2.43 is an approximation for quadrupole deformed nuclei with sufficiently small β. The reduced transition probabilities of the electrical quadrupole $E2$ transitions within a rotational band depend on Q_0 and take following relatively simple form, as the internal structure does not change:

$$
B(E2; KI_1 \rightarrow KI_2) = \frac{5}{16\pi}e^2 Q_0^2 < I_1 K 20|I_2 K >^2,
\tag{2.44}
$$

where I_1 is the spin of the initial, and I_2 the one of the final state. From Equation 2.15, the transition probability can be calculated as:

$$
T(E2; KI_1 \rightarrow KI_2)[s^{-1}] = 1.225 \cdot 10^9\,(E_\gamma[MeV])^5\,B(E2)[e^2 fm^4],
\tag{2.45}
$$

where the values for the transition energy E_γ and reduced transition probability $B(E2)$ are to be given in units indicated in the brackets.

In rotational ground-state bands, Equations 2.43 and 2.50 can be used in conjunction with phenomenological relations between the 2^+ energy and $B(E2)$ value to calculate the deformation of the nucleus from the ground-state band transition energies.

2.4.2 Magnetic Dipole Moment

Classically, a charged particle moving in a circular loop creates a magnetic dipole moment $\vec{\mu}$, which is proportional to the angular momentum of the particle $\vec{l}$. In the corresponding quantum mechanical description, the g factor is introduced as proportionality constant between the angular momentum and magnetic dipole moment μ, which is:

$$\frac{\mu}{\mu_N} = \frac{<l, m_l = l|\mu_z|l, m_l = l>}{\mu_N} = g_l m_{l,max} \, . \tag{2.46}$$

The dipole moment μ is given in units of the nuclear magneton $\mu_N = (e\hbar)/(2M_p)$, where M_p is the proton mass. As in the classical case, the vector $\vec{\mu}$ points in the same direction as the angular momentum vector $\vec{l}$. A magnetic moment is also created by the spin, which has no classical analogue. In contrast to the g_l factors, the internal g_s factors are non-integer, and, despite having no charge, even the neutron has a magnetic moment. This is evidence for the internal quark structure of the particles. Following values are found experimentally in the case of free particles:

$$g_l = 1 \quad g_s = 5.5858 \qquad \text{proton} \, ,$$
$$g_l = 0 \quad g_s = -3.8261 \quad \text{neutron} \, .$$

The contributions of spin and orbital angular momenta add up to the total dipole moment, $\vec{\mu} = g_l \vec{l} + g_s \vec{s}$. As a consequence, the direction of dipole moment and total spin $\vec{j} = \vec{l} + \vec{s}$ do not agree because of the different size of g_l and g_s. However, the strength is still defined by Equation 2.46, where l has to be replaced by the total angular momentum j. In the general case of coupling of two independent angular momenta j_1 and j_2 to J, the g factor of the coupled system g_J reads:

$$g_J = \frac{(g_1 + g_2)}{2} + \frac{(g_1 - g_2)}{2} \left[\frac{j_1(j_1 + 1) - j_2(j_2 + 1)}{J(J + 1)} \right] \, , \tag{2.47}$$

where g_J is defined through $\vec{\mu}_J = g_J \vec{J}$.

The so-called *Schmidt lines* are theoretical values for the magnetic dipole moment versus nuclear spin for ground state configurations of odd-A nuclei, where the valence nucleon is treated as a free particle. These calculated values deviate from the measured ones, especially for heavier nuclei. The picture of free protons and neutrons is thus too simple, as polarisation of the core nucleons has to be taken into account. Realistic effective g factors can be calculated with help of advanced theories.

In rotating nuclei, the contributions of the rotational core and valence nucleons are separated. Two g factors are introduced: the intrinsic g factor g_K and the rotational one g_R. The contribution of the rotational core to the magnetic dipole moment can be estimated for the ground-state band of an even-even nucleus with pure rotational motion:

$$\frac{\mu}{\mu_N} = g_R m_{R,max} \, , \tag{2.48}$$

where $\vec{R}$ is the angular momentum of the core. The parameter g_R equals approximately Z/A, which implies uniform rotation of a charged body. In the general case of a band with $K > 1/2$, the magnetic dipole moment reads:

$$\frac{\mu}{\mu_N} = g_R I + (g_K - g_R) \frac{K^2}{I + 1} \, . \tag{2.49}$$

Gyromagnetic factors are powerful tools to identify states by comparing theoretical predictions of Nilsson configurations to experimental results. One way is to compare the ratio of the reduced transition probability of $M1$ and $E2$ transitions within a rotational band, $B(M1)/B(E2)$, to the experimental intensity ratios. $B(E2)$ is given by Equation 2.44, and $B(M1)$ for a transition from states with spin I_1 to I_2 reads:

$$B(M1; KI_1 \rightarrow KI_2) = \frac{3}{4\pi} \left(\frac{e\hbar}{2Mc}\right)^2 (g_K - g_R)^2 K^2 < I_1 K 10 | I_2 K >^2 . \qquad (2.50)$$

From the reduced transition probability $B(M1)$, the transition probability $T(M1)$ can be calculated as follows:

$$T(M1; KI_1 \rightarrow KI_2)[s^{-1}] = 1.758 \cdot 10^{13} \, (E_\gamma[MeV])^3 \, B(M1)[\left(\frac{\mu_N}{c}\right)^2]. \qquad (2.51)$$

As in the case for $T(E2)$, transition energy E_γ and reduced transition probability $B(M1)$ are to be given in units indicated in the brackets.

It is evident from Table 2.1 that $E2$ transitions can give a small contribution to the intensity of the $M1$ transition. Thus the mixing ratio $\delta_{E2/M1}$ has to be taken into account, which is defined through the ratio of the transition probabilities:

$$\delta_{E2/M1}^2 = \frac{T(E2, I \rightarrow I-1)}{T(M1, I \rightarrow I-1)} . \qquad (2.52)$$

2.5   K-Isomerism

Isomers are defined as metastable nuclear excited states. There is no clear definition of where the limit is drawn between isomeric and non-isomeric states, except that the former have to have half lives longer than typical non-isomeric half-lives in the range of tens or hundreds of picoseconds. Thus a typical limit is given to be 1 ns. For focal-plane studies at the setup in Jyväskylä, lower limits for observable half lives are given by the flight time through the recoil separator, which is of the order of half a microsecond, and by the read-out time of the DSSSD detectors, which is of the order of 12 μs (unless the number of implanted nuclei is very high).

Nuclear isomers are classified in three groups: spin traps, shape isomers, and K-traps [54]:

Spin traps are related to the transition probabilities discussed in Section 2.2.1. If the excited state can only decay into states with large difference in spin, the fast low-multipolarity transitions are forbidden by the selection rules, and only transitions of high multipolarity, low transition probability and therefore long half life are allowed (see Table 2.2 and Figure 2.6).

A *shape isomer* can occur, if the total binding energy of the nucleus has a second minimum at large elongation. If fission is a competing decay channel, these isomers are called *fission isomers.*

Only parity and the projection of the total spin on the symmetry axis, K, are preserved quantum numbers in deformed nuclei. Allowed electromagnetic transitions have to fulfil the condition, that $\lambda \geq \Delta K$, where λ stands for the multipolarity of the transition. Thus a K *trap* occurs, if the change in K-quantum number ΔK between initial and final state is large.

It was shown in Section 2.3, that K equals the projection of the intrinsic angular momenta Ω for axially-symmetric nuclei. In a two-quasiparticle excitation, the single particles couple their spin either parallel or antiparallel, giving a total spin projection of $\Omega = |\Omega_1 \pm \Omega_2|$. Gallagher found that the two-fold degeneracy is broken by spin-dependent residual interactions,

and that the coupling is favoured in which the intrinsic spin projections of the single particles add up to zero, i.e. $\Sigma = \Sigma_1 + \Sigma_2 = 0$ [55]. In the favoured case, the two projections Ω_1 and Ω_2 couple in following way:

$$\Omega = |\Omega_1 - \Omega_2| \qquad \text{if} \quad \Omega_1 = \Lambda_1 \pm 1/2 \, , \Omega_2 = \Lambda_2 \pm 1/2 \, ; \qquad (2.53)$$

$$\Omega = \Omega_1 + \Omega_2 \qquad \text{if} \quad \Omega_1 = \Lambda_1 \pm 1/2 \, , \Omega_2 = \Lambda_2 \mp 1/2 \, . \qquad (2.54)$$

Because of K mixing, low-multipolarity transitions are possible, even though ΔK is large. In this case, one speaks of forbidden transitions. Löbner defined the degree of forbiddenness as $\nu = \Delta K - \lambda$ [56]. He found, that per unit of forbiddenness, the reduced transition probability decreases by a factor of 100. The hindrance factor is defined by:

$$F_W = \frac{T^\gamma_{1/2}(\text{experiment})}{T^\gamma_{1/2}(\text{Weisskopf})} \, , \qquad (2.55)$$

where $T^\gamma_{1/2}(\text{experiment})$ and $T^\gamma_{1/2}(\text{Weisskopf})$ are the experimental and Weisskopf half lives. The *reduced hindrance* f_ν can be defined as:

$$f_\nu = F_W^{1/\nu} \approx 100 \, , \qquad (2.56)$$

which equals approximately 100 according to the relation of forbiddenness and transition probability found by Löbner.

Chapter 3

Experimental Methods and Devices

In this chapter, the experimental devices and methods which are used to study heavy nuclei at the Accelerator Laboratory of the University of Jyväskylä (JYFL), are introduced. In the first section of this chapter, the fusion-evaporation reactions are described, by which the fermium isotopes have been produced. The experimental setup contains three parts: the γ-ray spectrometer JuroGam, the gas-filled recoil separator ritu and the focal-plane detector setup great, which are explained one after another in Section 3.2. The full capacity of this setup is realised in their combination, for which different tagging techniques are used, described in Section 3.3. By implementing Total-Data-Readout (TDR), dead time is reduced and more flexible data-handling is possible. For online- and offline-analysis, the software package grain has been developed. A short overview over the principles of TDR and grain is covered in Section 3.4. Finally, some analysis details such as energy calibration, efficiency measurement and gating are given in Section 3.5.

3.1 Fusion-Evaporation Reaction

Extensive spectroscopy of nuclei in the region of ^{254}No has been possible because of the use of fusion-evaporation reactions, which generate sufficiently high cross section and angular momentum.

Fusion-evaporation reactions can be regarded as a two-step process; the fusion of projectile and target forming the compound nucleus, and its decay by evaporation of light particles [57]:

$$A + a \rightarrow C^* \rightarrow B + b\,.$$

A classical model for fusion was introduced by Bass [58], using the liquid drop model to describe the potentials of projectile and target. Both are assumed to be spherical, and essentially unchanged in mass, as long as their distance r is larger than $R_{12} = R_1 + R_2$, where R_1 and R_2 are the half-density radii of projectile and target. As soon as they get closer, they penetrate each other, and their energy will be dissipated in collisions between the nucleons. Note that surface reactions can occur already within the interaction distance $r_{int} = R_{12} + d_{int}$, corresponding to the *Bass interaction barrier*, B_{int}. Fusion of projectile and target nuclei is possible, if the energy exceeds the *Bass fusion barrier* B_{fus}, which is the maximum value of the potential composed from nuclear, Coulomb and centrifugal parts. B_{fus} is situated between the contact and interaction distance $R_{12} \leq r_{fus} \leq r_{int}$.
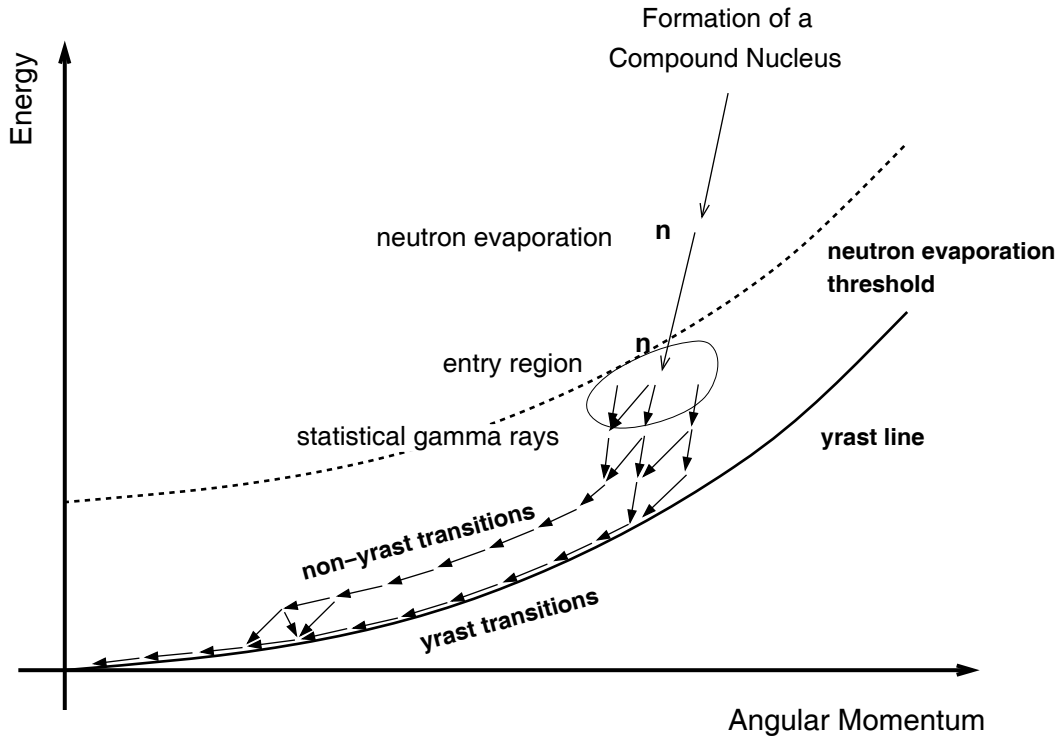
Figure 3.1: Schematic picture of the decay of the compound nucleus in the fusion-evaporation process.

During the fusion process, the reaction energy is shared among many configurations. It is very unlikely for it to be concentrated in one or a few nucleons, which could escape and deexcite the nucleus. The compound nucleus exists thus for approximately 10^{-19} s to 10^{-16} s, which is long compared to the time a projectile needs to pass the target nucleus, which is of the order of 10^{-21} s. As the compound system goes through many configurations during this time, the creation and decay channels of the compound system can be said to be independent of each other. The cross section is then a product of creation cross section and branching ratio:

$$\sigma = \sigma_{\mathrm{fusion}} G_{\mathrm{branching}} .$$

The decay of the compound nucleus occurs in a stepwise manner (schematically drawn in Figure 3.1). At first, light particles are evaporated. As neutrons do not have to overcome the Coulomb barrier, their evaporation is strongly favoured over protons and alpha particles. The excitation energy of the compound nucleus is reduced by rest mass, separation energy and kinetic energy of the evaporated particles, which carry only little angular momentum. When the energy is below the particle evaporation threshold, the decay will continue first by so-called statistical γ rays, which are mainly of $E1$ type, and finally by discrete γ rays at or close to the yrast line. The yrast line defines the minimal energy of the nucleus at a certain spin, given by the rotational energy formula in Equation 2.27.

The excitation energy of the compound nucleus is the sum of the centre-of-mass energy E_{cms} and the Q-value of the reaction:

$$E_{exc} = E_{cms} + Q \tag{3.1}$$
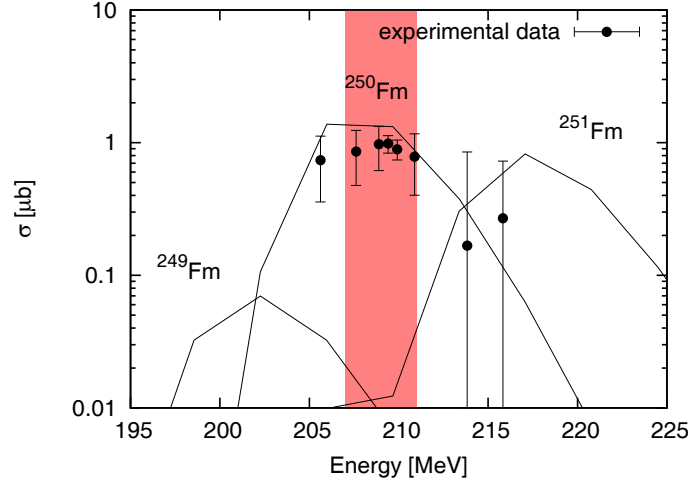
Figure 3.2: Excitation functions of ^{250}Fm, ^{249}Fm, and ^{251}Fm for the reaction ^{48}Ca + ^{204}Hg. Continuous lines correspond to calculations with the HIVAP code, the data points to experimental data measured in [13]. The bombarding energy interval in the ^{250}Fm experiment due to energy loss in the target is marked in red. The Bass interaction barrier for this reaction is $B_{int} = 212.8$ MeV, and the fusion barrier $B_{fus} = 226.1$ MeV. Graph adapted from [13].

The Q value is defined as the difference of binding energies of the nuclei before and after the reaction:

$$Q = BE_{compound} - (BE_{projectile} + BE_{target}) \tag{3.2}$$

It is strongly negative for heavy-ion fusion-evaporation reactions in the heavy-element region. If target and projectile are doubly magic, the Q value is even more negative, which lowers the excitation energy of the compound nucleus. This leads to increased survival probability of the compound nucleus against fission, and an exceptionally high fusion-evaporation cross section. In the case of ^{208}Pb$(^{48}$Ca, 2n$)^{254}$No, where both projectile and target are doubly magic, the cross section peaks at approximately 3 μb [59]. It decreases for neighbouring nuclei, to for example 1 μb in the case of ^{204}Hg$(^{48}$Ca, 2n$)^{250}$Fm (see Figure 3.2), and around 10 nb for ^{208}Pb$(^{40}$Ar, 2n$)^{246}$Fm [13, 27]. The relatively high cross sections facilitate spectroscopy in the region of the nuclear chart close to ^{254}No, which are the heaviest nuclei for which in-beam spectroscopy is possible by using the recoil-decay tagging technique.

The fermium isotopes in this study are produced via the ^{202}HgS$(^{48}$Ca, 2n$)^{248}$Fm and ^{204}HgS$(^{48}$Ca, 2n$)^{250}$Fm reactions. The peak in the excitation function for the 2n channel lies between the Bass interaction and fusion barriers. The excitation function is therefore relatively narrow, as it is cut by the barrier on the low-energy side, and by fission on the high-energy side. For the same reason, the cross sections of the 1n and 3n channels are much smaller, the reaction is thus very clean and the overlap small. For ^{250}Fm in Figure 3.2, the cross sections of the 1n and 3n channel, leading to production of ^{251}Fm and ^{249}Fm, are below 2 % of the cross section of the 2n channel at the centre-of-target energy of 209 MeV, according to the HIVAP calculations.

The target thicknesses in the experiments were of the order of $\approx$ 0.5 mg/cm^2. These targets are thin, which means that the energy loss of the beam in the target is relatively small, and the bombarding energy lies in a narrow band, in the case of ^{250}Fm within 207-
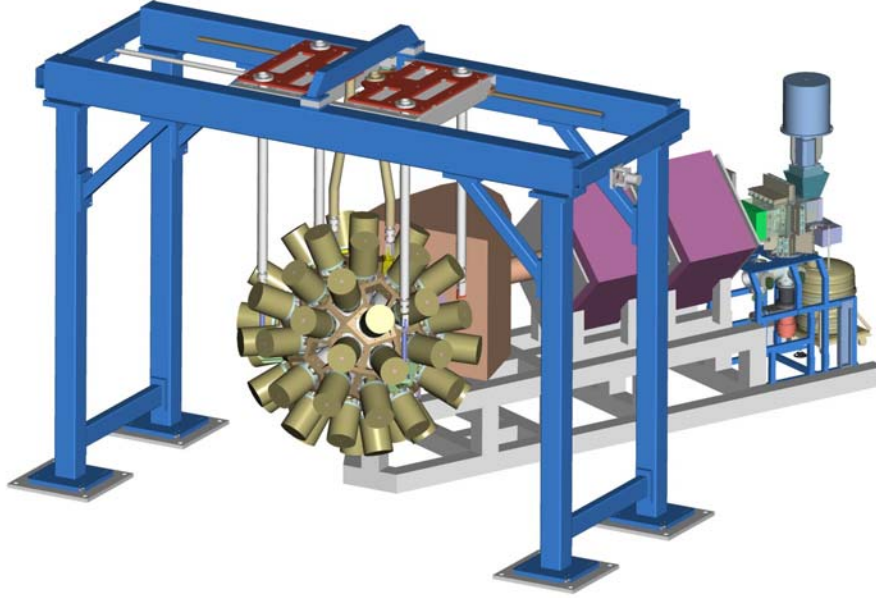
Figure 3.3: Schematic, from left to right, of JuroGam/ritu/great. Courtesy of D. Seddon.

211 MeV (see Figure 3.2). As a consequence, the reaction energy is well-defined, the competing evaporation channels have small cross section, and the Doppler broadening caused by different recoil velocities is small.

3.2   Experimental Setup

The different parts of the experimental setup at the Accelerator Laboratry of the University of Jyväskylä (JYFL) are explained in this section. It includes the germanium detector array at the target JuroGam (upgraded to JuroGamII at present), the recoil separator ritu, and the focal-plane detector setup great (see Figure 3.3).

3.2.1   JuroGam

The JuroGam array is designed to perform prompt coincidence γ-ray spectroscopy at the target position, for which good statistics, a high number of coincident γ rays, good resolution, and high Peak-to-Total ratio are needed. For this purpose, following requirements have to be fulfilled: (1) High efficiency of the array, achieved by high coverage of solid angle and high efficiency of the detectors; (2) high granularity to increase the number of coincidences; (3) good energy resolution of the detectors, and (4) good Peak-to-Total ratio, that is low background caused by Compton scattering, in order to get clean spectra.

The array was originally designed as eurogam, which consisted of 12 pentagons each carrying 6 detector modules [60]. The array had 70 detectors, where two modules were left out for incoming and outgoing beam. In contrast to eurogam, JuroGam is run in combination with a recoil-separator. As the first quadrupole lies directly behind the target
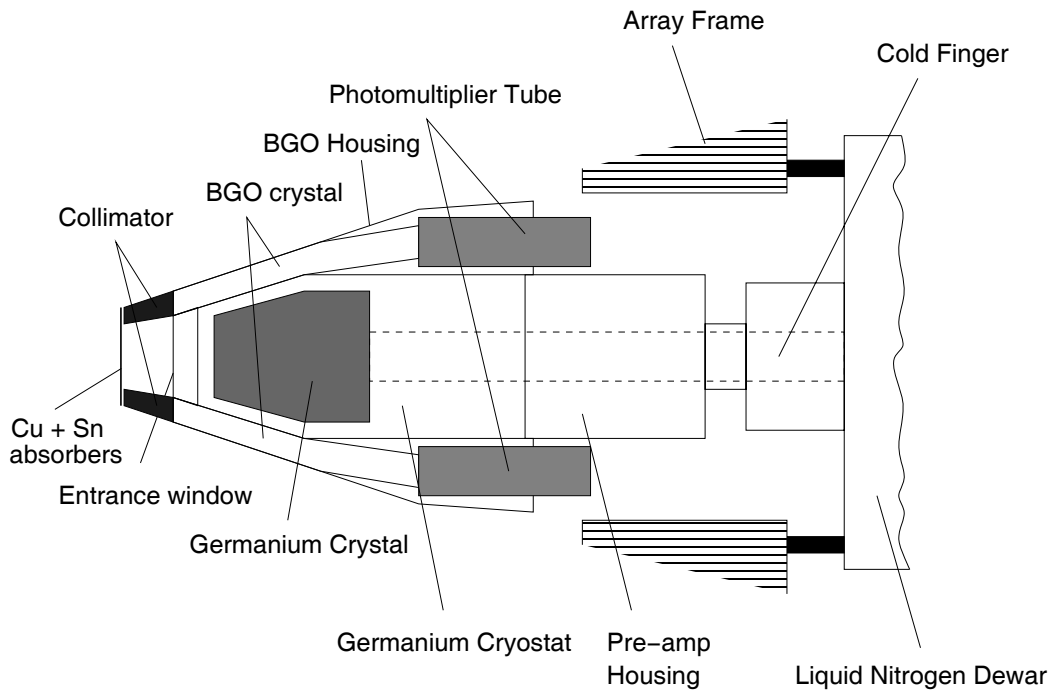
Figure 3.4: BGO shielded HPGe detector as used in the JUROGAM array. Adopted from [60].

(hidden behind JUROGAM in Figure 3.3), it has 27 detectors less in forward direction as compared to the original setup. Nevertheless it covers a large fraction of the 4π solid angle, with a high granularity.

Each of the 43 detector modules is equipped with a high-purity germanium (HPGe) detector, which is surrounded by a bismuth germanate (BGO) scintillation detector for Compton suppression (see explanation below). A schematic diagram of one module is shown in Figure 3.4. The detectors are placed at six positions relative to the beam direction, at 158° (5 detectors), at 134° (10), at 108° (10), at 94° (5), at 86° (5) and at 72° (7). The total photopeak efficiency for JUROGAM is estimated to be 4.2 % at 1332.5 keV.

The germanium detectors are of EUROGAM PhaseI and GASP type [61, 62]. Both are n-type high-purity coaxial germanium detectors, and are similar in structure. Their relative efficiencies at 1332.5 keV are $60 - 70$ % and $80 - 90$ %, respectively, compared to a 3×3 NaI(Tl) detector. In principle, they operate in an energy range of approximately 40 keV to several MeV, but are in practice limited to ≈ 100 keV and 2 MeV. On the low-energy side, the limitation arises from absorption in the 1 mm copper plate in front of the detector (see Figure 3.4). It is mounted to reduce high counting rate in the detector caused by low-energy X rays. At the high-energy side, the restriction comes from the fact that the first 1000 or so of 16384 ADC channels are non-linear. The γ radiation of this study lies mostly in the energy range between 100 and 1000 keV, so for the low-energy γ rays to be at the limit of the nonlinear region, the detectors are set to a full range of 2 MeV. The detectors have resolutions between 2 and 3 keV for the 1332.5 keV ^{60}Co peak.

The Peak-to-Total ratio (PTR) is the ratio of detected events in the photopeak to all detected events in the spectrum. PhaseI or GASP type germanium detectors have a PTR of

a) Vacuum mode   **b) Gas filled (ca. 0.6–0.7 mbar He)**
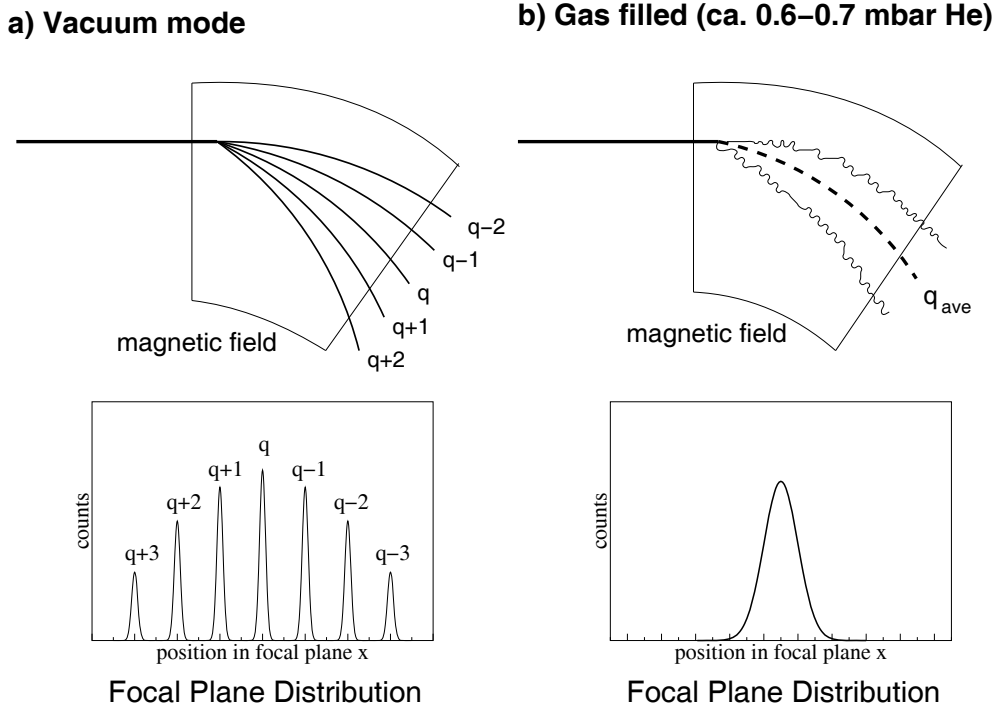
Figure 3.5: Schematic illustration of the operation of gas-filled separators. a) *Vacuum mode* The particles are separated due to their initial charge state. b) *Gas-filled mode* The recoils are scattered by the gas atoms and interchange electrons. The Gaussian distribution at the focal plane is due to a mean charge state produced in the gas.

about 25 % [61]. This value is doubled by the use of Compton suppression shields.

Compton suppression shields comprise bismuth germanate (BGO) scintillation detectors arranged in close geometry around the germanium detectors. They are shielded from direct radiation from the target by lead collimators. The detectors have high efficiency for detection of γ radiation because of the high Z value of BGO. The aim of the shields is to detect escaping γ rays from the detector, and use them to veto signals from the germanium detector. If the BGO shield and germanium detector fire simultaneously, the event in the germanium detector is suppressed, and is not incremented as Compton background in the spectrum.

3.2.2 The Gas-Filled Recoil Separator RITU

RITU (Recoil Ion Transport Unit) is a gas-filled separator situated behind the target. By use of magnetic fields, beam, fission and target-like products are separated from fusion-evaporation residues. The residues, which pass through RITU, are detected in GREAT, the detector setup at the focal plane.

Recoil separators are usually optimised for either (1) high mass resolution or (2) high transmission efficiency, between which a compromise has to be found. Very good mass resolution can be achieved in vacuum-mode recoil mass spectrometers. For example the mass over charge resolution of the Fragment Mass Analyzer (FMA) at Argonne National Laboratory (ANL) is $M/q = 1/340$ at a solid-angle acceptance of $\Omega = 8$ msr [63]. Their drawback is

the low transmission efficiency due to the collection of only up to two charge states (see schematic in Figure 3.5). This is a disadvantage in the production of heavy elements, where cross sections are low and high transmission is needed to obtain good statistics.

Gas-filled recoil separators such as RITU typically have high transmission [64, 65]. In a gas-filled separator, the charge states of the recoils are affected by charge-changing collisions with the gas molecules. For a sufficiently high number of collisions, the charge states are distributed around an average value q_{ave}, which depends the velocity of the ions, the atomic number Z and the type and pressure of the gas (see Figure 3.5). The information of the initial charge state is lost, and the ions follow trajectories according to q_{ave}. For asymmetric reactions as in the case of transfermium production, the transmission rate is up to 40 %. For symmetric reactions it is even higher. As the mass resolution is much worse than in vacuum mode separators, the different reaction channels have to be separated by recoil and recoil-decay identification at the focal plane. In this respect, the clean reactions for nuclei in the region of ^{248,250}Fm is an advantage.

Traditionally an arrangement of DQ_hQ_v is used for gas-filled separators, for example in the Dubna Gas-Filled Recoil Separator (DGFRS) in Dubna and the Small Angle Separator System (SASSY1) at LBNL in Berkeley [64]. Here D stands for dipole and Q_h and Q_v for horizontal and vertical focussing quadrupoles, respectively. The dipole D is positioned as close as possible to the target. On the one hand this reduces drift space to the focal plane, which would increase the image size, on the other hand separation of beam directly behind the target reduces the background at the focal plane.

RITU possesses an additional vertical focussing quadrupole, which is placed between the target and the dipole magnet. The complete configuration is then $Q_vDQ_hQ_v$ (the first quadrupole is hidden behind JUROGAM in Figure 3.3). It is found that this increases the transmission by 30 % for asymmetric reactions as compared with the standard configuration [64].

3.2.3   The Focal-Plane Spectrometer GREAT

The Gamma Recoil Electron Alpha Tagging (GREAT) Spectrometer is situated at the focal plane of RITU and comprises an arrangment of gas, silicon and germanium detectors to measure α, β, and γ radiation. GREAT is designed for isomer and decay spectrometry and enables recoil and decay channel selection in the Recoil-Decay-Tagging (RDT) method described below. Five sets of detectors are in use (see Figure 3.6 and [66]):

1. *DSSSD* Two Double-Sided Silicon Strip Detectors (DSSSD) are the central part of GREAT, where the recoils arriving from RITU are implanted and further decays of α particles and electrons are measured. Each detector has an active area of 60×40 mm^2 and a thickness of 300 μm. The detectors adjoin each other with a separation of 4 mm. They are segmented with a strip pitch of 1 mm in both horizontal and vertical direction, giving 60 channels in x- and 40 channels in y-direction for each detector, and a total of 4800 pixels for both detectors.

2. *MWPC* The Multiwire Proportional Counter (MWPC) is positioned ≈ 20 cm upstream from the DSSSD, at the entrance of GREAT. It is a gas detector of 131×50 mm^2, filled with isobutane, and works as a transmission detector. The energy loss ΔE of the recoiling ions is used to separate them from scattered beam particles and decay products
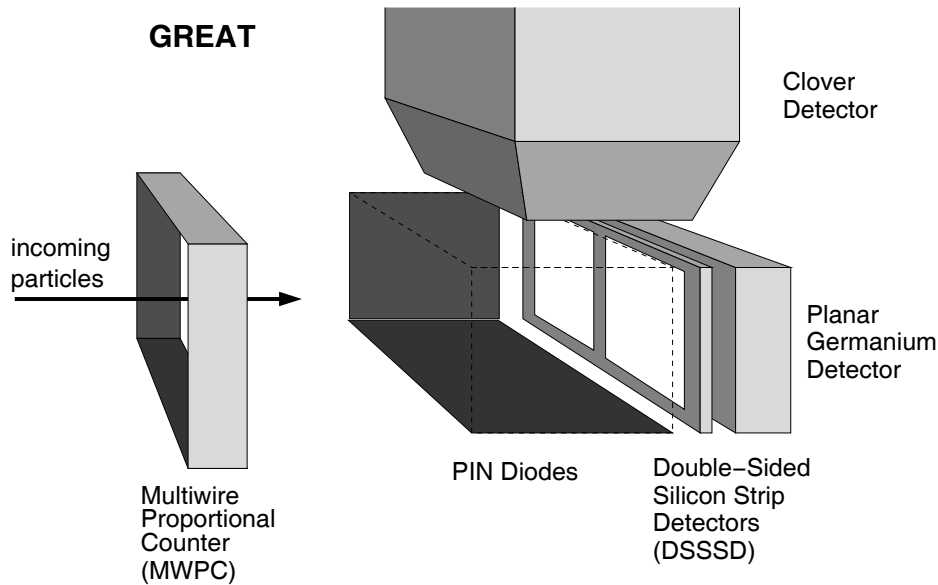
Figure 3.6: Schematic drawing of the focal-plane spectrometer GREAT.

in the DSSSD. Recoils are selected by setting a two dimensional gate on energy loss ΔE versus Time-of-Flight between the MWPC and DSSSD.

3. *PIN Diodes* Twenty-eight silicon PIN diodes are arranged in a box directly in front of the DSSSD, upstream with respect to the beam direction. Each diode has an active area of 28×28 mm^2 and a thickness of 500 μm. The PIN diodes detect conversion electrons and α particles escaping the DSSSD. They have a geometrical efficiency of 30 %.

4. *Planar Germanium Detector* The Planar double-sided germanium strip detector is used to measure X rays and low energy γ rays. It is mounted 10 mm downstream from the DSSSD inside the vacuum, and equipped with a thin beryllium entrance window to minimise the attenuation of the γ and X rays. The detector is rectangular with an active area of 120×60 mm^2 and 15 mm thickness. It has 24 vertical strips at the front side and 12 horizontal strips at the back, with a strip pitch of 5 mm on both faces.

5. *Clover Germanium Detector* A segmented germanium Clover detector is mounted above the vacuum chamber of GREAT for detection of higher-energy γ radiation. The Clover detector contains four germanium crystals with a diameter of 70 mm at the front and a length of 105 mm, and is surrounded by a Compton-suppression BGO shield.

3.3 Spectroscopic Techniques

JuroGam is designed to perform in-beam γ-ray spectroscopy, i.e. spectroscopy of excited states of the fusion-evaporation residue. GREAT in combination with RITU is a powerful tool for decay and isomer spectroscopy. The approaches are complementary, and therefore reveal different parts of the excitation and decay scheme of the nucleus, as can be seen from Figure 3.7.
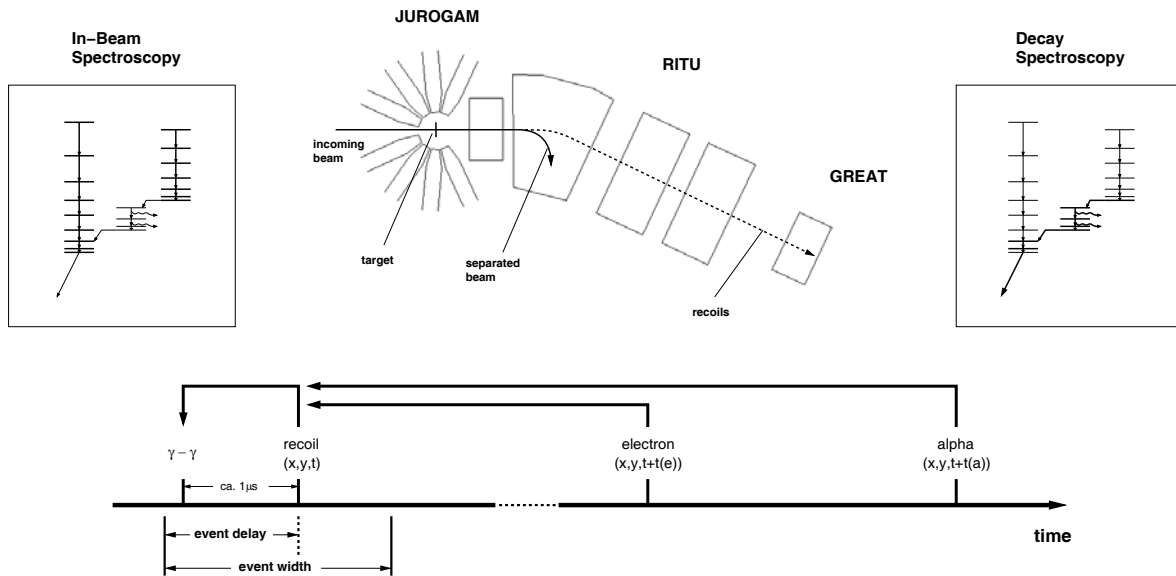
Figure 3.7: Spectroscopic techniques and the RDT technique implemented at the setup in Jyväskylä. Events in JuroGam and great are used to perform in-beam and decay spectroscopy. In the Recoil-Decay-Tagging method (RDT), JuroGam events are correlated to the subsequent recoil implantation and decays in great. Event delay and width in the lower part of the figure correspond to the event definition in the software grain.

In the determination of the α-decay half life at the focal plane, *accidental correlations* have to be taken into account. In order to measure the half life, the α particles are correlated to the preceding recoil in the same pixel of the DSSSD, see Figure 3.8. There are two cases in which random recoil-α pairs are detected: (a) a second recoil or a second α particle is detected in between the recoil event and its subsequent α decay. (b) the recoil was not detected at all, for example because it arrived during the dead time of a detector, so that the α particles are correlated with the wrong recoils.

Due to accidental correlations, the measured exponential decay curve comprises two terms. In the first exponential, corresponding to case (a), the real decay probability λ and the background rate r add up, as the probability for accidental correlation and real correlation are additive. The second exponential, corresponding to case (b), is purely accidental and depends on the background rate r. Following fit formula arises:

$$f(t) = A \cdot e^{(-(\lambda+r)t)} + B \cdot e^{(-rt)} , \tag{3.3}$$

where A and B are fitting parameters.

In-beam γ-ray spectroscopy of very heavy elements suffers from the strong fission cross section. While the fusion-evaporation cross section in the case of the $^{204}\text{Hg}(^{48}\text{Ca}, 2n)^{250}\text{Fm}$ reaction at a bombarding energy of 211 MeV is ≈ 1 μb, the total fusion cross sections are typically of the order of 10-100 mb (see for example [67], Figure 3 for reactions using lead targets). The γ rays of the fusion-evaporation residues are therefore buried under a huge background from fission, and inaccessible even with γ-γ coincidence techniques. Only by fusion-evaporation residue identification in the focal-plane detectors using the so-called *recoil-decay tagging technique* (RDT), the major part of this background can be removed.

(1) recoil implantation   **(2) alpha decay**
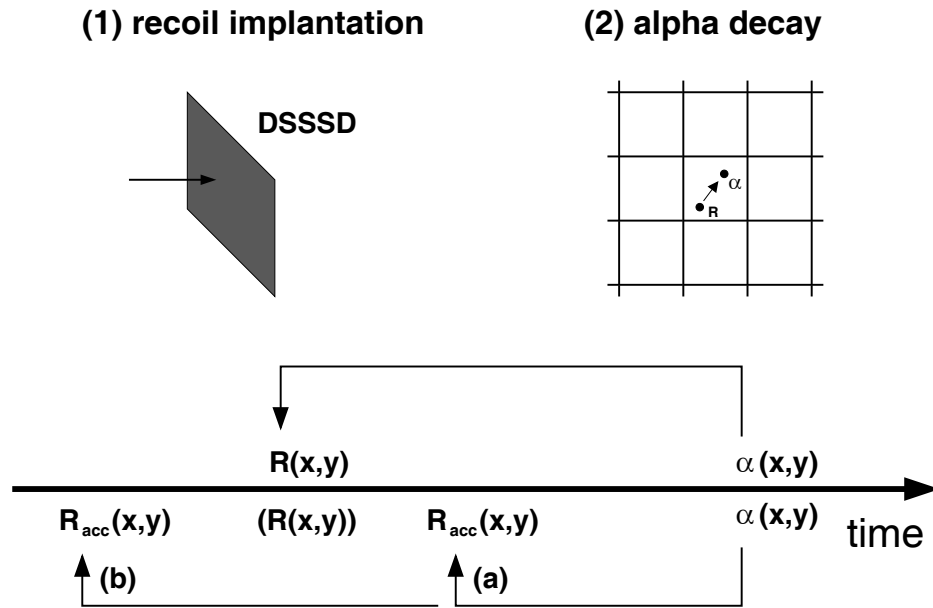
Figure 3.8: Accidental correlation in the assignment of α particle to the preceding recoil event. The α particles are correlated to a previous recoil in the same pixel of the DSSSD for decay half-life analysis and RDT. Accidental correlations occur, if (a) another recoil or α particle have been implanted into the same pixel of the DSSSD in between recoil implantation and its decay, or if (b) the recoil implantation was not detected.

The RDT method is schematically depicted in Figure 3.7. The evaporation residues are separated from the beam in RITU and implanted into the DSSSD. Their flight time through RITU is approximately 1 μs. Recoils are selected from the background of scattered beam, and target-like transfer products arriving at the focal plane by a two-dimensional gate set on a matrix of time of flight between MWPC and DSSSD and energy loss in MWPC. Decay products are identified by anti-coincidence of a DSSSD event with the MWPC.

The recoil signal in GREAT is used as a trigger for events in JuroGam with help of the precisely known flight time of the recoils through RITU. The JuroGam spectra, in which events are correlated to subsequent recoils, are called *recoil gated*. If a further constraint is set on the decay of the recoil, for example by demanding an α decay in the same pixel of the DSSSD, the spectra are *recoil-decay tagged*.

A method was proposed by Jones to investigate nuclei which are in an isomeric state when arriving at the focal plane [68]. This requires an isomeric life time of the order of or longer than the flight time of the recoil through RITU, which is approximately 1 μs. If the conversion coefficients of transitions from the isomeric decay are high, conversion electrons are emitted and can be measured with high efficiency in the pixel of the DSSSD, where the recoil has been implanted. These signals can be summed up and used to determine the half life and a lower limit for the excitation energy of the isomer. The coincident γ radiation in the focal plane germanium detectors can be measured and the decay path of the isomer delineated. The signal can also be used as a *recoil-electron tag* to reveal the structure above the isomer in combination with JuroGam. The method is suitable for heavy elements, because of the Z dependency of the conversion coefficient.
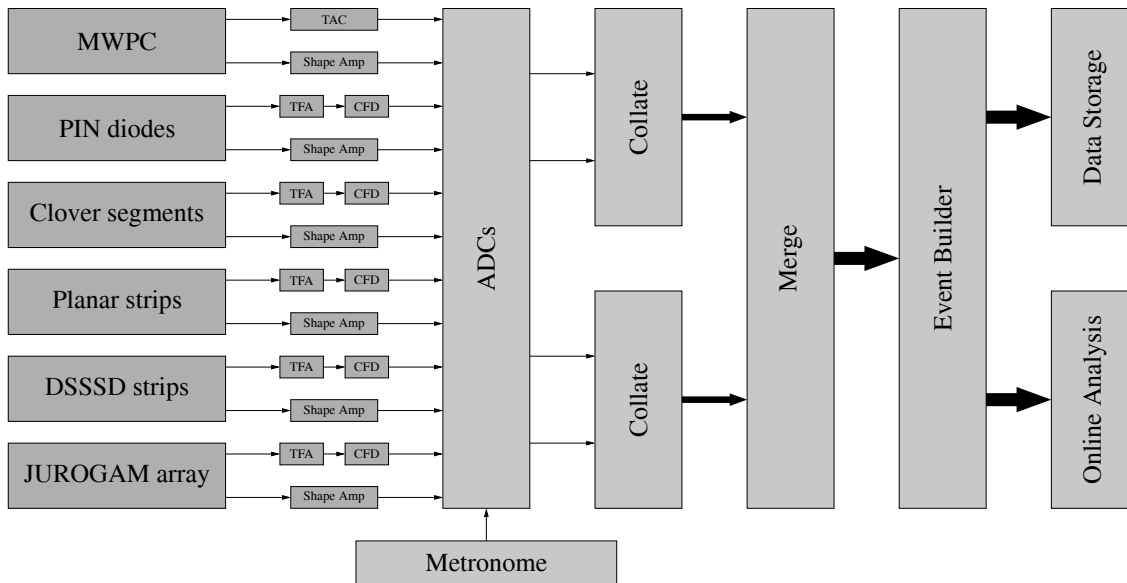
Figure 3.9: Block diagram of the TDR electronics.

3.4 Data Aquisition and Analysis Software GRAIN

Dead time is a main limitation in RDT experiments. The triggerless data acquisition Total-Data-Readout (TDR) method has been developed to overcome this problem by reading out all electronic channels separately. The events are reconstructed and the analysis is performed in the software GRAIN.

Total Data Readout Common dead time data acquisition systems for RDT experiments use a preselected event as trigger. All data is collected, which arrives in a time window after this event, and is written to tape together with the timestamp of the trigger. Detectors at the target position fire approximately 1 μs before arrival of the recoil at the focal plane, which is the flight time through the separator. The time difference is overcome by using delayed coincidence with help of the ADC. This acquisition system has two main disadvantages:

- As the whole acquisition system is busy during readout of the events, the dead time is not negligible. Long gate widths for the study of isomeric states are not feasable because of the increase in dead time.

- During the gate width, all events are read out, real as well as random. Especially for long gate widths at the target position this reduces the quality of the spectra.

These problems are solved in TDR, where all data is read out independent of a hardware trigger, and all events are timestamped separately [69]. The schematic drawing in Figure 3.9 shows how the data is read out by the electronics and further processed.

The signals from the preamplifiers of the detectors are passed to the VXI ADC cards via shaping amplifiers. Typical rates through the system are up to 10 kHz for a single channel, before the resolution gets worse and pile up increases. A time gate is generated by the signal passing the TFA and CFD, which can process events up to a rate of 100 kHz. In the case of a

pile-up event, a second timing signal arrives within the gate window, and the event is marked and can be rejected in the software.

Each VXI card has 32 independent channels, and is equipped with a 100 MHz clock. The clocks are synchronised with help of a metronome, which sends out synchronisation pulses every 655 μs. This allows the outgoing data to be timestamped with an accuracy of 10ns. Simultaneously they are given a tag to indicate from which detector they originate. The time-ordered data items are transfered from the ADCs to the data collate via SHARC links. The data collate bundles the data streams to one stream of time-ordered data per SHARC link. These streams are further bundled to one time-ordered stream in the merge unit.

Events are reconstructed from the data in the Event Builder. The germanium detector signals are associated to BGO signals and Compton-suppressed at this stage. The Event Builder allows filters to be set to reduce the amount of data written to disc. In pure gamma coincidence measurements, the data is triggered by multiple hits in the array. In this work, a signal from any focal-plane detector is chosen as trigger, and data up to 5 μs previously is filtered from the rest of the data. The filtered data is sent to both online analysis and data storage.

GRAIN   Data analysis is performed using the program GRAIN [70]. GRAIN is Java-based software to handle the raw or pre-filtered data produced in the Event Builder of the TDR system. GRAIN creates events out of the data stream, which can be correlated and analysed with help of a sorting code written by the experimentalist. Histograms can be drawn in a graphical users interface for use in online and offline analysis.

The event consists of data in a time window around a trigger. The trigger can be for example the recoil implantation, or any detector signal. The time window is defined by an event width and delay (see Figure 3.7). Piled-up and BGO-vetoed items are either marked or removed. Then the data is assigned their detector type according to the ADC channel, and bundled into an event object.

3.5   Analysis Details

In this section, basic details of the analysis used in both the investigation of ^{250}Fm and ^{248}Fm are presented. The energy calibration of the detectors, their efficiency and the identification of recoils, and gating of the detectors for different purposes are discussed.

3.5.1   Energy Calibration

The JuroGam detectors are operated in a range from $\approx$ 100 keV to 2 MeV, as is explained in Section 3.2.1. The calibration is performed with ^{133}Ba and ^{152}Eu sources. The energies of these sources are given in Table 3.1 together with the relative intensities of the peaks.

The calibration has been performed with a quadratic fit, but excluding the first two peaks at 81.00 keV and 121.78 keV, which lie in the nonlinear part of the ADC. The non-linearity of the ADC is visible in the data as a deviation of the peak energies to the literature values from the Table of Isotopes, which is plotted in Figure 3.10. The deviation can be partly corrected for by adding a damped-sine function to the calibration. The fit can be seen in the same Figure 3.10. The function allows the identification of peaks and assigment of energies down to channel 800.

Isotope	Energy [keV]		Intensity [%]	
^{133}Ba	81.00	0.0030	34.06	0.27
^{152}Eu	121.78	0.0021	28.58	0.06
^{133}Ba	160.61	0.0080	0.65	0.08
^{133}Ba	223.23	0.0120	0.45	0.04
^{152}Eu	244.70	0.0010	7.58	0.19
^{133}Ba	276.40	0.0020	7.16	0.22
^{133}Ba	302.85	0.0010	18.33	0.06
^{152}Eu	344.28	0.0020	26.5	0.4
^{133}Ba	356.02	0.0020	62.05	0.19
^{133}Ba	383.85	0.0030	8.94	0.03
^{152}Eu	411.12	0.0050	2.23	0.04
^{152}Eu	443.98	0.0050	2.82	0.19
^{152}Eu	778.90	0.0060	12.94	0.19
^{152}Eu	867.39	0.0080	4.25	0.19
^{152}Eu	964.13	0.0090	14.61	0.21
^{152}Eu	1112.12	0.0170	13.64	0.21
^{152}Eu	1408.01	0.0140	21.01	0.24

Table 3.1: Gamma-ray energies of ^{133}Ba and ^{152}Eu used for JUROGAM and GREAT Clover calibration [71, 72].
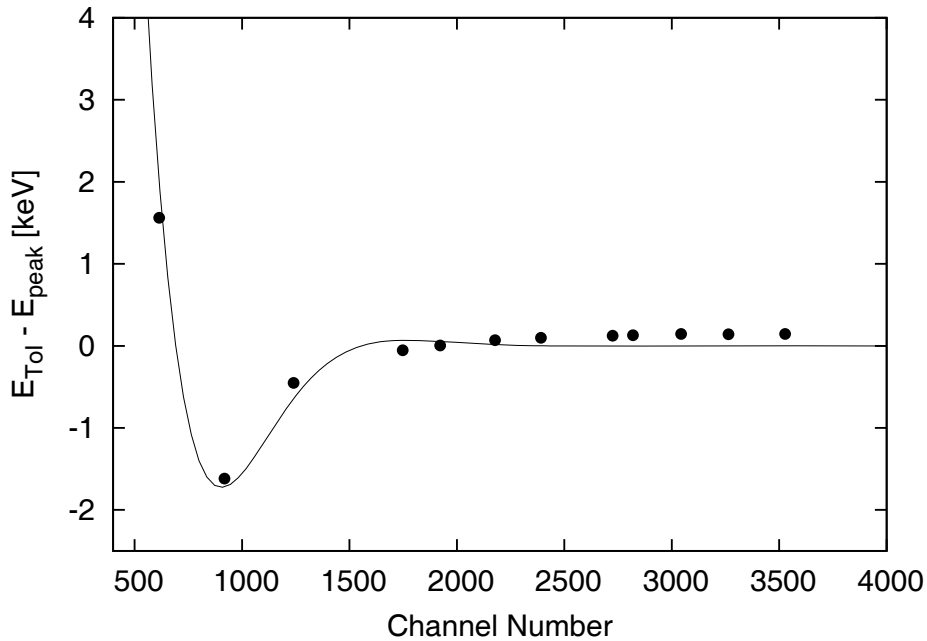
Figure 3.10: Damped-sine fit of the deviation of the calibrated peak energies from the literature values in [71, 72] in the JUROGAM and GREAT Clover calibration. The energies E_{peak} are defined from a quadratic fit to the data excluding the peaks at 81.0 keV and 121.8 keV. Energies above 500 keV are not shown in the spectrum.

A similar calibration procedure is used for the GREAT Clover detector, which is set to the same energy range.

The gain of the DSSSD y side was set to a full range of approximately 20 MeV to be able to detect the fermium recoils and α decay. It is calibrated with an α source containing the three isotopes ^{239}Pu, ^{241}Am, and ^{244}Cm. The source is situated inside the vacuum chamber, and connected to a motor, by which it is moved in front of the detectors if needed. The calibration has following disadvantages, which have to be taken into account:

- The calibration sources have three strong and four weak peaks in between 5100 keV and 5800 keV. The peaks of ^{250}Fm and ^{248}Fm lie at 7430 keV, 7830 keV, and 7870 keV, respectively. Because of the interpolation from the calibration to fermium peaks, a shift and widening results.

- The DSSSD has a dead layer on its surface, which attenuates α particles from the external sources. Thereby, lower calibration energies are measured, and the experimental α-particle energy increases.

- When the nucleus decays inside the detector, the energy of the recoiling daughter nucleus is added to the α-particle energy. While the α emitter of the calibration source is outside the detector, the fermium recoils in the experiment are implanted into the detector. The latter will deliver a higher energy into the detector. For the fermium isotopes, this energy can be estimated:

$$E_{recoil} \approx \left(\frac{m_\alpha}{m_{recoil}} E_\alpha \right) \cdot PHD \,. \tag{3.4}$$

By assuming the α mass m_α to be 4 atomic units, the recoil mass m_{recoil} to be 250 atomic units, α-particle energy $E_\alpha = 7430$ keV and a pulse height defect (PHD) of 50 %, the correction energy is of the order of 60 keV.

These problems can be solved by calibrating the DSSSD with reaction products of known reactions during the experiment. A calibration run was performed in the experiment on ^{248}Fm, with the reaction ^{160}Dy + ^{48}Ca at a beam energy of $E_{beam} = 211$ MeV. But as only one fusion-evaporation channel was open, and the α peaks are well separated, the calibration has been performed only with the three-line α source inside GREAT.

The x strips of the DSSSD detectors are calibrated by conversion electrons from a ^{133}Ba source which is mounted inside the GREAT chamber. In both experiments, a full range of 1 MeV was used. The calibrated spectrum of the combined strips is shown in Figure 3.11. The PIN diodes were set to 600 keV and 7500 keV full range in the ^{250}Fm and ^{248}Fm experiment, respectively, and have therefore been calibrated with the ^{133}Ba source in the former, and the three-line α source in the latter experiment. The barium source was also used to calibrate the Planar detector, which was set to a full range of 400 keV.

3.5.2 Efficiency

The absolute photopeak efficiency of the JuroGam array is a sum of the efficiencies of the single detectors. The latter depend on the internal efficiency of the detectors, and their position in the frame, especially their distance to the target. There are variations in the total efficiency due to missing detectors and the fact, that the internal efficiency is not constant for
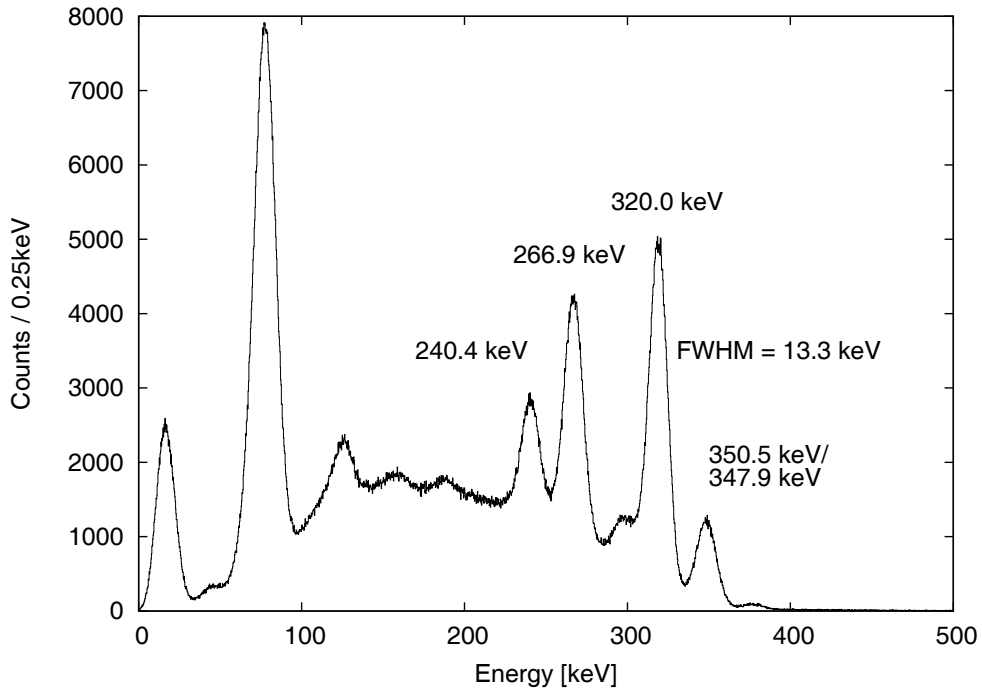
Figure 3.11: Calibrated ^{133}Ba spectrum of the DSSSD x-side detectors. The peaks used for calibration and the Full Width at Half Maximum (FWHM) of the 320 keV peak are indicated in the figure.
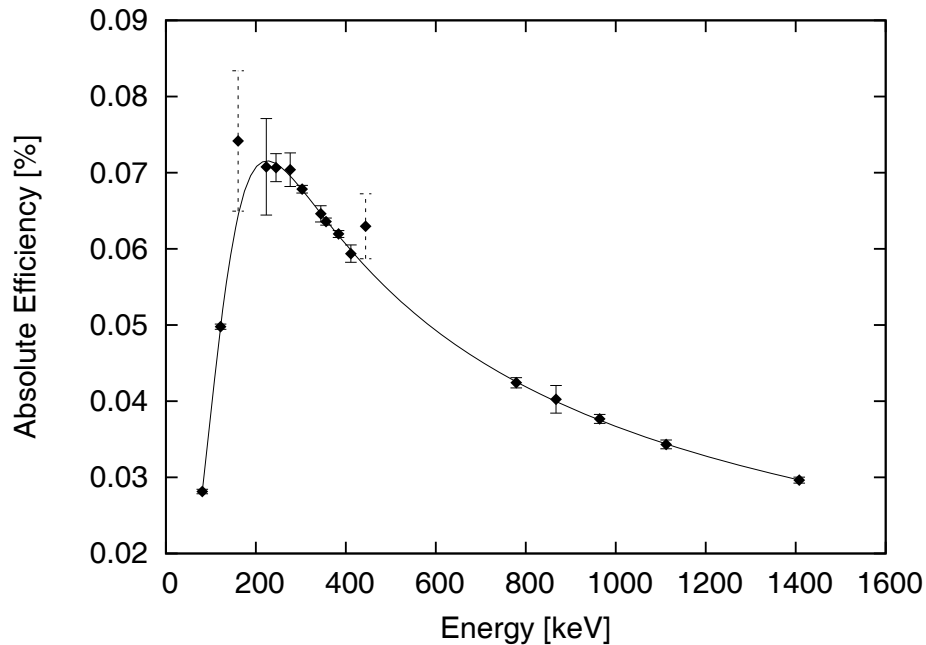
Figure 3.12: JUROGAM efficiency curve measured in the ^{250}Fm experiment. The points at 161 keV and 444 keV (dashed in the figure) have been disregarded, as no proper fit was achieved. Note that 5 detectors were missing in this experiment due to signal problems, which reduces the absolute efficency.
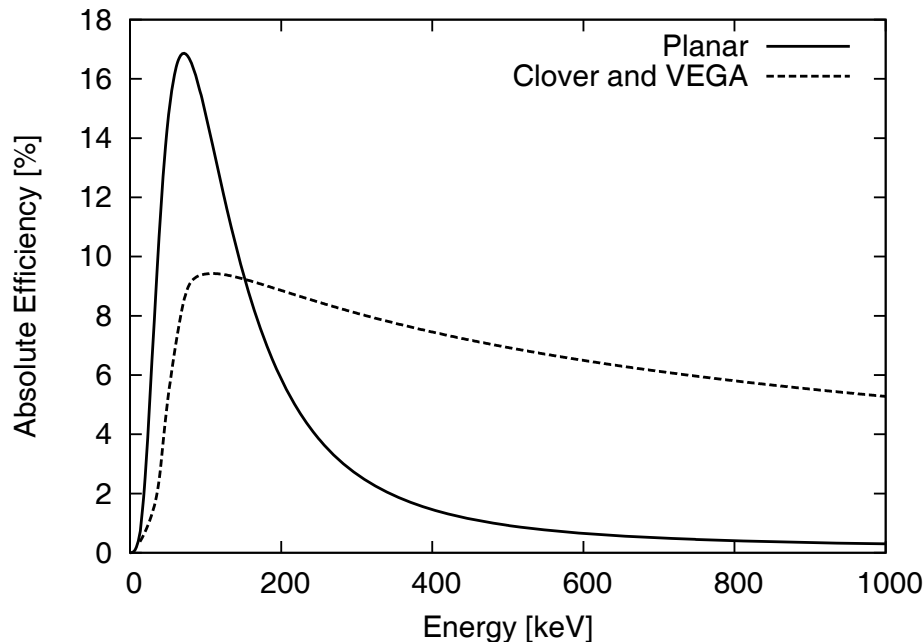
Figure 3.13: Simulation of efficiency curve of Planar and Clover detectors by Andreyev *et al.* [73]. In this graph, the two VEGA type Clover detectors are added with approximately 50 % efficiency as compared to the GREAT Clover efficiency

all detectors. GASP detectors have an efficiency of at least 80 % relative to a $3'' \times 3''$ NaI(Tl) detector, while the one of Phase1 detectors is at least 60 %. The JuroGam efficiency is measured with the calibration sources ^{133}Ba and ^{152}Eu. The peak intensities are given in Table 3.1 together with the energies. The source is positioned in the centre of JuroGam, at target position. The total photopeak efficiency measured in the the ^{250}Fm experiment is shown in Figure 3.12.

The efficiencies of the focal plane germanium detectors are more difficult to measure, as the implantation position of the recoil, and the probability for arriving at this position have to be taken into account. A simple source measurement is thus not sufficient. Instead, an implanted recoil would have to be used. This recoil could be an α emitter with a daughter in an excited state, which decays by at least one γ transition, which collects the whole intensity of the decay. As no such calibration was available, an efficiency curve has been used which was simulated by Andreyev *et al.* [73] using GEANT Monte Carlo simulations [74] (see Figure 3.13).

3.5.3   Recoil Identification and Gating

Accurate recoil identification is of central importance for both recoil-decay tagging and focal-plane spectroscopy. The recoils are identified by setting a gate on a matrix as shown in Figure 3.14. In this matrix, the energy which the recoil loses in the MWPC, is plotted against the time of flight of the recoil, measured between MWPC and DSSSD. As signals from both MWPC and DSSSD are required, decay products detected in the DSSSD are automatically filtered out. Three large areas stand out in the graph: transfer products are situated at relatively long flight times, they are relatively slow. A ridge of scattered beam
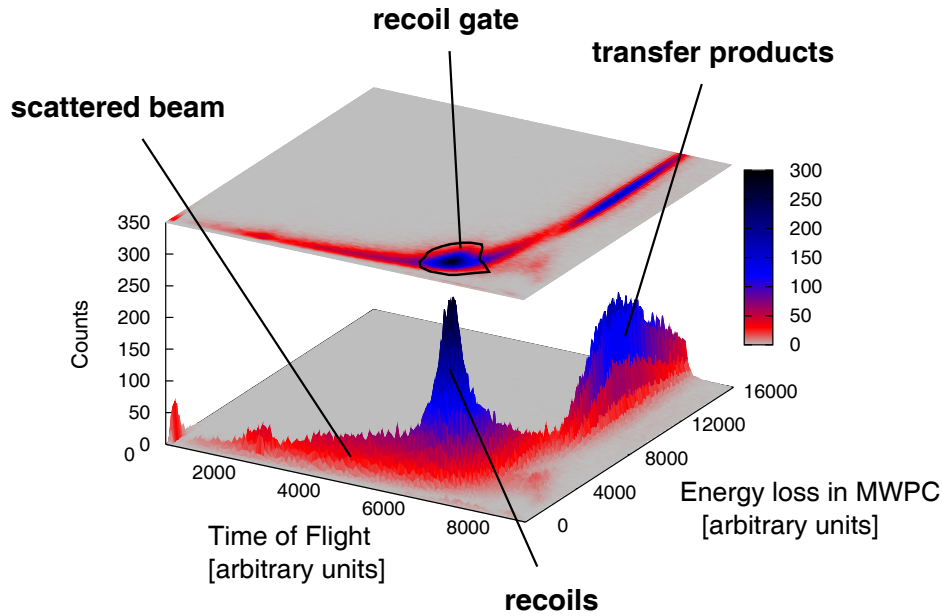
Figure 3.14: Matrix of energy loss in MWPC against time of flight for recoil identification. The position of recoils, transfer products and scattered beam are indicated in the figure. Data and gate are taken from the experiment on ^{250}Fm, but are similar for ^{248}Fm.

particles extends from the transfer products down to small energies and fast flight times. The recoils lie on top of this ridge, such that the gate has to be set as a compromise of maximising the number of recoils and simultaneously minimising the level of background from scattered beam.

Further identification of the recoils can be done by setting gates on subsequent DSSSD events. Electrons and α particles are selected by appropriate gating conditions on time and energy, and requiring anti-coincidence with the MWPC.

The recoils pass the JUROGAM detectors at target position, approximately 0.5 μs to 1 μs before they are implanted into the DSSSD. The time between JUROGAM and DSSSD events differs for each germanium detector because of differences in cable lengths and signal processing. This difference is corrected for by adjusting the time stamps of the JUROGAM detectors. In order to select prompt γ rays from the fusion-evaporation residues, a gate is then set on the corrected time differences (see Figure 3.15, left panel).

In the ^{248}Fm experiment, a gate was instead set on the matrix of the JUROGAM to DSSSD time difference versus time-of-flight between MWPC and DSSSD. The matrix is shown in Figure 3.15, right panel, where RF time structure of the beam is visible. The gate is set to exclude the faster events below the region of recoils, which are caused by beam particles.
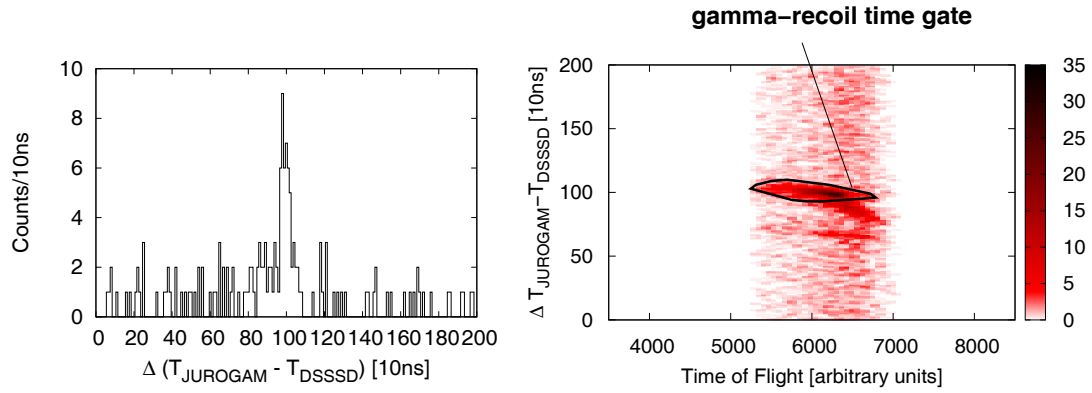
Figure 3.15: Time spectra and gates for prompt γ-ray identification in JuroGam using the recoil-tagging technique. Left Panel: Time difference between JuroGam and recoil event $\Delta T_{jurogam-dsssd}$ for a single detector; right Panel: $\Delta T_{jurogam-dsssd}$ against Time-of-Flight of recoils between MWPC and DSSSD.

Chapter 4

Data Analysis

This chapter covers the analysis of in-beam and delayed spectroscopy of ^{248}Fm and ^{250}Fm. Before elaborating on the analysis of ^{250}Fm and ^{248}Fm in Section 4.3 and 4.4, respectively, previous studies of these two isotopes are shortly summarised, and experimental details of the two experiments described in this work are given.

4.1 Previous Studies of ^{248}Fm and ^{250}Fm

Fermium was discovered in 1952 [75]. Isotopes of mass 250 and 248 were found in 1954 and 1966, respectively [76, 77].

The dominant decay branch in ^{250}Fm is α decay. No β decay branch has been measured, though it was deduced to be < 10 % [78]. The spontaneous fission branch is small, it was measured to be 0.0069(1) % as compared to the α decay branch [79]. The energy and half life of the α decay are $E_\alpha = 7.43(2)$ MeV and $T_{1/2} = 30.4(15)$ min [13, 78]. In the 1970s, a K isomer was discovered by Ghiorso *et al.*, and a half life of $T_{1/2} = 1.8(1)$ s could be determined [18]. In a study by Lazarev *et al.*, an upper limit for the spontaneous fission decay branch of the isomer was given at $b_{sf} \leq 8.2 \times 10^{-7}$. The ground-state band was established up to $I^\pi = 18^+$ by Bastin *et al.* in a detailed study combining results from the conversion-electron spectrometer SACRED and the JUROSPHERE IV array, a predecessor of JuroGam [13]. The results of this work to delineate the exact decay path of the isomer are published in [35].

Structural information on ^{248}Fm is on the other hand scarce. It has two α decay branches of energy 7.87(2) MeV (80 % intensity) and 7.83(2) MeV (20 %), which populate the 0^+ and 2^+ states of the ground state band of the daughter ^{244}Cf [80]. Andreyev *et al.* measured an α-decay branching of $b_\alpha = 93(17)$ % [81]. A small spontaneous fission branch with a partial half life of $T_{sf} = 10(5)$ h was observed by Nurmia *et al.* [80]. Measurements of the total half life gave results of $T_{1/2} = 36(4)$ s [77], 38(4) s [80], 32(6) s [82], giving a weighted average of $\bar{T}_{1/2} = 36(3)$ s.

4.2 Experimental Details

The experiments of this work were performed at the Accelerator Laboratory of the University of Jyväskylä with the setup introduced in the previous chapters. A summary of data

	^{250}Fm	^{248}Fm
reaction	^{204}HgS(^{48}Ca,2n)^{250}Fm	^{202}HgS(^{48}Ca,2n)^{248}Fm
centre-of-target energy	209 MeV	211 MeV
$E^*_{compound}$	24 MeV	26 MeV
average beam intensity	8 pnA	7 pnA
irradiation time	170 hours	170 hours
target material	^{204}HgS (90.5 %)	^{202}HgS (98.5 %)
	^{202}HgS (9.5 %)	
target thickness	510 μg/cm^2 HgS	585 μg/cm^2 HgS
	440 μg/cm^2 Hg	490 μg/cm^2 Hg
target cover/backing	$< 30\mu$g/cm^2 carbon	22 μg/cm^2 carbon
cross section	2 μb	120 nb

Table 4.1: Experimental details of the two experiments on ^{250}Fm and ^{248}Fm.

concerning these experiments including the reaction, centre-of-target energy, beam time on target, and estimated cross section can be found in Table 4.1.

Approximately 13000 full-energy 7.43 MeV α particles from the decay of ^{250}Fm were detected. Assuming a transmission through RITU of 40 %, a recoil coverage of 70 % at the DSSSD, and 55 % α detection efficiency of the DSSSD, this corresponds to a cross section of approximately 2 μb. This value is higher than the one from [13] (see Figure 3.2). The largest source of error comes from the estimation of the average beam intensity, which is based on single measurements during experiments and approximation based on the event and production rates.

In the experiment on ^{248}Fm, a total of 750 full-energy 7.8 MeV α particles were detected. This corresponds to a cross section of 120 nb, when using the same approximations as for ^{250}Fm.

4.3   In-beam and Focal-Plane Spectroscopy of ^{250}Fm

4.3.1   Alpha-Particle Energy Spectrum

The energy spectrum of correlated α-particles in Figure 4.1 contains all events in the DSSSD, which are in anti-coincidence with the MWPC, and which are correlated to a preceding recoil event in the same pixel. The maximum correlation time to the recoil is 110 minutes, well above three half lives of the literature value for ^{250}Fm, which is 30.4(15) minutes. Only a few peaks are present in the spectrum which is a consequence of the fact that fusion-evaporation channels other than the 2n channel are strongly suppressed. The energy of α particles from ^{250}Fm α was measured to be 7490(5) keV, 60 keV above the literature value of 7430(20) keV. This offset matches the prediction given in Section 3.5.1. The α decay daughter of ^{250}Fm is ^{246}Cf, which decays via a 6750.2(10) keV α transition to ^{242}Cm, which emits an α particle of 6112.72(8) keV. The spectrum has been recalibrated using the literature values for the α peaks of the ^{250}Fm decay chain.

The other two marked peaks in the spectrum belong to an α decay chain of ^{248}Fm, which decays by emission of a 7870(20) keV α particle to ^{244}Cf, which emits a 7213(2) keV α particle. These peaks are due to the 9.5 % impurities of ^{202}HgS in the target. One peak at 7570(5) keV
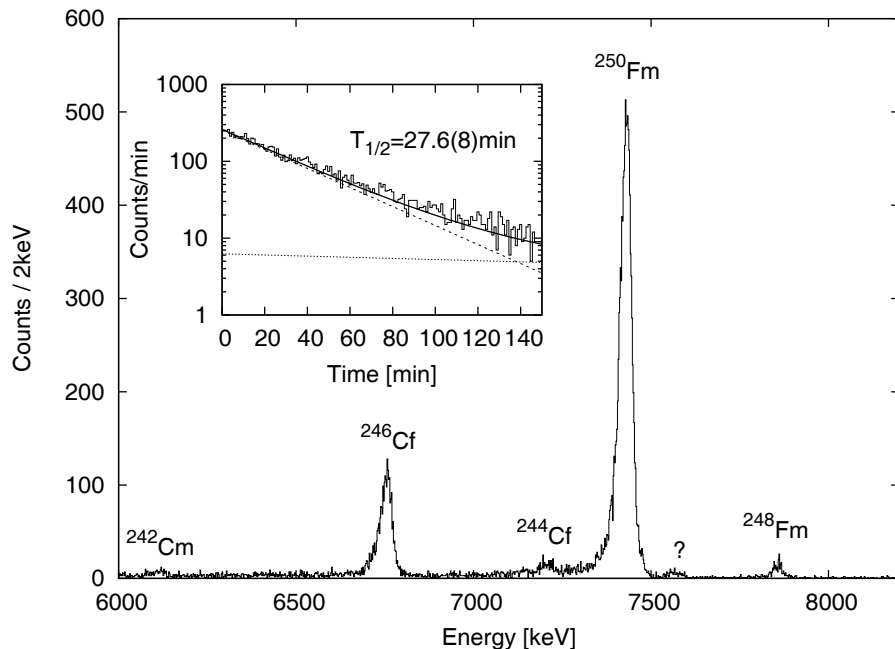
Figure 4.1: Energy spectrum of α particles arriving subsequent to a recoil in the same pixel of the DSSSD within a maximum search time of 110 min. One peak, marked with a question mark, could not be assigned. Inset: Time distribution between recoil and subsequent ^{250}Fm α event. The decay curve is fitted by a double-exponential fit.

is marked with a question mark, as no candidate for this transition energy could be found. The DSSSD was in use only a few times before in 2005, and no candidate for an α particle of this energy was found in the previous reactions. Thus a remaining decay product from a preceding run can be excluded. Note that the energy would be higher by approximately 10 keV, if the peak would be due to a transfer product.

The ^{250}Fm α decay curve is shown in the inset of Figure 4.1. Before fitting the data itself, the background is measured by assigning the α particles to recoils in another pixel, which is 7 pixels left of the one where the α was detected. This is far enough to ensure that the α particles do not originate from the correlated recoil. The measured background rate is $r = 0.00171(3)$ min^{-1}. This rate is fixed in the double-exponential fit of the data according to Equation 3.3. Both exponentials and the final fit curve are drawn on the decay spectrum in Figure 4.1. The measured half life was 27.6(8) min. This is lower than 30.4(15) min [13], but close to the error limits.

4.3.2   Ground-State Rotational Band

The recoil-gated and ^{250}Fm α-tagged γ-ray singles spectra are shown in Figures 4.2(a) and (b), respectively. In a previous experiment, ground-state band transitions from $4^+ \rightarrow 2^+$ to $18^+ \rightarrow 16^+$ were measured by Bastin *et al.* [13]. These transitions are seen in Figures 4.2(a) and (b), together with additional ones at $20^+ \rightarrow 18^+$ and $22^+ \rightarrow 20^+$. Note that the $22^+ \rightarrow 20^+$ transition at 499 keV is only weakly visible in the recoil-gated spectrum, and cannot be distinguished from background in the α-tagged spectrum.
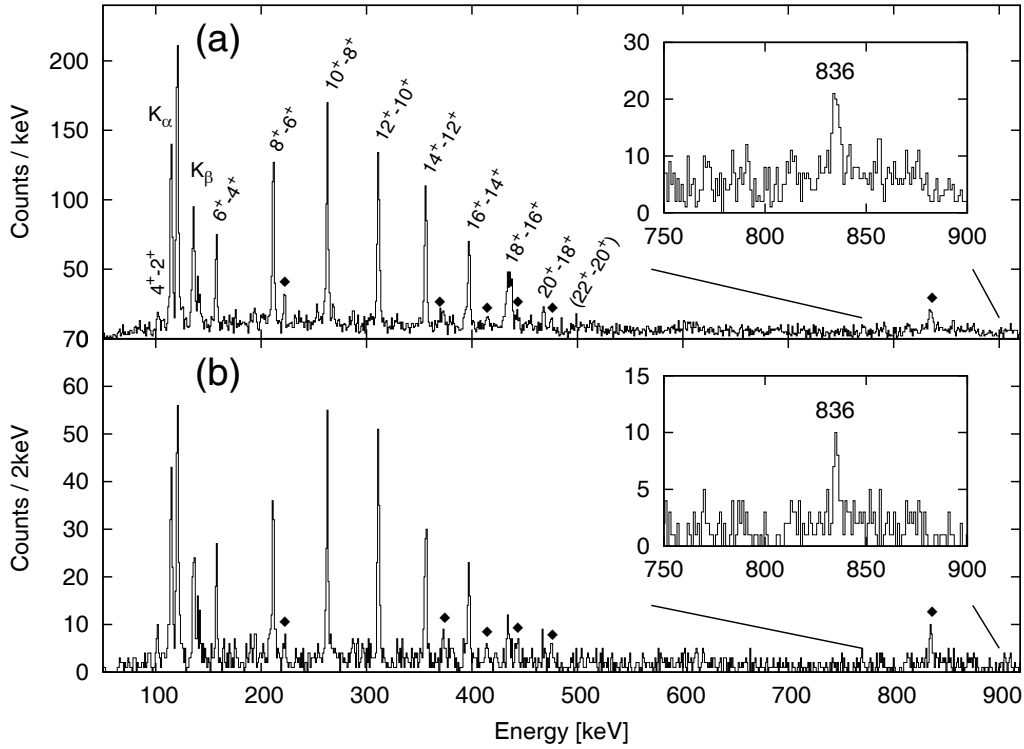
Figure 4.2: JuroGam γ-ray singles spectra of ^{250}Fm. (a) Recoil-gated spectrum; (b) ^{250}Fm-α tagged spectrum. In the insets, the section of the spectra is enlarged, which includes the peak at 836 keV. Peaks which are present in both spectra, but cannot be assigned to the level scheme so far, are marked by diamonds.

In Figure 4.3(a), the total projection of the γ-γ coincidence matrix of recoil-gated Ju-roGam events is shown. The spectrum contains all transitions from the ground-state band seen in the recoil-gated spectrum. In order to confirm that the 499 keV belongs to the band, a sum of γ-ray spectra projected from the γ-γ coincidence matrix with gates on the $4^+ \rightarrow 2^+$ to $20^+ \rightarrow 18^+$ ground-state band transitions is given in Figure 4.3(b). The ground-state band transitions are reproduced, and a clear peak is visible at 499 keV.

The measured peak energies are listed in Table 4.2. The values are taken from fits in the recoil-gated spectrum, except for the 102(1) keV and 435.0(5) keV peak energies, which where measured in the α-tagged spectrum. The peak at 102 keV benefits from the reduced background in the latter, and the 435.0 keV transition is covered by another peak in the recoil-gated spectrum. This is due to a Coulomb excitation peak, exciting the 2^+ state in ^{204}Hg at 436.5 keV [83], which is suppressed in the α-tagged spectrum.

In Table 4.2, the transition energies are compared to the energies measured by Bastin *et al.*. An offset of ≈ 0.5 keV is evident. Our data has been reanalysed several times, the calibration has been checked thoroughly, and other sources for a 0.5 keV offset have been sought. As there was no evident source of error in our measurements, we believe, that our results are correct, and the values given by Bastin *et al.* include an offset of 0.5 keV.

Several peaks are seen in both spectra, which are not members of the ground-state band, and could not be assigned to the level scheme only by the recoil-decay tagged γ-ray spectra. They are marked by diamonds, and their energy is given in Table 4.2. The distinct peak at
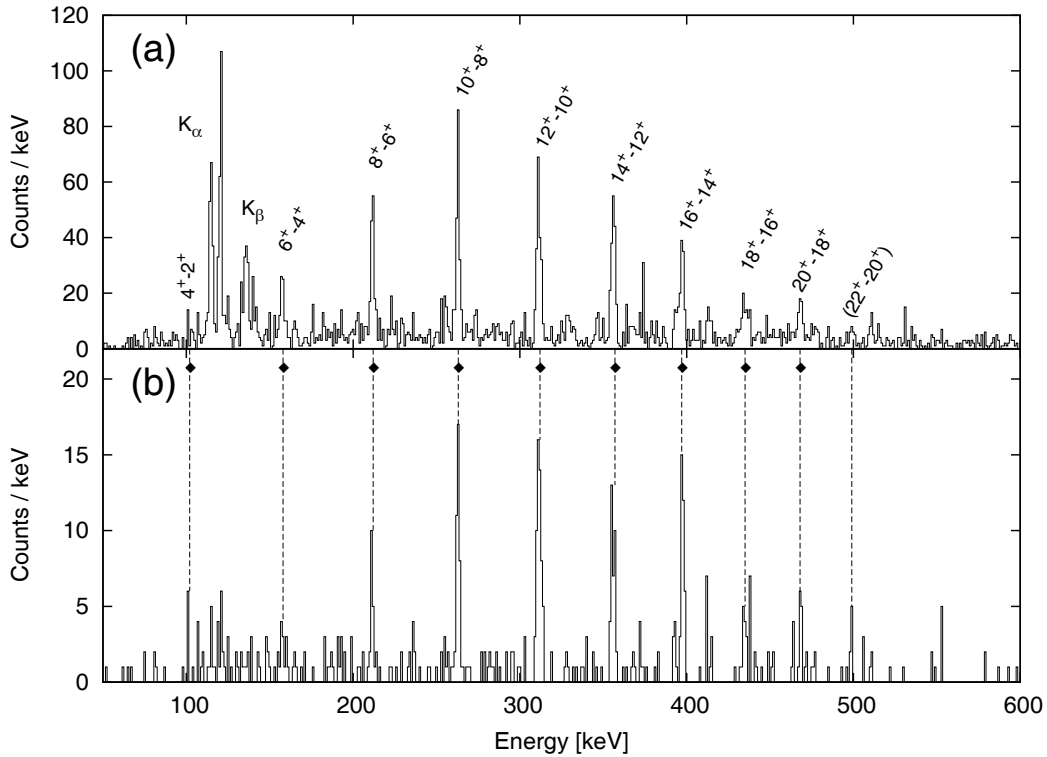
Figure 4.3: Projections of the γ-γ coincidence matrix of recoil-gated JuroGam events: (a) total projection of the γ-γ coincidence matrix. (b) Sum of γ-ray spectra projected from the γ-γ coincidence matrix with gates on the $4^+ \rightarrow 2^+$ to $20^+ \rightarrow 18^+$ ground-state band transitions. In order to guide the eye, the position of the ground-state band are indicated by dashed lines. The gating transitions are indicated by diamonds.

836.3(5) keV is also shown in the insets of Figures 4.2(a) and (b).

4.3.3   Isomer Spectroscopy

In order to confirm the K isomer found by Ghiorso *et al.* (Section 1), and to delineate its exact decay path, conversion electrons following the implantation of a recoil have been used as a tag, as proposed by G.D. Jones (see [68] and Section 3.3).

Figure 4.4 shows the time difference of recoils to correlated conversion electrons in the same pixel of the DSSSD. A correction is made to account for the dead time induced by the read-out electronics. The conversion electrons are detected within an energy range of 40 to 1000 keV. In order to reduce background, a further condition is set, that the recoil-electron pair is followed by a ^{250}Fm α decay. Three structures can be distinguished: a small peak with a measured half-life of 8(2) μs, a larger peak with a half-life of $T_{1/2} = 1.92(5)$ s, and the background distribution, which partly overlaps the 1.92 s peak. The background peak is not fully shown in the figure.

The measured half life of $T_{1/2} = 1.92(5)$ s is in very good agreement with the half life measured by Ghiorso *et al.* of $T_{1/2} = 1.8(1)$ s. The time difference of these electrons to recoil-correlated ^{250}Fm α particles is plotted in Figure 4.5(b), in this case with the electrons arriving within 100 μs and 10 s after recoil implant. A long maximum correlation time of

| This work | | Bastin *et al.* [13] | Transition |
Energy[keV]	Peak Area	Energy[keV]	
102(1)*		100(1)	$4^+ \rightarrow 2^+$
157.9(5)	151(14)	156.9(1)	$6^+ \rightarrow 4^+$
212.0(5)	309(19)	211.3(1)	$8^+ \rightarrow 6^+$
223(1)	63(10)		
263.3(5)	360(20)	262.6(2)	$10^+ \rightarrow 8^+$
311.8(5)	357(20)	311.0(2)	$12^+ \rightarrow 10^+$
356.6(5)	292(18)	355.7(2)	$14^+ \rightarrow 12^+$
374(1)	33(8)		
397.6(5)	190(15)	396.6(2)	$16^+ \rightarrow 14^+$
415(1)	35(8)		
435.0(5)*		434.4(2)	$18^+ \rightarrow 16^+$
444(1)	45(9)		
468.6(5)	55(4)		$20^+ \rightarrow 18^+$
476(1)	33(7)		
499(1)	22(7)		$(22^+ \rightarrow 20^+)$
836.3(5)	71(10)		

Table 4.2: Fit results for the peaks energies in the recoil-gated spectrum. The energies marked by asterisk are taken from fits in the α-tagged spectrum. The energies are compared to ground-state band energies measured by Bastin *et al.* [13]. In the last column, the transition assignments are given.
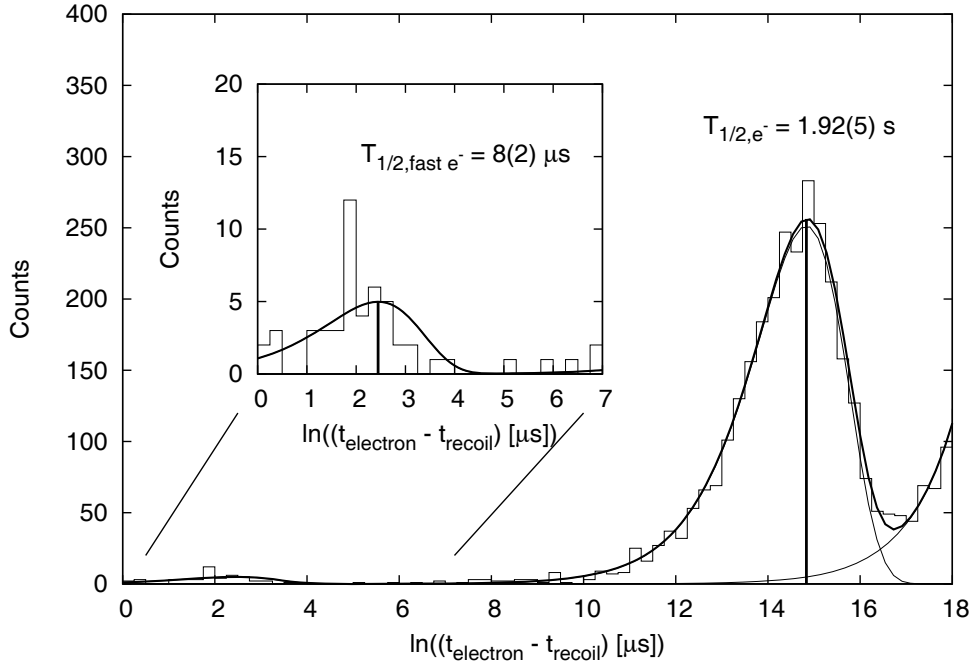
Figure 4.4: Time difference between recoil and recoil-correlated conversion electrons, correlated to ^{250}Fm α decay in the same pixel of the DSSSD. A maximum search time of 110 min is chosen for the recoil-electron-α chain.
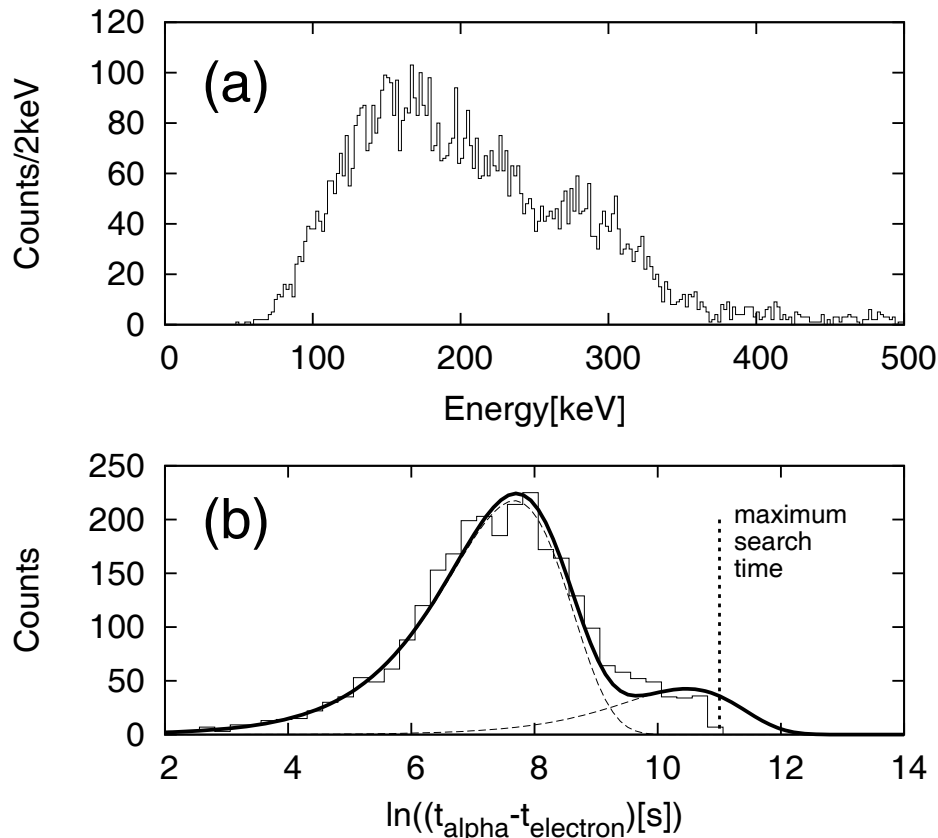
Figure 4.5: Time and energy spectra related to the decay of the 1.92(5) s isomer. (a) Energy of the electrons, which arrive within 100 μs and 10 s after recoil implant. (b) Time difference of ^{250}Fm α particles following recoil-correlated electrons, with a time difference between recoil and electron between 100 μs and 10 s.

1000 min has been chosen to be able to distinguish the true events from accidental background. Clearly, a large peak and a small background distribution can be distinguished, which partly overlap. For the fit, the background rate is fixed to the measured background rate of $r = 0.00171(3)$ min^{-1}, given in the previous section. The fit gives a half life of the peak of 26.5(36) min, which proves the isomer to be from ^{250}Fm, and confirms the measurement of Ghiorso *et al.* The energy spectrum of electrons from the decay of the 1.92(5) s isomer is shown in Figure 4.5(a). The spectrum contains all recoil-correlated electrons with a recoil-electron time difference of 100 μs to 10 s. The population of the isomer can be calculated by comparing the number of correlated electrons to the number of correlated ^{250}Fm α decays. The efficiency of the DSSSD for α particles is estimated to be 55 %. The detection efficiency for electrons is deduced with help of the simulation shown in Figure 4.12, which will be discussed in detail later. The CFD thresholds cut the experimental spectrum at approximately 50 keV, which corresponds to approximately 10 % loss of counts in the simulated spectrum, giving an efficiency of 90(5) %. Altogether 6950(90) electrons were detected subsequent to a recoil, compared to 11500(120) correlated α particles, which gives a population of 37(2) %.

As seen in the inset of Figure 4.4, 94 counts fall within a peak at 8(2) μs. These electrons
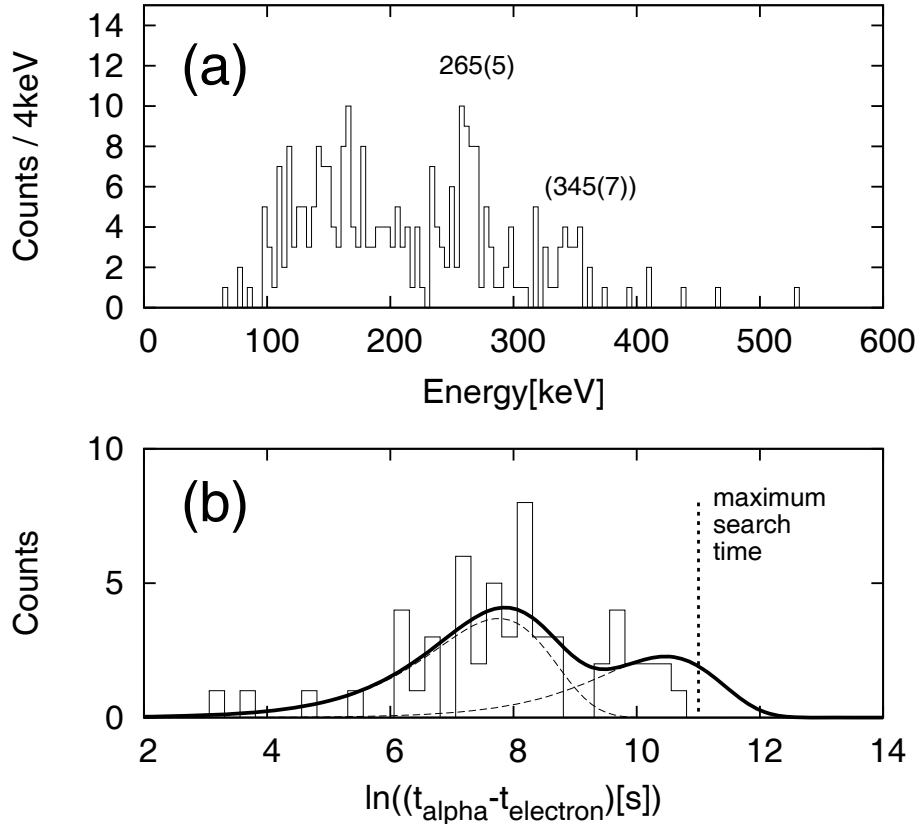
Figure 4.6: Time and Energy spectra related to the fast-electron decay. (a) Electron energy of the electrons, which arrive within 100 μs after recoil implant. (b) Time difference of ^{250}Fm α particles to the second electron e_2^- in the chain of recoil-e_1^--e_2^--α events in the same pixel of the DSSSD. In this chain, the first electron e_1^- arrives within 100 μs after recoil implant, and the second electron e_2^- within 100 μs and 10 s after the first one.

can be correlated to electrons from decay of the 1.92(5) s isomer. Recoil-e_1^--e_2^--α chains in the same pixel of the DSSSD have been investigated, where the first electron event e_1^- is detected within 100 μs of the recoil implantation and the second e_2^- within 100 μs and 10 s after the first one. Furthermore, a ^{250}Fm α particle is required, and as above, a long search time of 1000 min has been chosen, to distinguish between accidental and true correlations. The spectrum of the time difference between e_2^- and ^{250}Fm α particles are shown in Figure 4.6(b). The spectrum comprises two parts, a stronger peak is sitting on the tail of a smaller background distribution. Again, the background is fixed to $r = 0.00171(3)$ min^{-1}. The peak fit gives a half life of 29(6) min, which matches the half life of ^{250}Fm. Together with the correlation to the decay of the 1.92(5) s isomer, this gives strong evidence for the assigment of a new 8(2) μs isomer above the 1.92(5) s isomer.

Electrons following the recoil implant within 100 μs are shown in Figure 4.6(a). The electrons are not correlated to the ^{250}Fm α decay, and contain therefore a larger amount of background.

The electron spectrum has a distinct peak at 265(5) keV, and a smaller one at ≈ 345 keV.
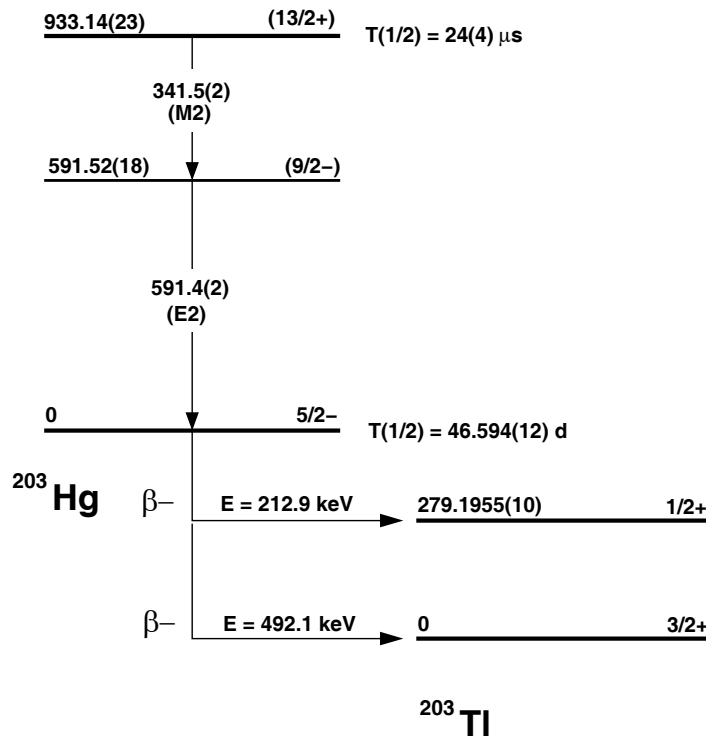
Figure 4.7: Partial level scheme of ^{203}Hg including the $T_{1/2} = 24(4)$ μs isomer [84].

265(5) keV is approximately equal to the K-conversion electrons from the 341.5 keV transition of the $13/2^+ \rightarrow 9/2^-$ M2 isomeric decay in ^{203}Hg, at 258.4 keV. The peak of L conversion electrons would then be at 326-329 keV. This value is lower than the 345(7) keV in the spectrum. However, The L X rays of mercury have an energy of around 10 keV, and have therefore a much higher probability to be absorbed in the DSSSD by photoeffect than the K X rays. Summing of the X rays and the conversion electron energy gives a peak energy of almost 340 keV, which agrees well with the measured value of ≈ 345 keV.

The spectrum of γ-ray singles in the Planar detector, in coincidence with the correlated electrons, is given in Figure 4.8(b). A peak is present at 69 keV, which is assigned to the K X rays of mercury. It should be noted that when correlation with a ^{250}Fm α decay is demanded, both the 69 keV X-ray and the discrete lines in the electron spectrum are no longer visible.

Despite the evidence, that transfer products pass the gate, the decay chains in the DSSSD give strong evidence for a fast isomer in ^{250}Fm. It should be noted, that there is a possibility that the signals could be produced by tails of the recoil signal in the DSSSD.

The population of the 8(2) μs isomer can be estimated from the number of correlated electrons to correlated ^{250}Fm-α particles. In the spectrum of Figure 4.6(a), 220(15) counts are present . From these, 30(6) counts are subtracted, which are estimated to be from the ^{203}Hg isomer. The estimate is based on 5 counts in the 69 keV X ray peak in the Planar spectrum, which has an efficiency of 17 % for 69 keV γ radiation. The total number of electrons can be estimated using the efficiency for electron detection in the DSSSD of 90(5) %, as discussed for the 1.92 s isomer, as well as the fact, that approximately 83 % of the electrons are not detected, as they occur within the dead time of the data acqusition system of approximately 14 μs. Using an α detection efficiency of 55 %, a population of 6(3) % is calculated for the
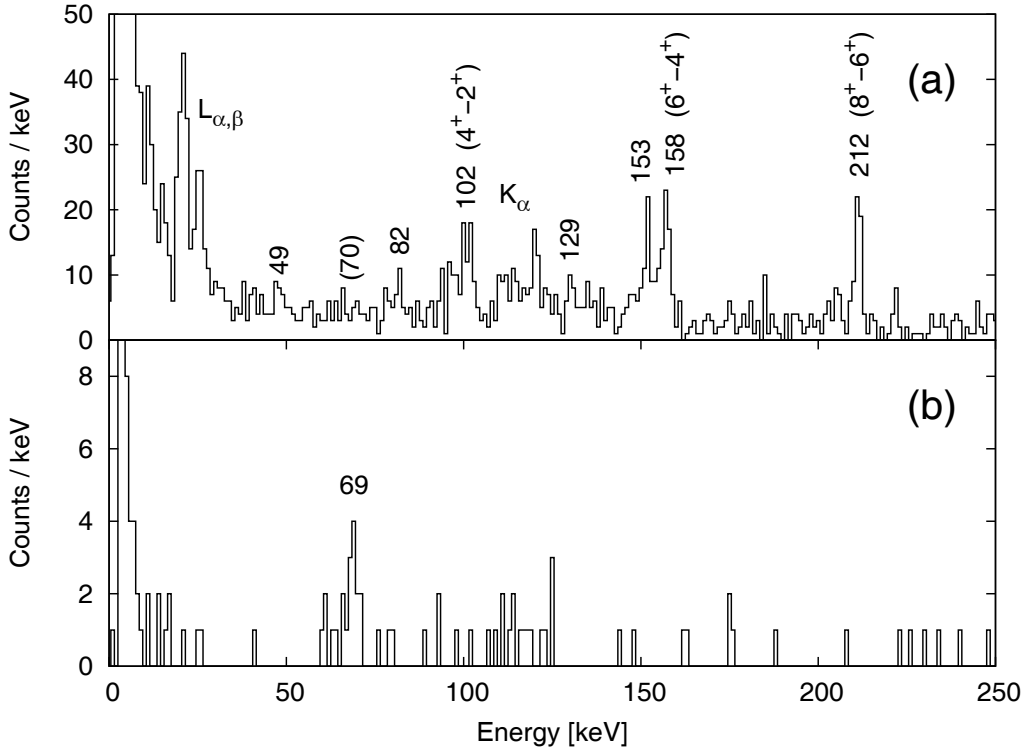
Figure 4.8: Spectrum of γ-ray singles detected in the Planar detector in coincidence with the conversion electrons (a) within 100 μs and 10 s after recoil implant (Figure 4.5(a)); (b) within 100 μs after a recoil implant (Figure 4.6(a)). Peak energies are given with 1 keV precision.

8(2) μs isomer.

In order to delineate the exact decay path of the 1.92 s isomer, γ spectroscopy is used. The γ rays, which are coincident with the conversion electrons in Figure 4.5(a), and detected in the Planar and Clover germanium detectors, are shown in Figures 4.8(a) and 4.9, upper panel, respectively. Fitted values for the peak energies are given in the spectra and in Tables 4.3 and 4.4.

Three peaks in the Planar spectrum, at 102 keV, 158 keV, and 212 keV, are identical to transitions in the ground-state band. In the Clover spectrum, two of these (at 158 keV and 212 keV) are present. These transitions can be assigned to the ground-state band assuming that the isomer decays into it. Furthermore, several high-energy peaks between 680 keV and 880 keV are present in the Clover spectrum, and low-energy transitions in the Planar.

The strongest single lines in the Clover spectrum are at 682.3 keV and 835.6 keV. The peak at 871/876 keV can only be fitted properly assuming a doublet or triplet. The peak strength is thus fragmented over several transitions, and will be discussed later. We interpret the 682.3 keV and 835.6 keV lines to depopulate a $K^{\pi} = 8^-$ isomer and a $K^{\pi} = 2^-$ intermediate state, respectively, as will be explained in the following.

The 836 keV transition is visible in both the prompt recoil-gated and α-tagged spectra (Figure 4.2). This means that the transition decays from a state which can be populated either directly in the reaction and which decays promptly, or through the isomer and is detected delayed. Consequently, it must depopulate an intermediate structure below the isomer. The 682.3 keV transition, on the other hand, is not present in the prompt spectra even though it
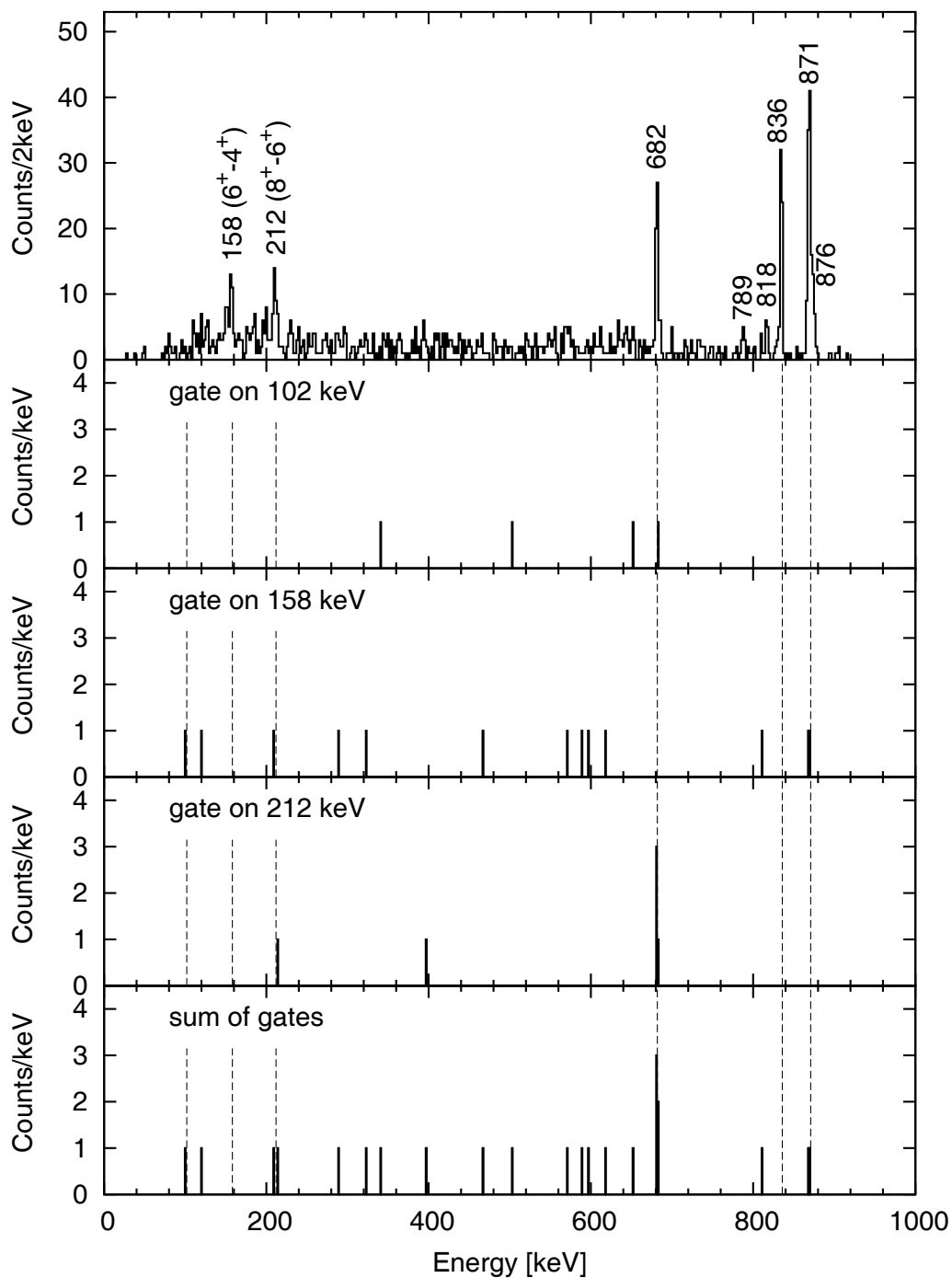
Figure 4.9: Upper Panel: Spectrum of γ rays detected in the Clover germanium detectors coincident with the summed conversion electrons. Peak energies are taken from fits, and have a precision of 1 keV. Lower Panels: Conversion-electron tagged spectra of γ rays in the detectors, which are coincident with the γ rays in the Planar detector of energy indicated in each spectrum.

Energy [keV]	Peak Area	Assignment
49(1)	12(4)	$4^- \to 3^-$
82(1)	6(3)	$7^- \to 6^-$
102(1)	17(5)	$4^+ \to 2^+$
129(1)	9(4)	$6^- \to 4^-$
153(1)	29(6)	$7^- \to 5^-$
158(1)	31(6)	$6^+ \to 4^+$
212(1)	18(5)	$8^+ \to 6^+$

Table 4.3: Fit results of the peaks in the electron-α tagged Planar spectrum. Proposed assignments are shwon in the right-hand column.

Energy [keV]	Intensity		Assignment
	of fit	corrected	
152(1)	14(4)	756(250)	$7^- \to 5^-$
158(1)	25(6)	1223(280)	$6^+ \to 4^+$
212(1)	27(6)	641(138)	$8^+ \to 6^+$
682.3(5)	50(7)	820(120)	$8^- \to 8^+$
789(1)	9(3)	155(58)	$6^- \to 6^+$
818(1)	10(3)	181(61)	$4^- \to 4^+$
835.6(5)	50(7)	897(128)	$2^- \to 2^+$
871(1)	100(11)	1803(190)	$7^- \to 6^+$
			$3^- \to 2^+$
876(1)	21(6)	383(103)	$5^- \to 4^+$

Table 4.4: Fit results of the peaks in the electron-tagged Clover γ-ray spectrum. Intensities corrected for internal conversion and efficiency of the detector are given in the third column (see Figure 3.13 for the efficiency curve). Proposed assignments in the right column.

is roughly as intense as the 836 keV peak in the conversion-electron tagged Clover spectrum. It very likely decays from the isomer directly, not from an intermediate state which could be populated in-beam.

The ground-state band transitions in the conversion-electron tagged Planar spectrum (Figure 4.8), are used as a gate for γ rays detected in the Clover. The gated Clover spectra are displayed in the lower panels of Figure 4.9. Lines are inserted at the ground-state band transition energies at 102 keV, 158 keV, 212 keV, and at 682.3 keV, 836 keV, and 871 keV (the strong isomeric transitions), in order to guide the eye. A clear peak at 682.3 keV is present in the spectrum gated by 212 keV, the $I^\pi = 8^+ \to I^\pi = 6^+$ transition. Therefore, the 682.3 keV peak feeds into the ground-state band at spin $I^\pi = 8^+$. If it fed in below the 8^+ state, the 212 keV transition would not be seen, and if it fed in above the 8^+ state, the next-higher ground-state band transition at 263 keV would be present in the Planar spectrum. From the area of the 212 keV peak of 27(6) counts, and an efficiency of the Planar of 5.3 % and 3.5 % for the 212 keV and 263 keV transition, respectively, a peak intensity of 18(4) counts would be expected in the latter case.

In Section 2.2, it was discussed that transitions of low multipole order are strongly favoured over transitions of high multipole order. A transition feeding the 8^+ state may be expected to have $E1$ or $M1$ character. For transitions of $E1$ or $M1$ multipole order, the spin selection

rules of Equation 2.17 allow a spin change of $\Delta I = 0, 1$. This restricts the possible spins of the isomer to $I = 7$, 8, or 9. Of these possibilities, $I = 7$ and $I = 9$ can be ruled out by arguments based on the transition strength.

If the isomer had a spin of $I = 7$, one would expect a transition of similar strength to the 6^+ member of the ground-state band. The ratio of the intensities of the $7 \to 6^+$ and $7 \to 8^+$ transitions can be expressed in terms of the the transition probabilities T^{fi} and efficiencies $\epsilon(E)$:

$$\frac{A^{fi}(7 \to 6^+)}{A^{fi}(7 \to 8^+)} = \frac{T^{fi}(7 \to 6^+) \cdot \epsilon(E_{7 \to 6^+})}{T^{fi}(7 \to 8^+) \cdot \epsilon(E_{7 \to 8^+})}, \tag{4.1}$$

From Equation 2.15 one can find that the ratio of the two depopulating transitions equals to the ratio of the corresponding energies cubed, assuming that the transition strengths are identical. The energy of the $7 \to 6^+$ transition would be $(682.3 + 212.0) = 894.3$ keV. The intensity of the 682.3 keV peak is measured to be 50(7) (see Table 4.4). Using Equation 4.1, the intensity of the 894.3 keV peak would then be approximately 100 counts. The transition would be clearly seen in the spectrum of Figure 4.9, upper panel. As it is not present, the $I = 7$ assignment is unlikely.

The assigment of $I = 9$ can be dismissed by a similar argument. In this case, one would expect a transition to the 10^+ state with an energy of $(682.3 - 263.3) = 419.0$ keV. The intensity of the 419.0 keV peak would be approximately 14 counts. Even though this value is much smaller than the one expected for $7 \to 6^+$, it is still of similar intensity to the peaks at 789 and 818 keV. The peak should be easily seen in the spectrum. As it is not, the $I = 9$ assignment can also be ruled out.

Consequently, the isomer is assigned spin 8. A negative parity can be assigned by comparing the experimental results to calculated two-quasiparticle states, as will be discussed in Section 5.4. Thus, it can be concluded, that the 682.3 keV transition decays from the isomer with $K^\pi = 8^-$ into the 8^+ member of the ground-state band.

The remaining peaks are assigned to the decay of the isomer through an intermediate structure with $K = 2^-$. The high-energy transitions seen in the Clover spectrum depopulate the intermediate structure, while the low-energy transitions seen in the Planar spectrum connect members of the band built on top of the state. The complete level scheme is given in Figure 4.10. The 836 keV peak is seen in both prompt and delayed spectroscopy. It is also the strongest peak in the Clover spectrum, and therefore interpreted as depopulating the band head. The other high-energy transitions are not present in the prompt spectrum, but only in the delayed one. A possible explanation arises from the fact that the intermediate state must be strongly non-yrast. Therefore, mainly the lowest members of the band are directly populated in the reaction, and most of the intensity is collected in the band head. In the decay of the isomer, a higher-spin member of the band is populated, from which the decay goes through many levels of the band. A transition from a higher-lying band member to the ground-state band is therefore more likely.

Combining the information of the remaining transitions (see fits in Tables 4.3 and 4.4), the exact structure of the intermediate band can be determined. The levels from 4^- to 7^- are fixed by coincidence measurements, energy sums and transition strength arguments:

The 871 keV transition must decay into the ground-state band at spin 6^+ or below, as otherwise the initial state would lie above the isomer. On the other hand, the transition is in coincidence with the 158 keV $6^+ \to 4^+$ transition of the ground-state band (see Figure 4.9). As a consequence, it is placed feeding into the 6^+ level.
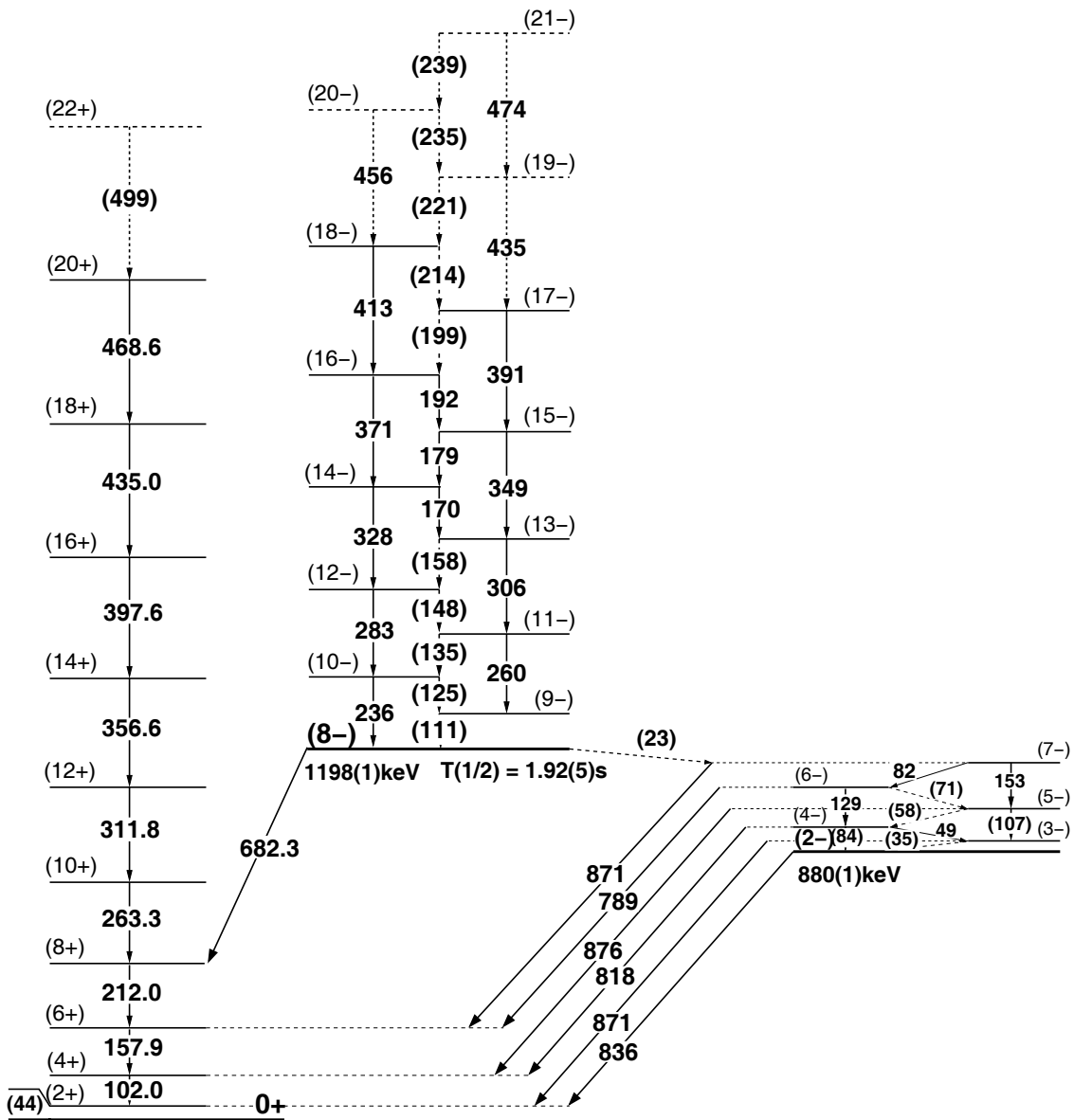
Figure 4.10: Experimental level scheme of ^{250}Fm. Energies of transitions above and below the 1.92(5) s isomer, which are given in brackets, are calculated from the assigned transitions. In the ground-state band, the transition at 44 keV is deduced from a spin fit (see Section 5.3), and the transition at 499 keV is weakly visible in the recoil-gated spectrum and assigned based on the systematic of ground-state band transitions.

In three cases, the energies can be added up to consistent sums:

- $(789 + 82) = 871$ keV and 871 keV.

- $(153 + 876) = 1029$ keV, and $(871 + 158) = 1029$ keV.

- $(129 + 818) = 947$ keV and $(789 + 158) = 947$ keV.

These energy sums fix the intraband $E2$ and $M1$ transitions at 153 keV, 129 keV and 82 keV, and the interband transitions at 789 keV, 818 keV, 871 keV, and 876 keV, between the intermediate and ground-state band.

Using the fact that the interband transitions decay into the 4^+ and 6^+ levels of the ground-state band, the initial state of the 871 keV transition can be fixed at a spin of either 7 or 6, assuming only the lowest multipole orders for the interband transitions, i.e. either $M1$ or $E1$. If the initial state of the 871 keV transition would have spin $I = 6$, the 789 keV transition would decay with spins $I = 5 \rightarrow 6^+$ from the intermediate band to the ground-state band. Another transition would be possible with spins $I = 5 \rightarrow 4^+$ and energy $(789+158) = 947$ keV. It would have the same multipole order and even higher energy, and should be seen in the spectrum. As it is not, this assignment is unlikely. Similar considerations can be made for the 876 keV and 818 keV transitions.

These arguments confine the band-head spins of the intermediate band to $I = 0, 1, 2, 3$. A spin of $I = 2$ is determined based on transition strength arguments and the rotational formula:

If we assume, that $I = 3$ is the band head spin of the intermediate band, two transitions to the ground state band are possible, $3 \rightarrow 4^+$ and $3 \rightarrow 2^+$. If the 836 keV peak stems from the $3 \rightarrow 4^+$ transition, the $3 \rightarrow 2^+$ transition would have an energy of $(836 + 102) = 938$ keV. Using Equation 4.1 and reducing the ratio of the transition probabilities to the ratio of the cubes of the transition energies, an intensity of 66 counts can be estimated for this peak. If we assume the 836 keV to be the $3 \rightarrow 2^+$ transition, the $3 \rightarrow 4^+$ would have an energy of $(836 - 102) = 734$ keV and an intensity of 35 counts. Neither of these peaks are seen in the spectrum, and the $I = 3$ assignment is therefore dismissed.

If we assume $I = 1$ to be the band head spin, two transitions $1 \rightarrow 2^+$, and $1 \rightarrow 0^+$ would be seen. If the 836 keV peak was due to one of these transitions, the strength of the other can be estimated with help of the Alaga rules [85]. The Alaga rules state that the ratio of transition probabilities from two interband or two intraband transitions do not depend on the microscopic structure of the bands. Therefore, they reduce to the ratios of Clebsch-Gordan coefficients representing the transitions, which are nearly identical for the transitions discussed. If the 836 keV transition were a decay to the 0^+ state, the $1 \rightarrow 2^+$ transition would have a peak energy of $(836 + 44) = 880$ keV. A peak area of 36 counts can be estimated with help of the efficiency curve, the peak intensity of the 836-keV peak, and the Alaga rules. If the 836 keV transition were a decay to the 2^+ state, the $1 \rightarrow 0^+$ transition would have an energy of $(836 - 44) = 792$ keV and the peak area is estimated to be 69 counts. As neither of these peaks are seen with this strength, the $I = 1$ assignment can also be ruled out.

If the band-head had a spin $I = 0$, the 836 keV transition could not decay into the $I^\pi = 0^+$ state of the ground-state band, as the transition is forbidden. Assuming a $0 \rightarrow 2^+$ transition, the head of the intermediate band would lie $(818 + 102 - 836) = 84$ keV below the $I = 4$. This is too low for a regular continuation of the band, assuming a smooth rotational behaviour according to Equation 2.27. Spin $I = 2$ is thus the only remaining candidate for the band

Energy [keV]	Peak Area	Assignment
170(1)	6(3)	$16^- \to 15^-$
179(1)	8(4)	$15^- \to 14^-$
192(1)	8(4)	$14^- \to 13^-$
236(1)	11(4)	$10^- \to 8^-$
260(1)	32(6)	$11^- \to 9^-$
283(1)	4(3)	$12^- \to 10^-$
306(1)	12(4)	$13^- \to 11^-$
328(1)	13(4)	$14^- \to 12^-$
349(1)	19(5)	$15^- \to 13^-$
371(1)	13(4)	$16^- \to 14^-$
391(1)	19(5)	$17^- \to 15^-$
413(1)	10(4)	$18^- \to 16^-$
435(1)	20(5)	$19^- \to 17^-$
456(1)	5(3)	$20^- \to 18^-$
474(1)	8(4)	$21^- \to 19^-$

Table 4.5: Fit results of the transitions of the $K = 8$ band in the recoil-electron tagged JUROGAM γ-ray singles spectrum in ^{250}Fm. The third column gives the proposed assignment of the transitions.

head of the intermediate band. In this way, the 49 keV peak can be assigned as a $4^- \to 3^-$ $M1$ transition, and the moment of inertia behaves smoothly.

The assignment of the intermediate states, which is made above and presented in the level scheme in Figure 4.10, is supported by comparison to ^{250}Cf, which has 2 protons less and two neutrons more than ^{250}Fm [86]. This nucleus has a $I^\pi = 2^-$ state at 871 keV as compared to 880 keV in ^{250}Fm, and the depopulating γ-ray transitions have very similar energies, for example of 829 keV for the $2^- \to 2^+$ transition to the ground-state band as compared to 836 keV in ^{250}Fm. Lately, further high-K structures with 2^- intermediate bands have been found in isotones of ^{250}Fm, as will be discussed in Section 5.6.

The isomer decays via two branches, one of which goes directly to the ground-state band through the 682.3 keV transition, the other through an intermediate band. The branching ratio can be calculated by adding up the intensities of the interband transitions in Table 4.4 (including the conversion electron contribution and corrected for efficiency), and comparing to the strength of the 682.3 keV transition. 20(3) % of the intensity decays directly to the ground state band.

4.3.4 Rotational Band above the $K^\pi = 8^-$ Isomer

Transitions in the rotational band above the $K^\pi = 8^-$ state, which are excited in the reaction and decay promptly, can be studied using the recoil-electron tagging technique introduced in Section 3.3. The recoil-electron tagged γ-ray singles spectrum obtained with JUROGAM is shown in Figure 4.11. The electrons are restricted to arrive in a time window of 100 μs to 10 s after a recoil implantation, which elects the conversion electrons from the 1.92(5) μs isomer.

A series of regularly-spaced peaks are seen in the spectrum. The fit results are given in Table 4.5. The spacing lies between 19 keV and 25 keV, which is half of the spacing of the peaks in the ground-state band. Therefore, the peaks can be assigned to $E2$ transitions,
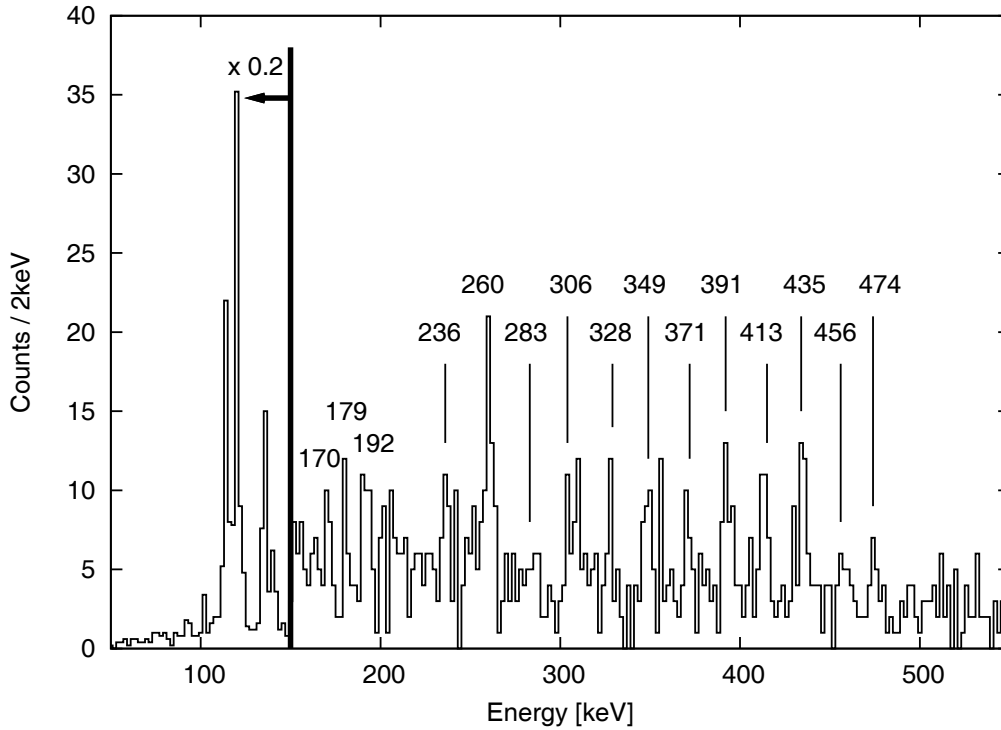
Figure 4.11: Recoil-electron tagged JuroGam γ-ray singles spectrum. The γ rays arrived in a time window of 100 ns approximately 1 μs before recoil implantation in the DSSSD. The recoils are followed by conversion-electron events between 100 μs and 10 s after recoil event in the same pixel.

which form the two signature partners of a rotational band built above the $K^\pi = 8^-$ isomer. The lowest transition has an energy of 236 keV, assuming a smooth continuation of the band. Otherwise the next lowest transition should be seen, at an energy and with a strength estimated as follows:

The transitions of the signature partner containing the peaks at 260 keV, 306 keV, 349 keV, 391 keV, 435 keV and 474 keV are populated more strongly than the other signature partner. On average, the transition intensity is 2.1(4) times the intensity of neighbouring transitions in the other signature partnerband, after correcting for the JuroGam efficiency. The 260 keV transition is even 4.3(18) stronger than its neighbours. The separation between the peaks of the two signature partners varies between 19 and 25 keV. Assuming a smooth continuation of the band, the next transition would be expected between 218 and 212 keV. It would have a peak strength in the spectrum of at least 22(10) counts, calculated from the 237 keV transition intensity, increased by a factor of 2.1(4). As it is not seen, 236 keV has to be the lowest transition of the band, and decays to the $I^\pi = 8^-$ state. The assignment of the other transitions follows accordingly and is given in Table 4.5.

Three peaks can also be found at lower energies, at 170 keV, 179 keV, and 192 keV. 170 keV and 179 keV sum to 349 keV, which equals the energy of the 349 keV $E2$ band transition, and 179 keV and 192 keV sum to 371 keV, which equals the energy of the 371 keV $E2$ transition. These peaks are likely to be $M1$ transitions connecting the two signature partners of the band. With help of the $M1$ transitions, the relative position of the two signature partner bands is

fixed, and the remaining $M1$ transitions between the signature partners can be calculated, which are given in brackets in Figure 4.10.

4.3.5   Simulation of the $K^\pi = 8^-$ Isomer-Decay Spectra

A simulation has been made based on the code CALOBRANCH by R.D. Herzberg. The input file contains transition energies and branching ratios as well as the K and $L1$-$L3$ internal-conversion coefficients. Using this data, single cascades are simulated, and the DSSSD, Planar and Clover spectra incremented with conversion-electron, X-ray and γ-ray events from the cascade. The simulation is based on the level scheme in Figure 4.10, where the transition energies are taken from the measurements in Tables 4.3 and 4.4, or, if not seen in the measurement, calculated with help of the known transitions. The branching ratios are chosen as follows: the isomer decays with a probability of 20 % via the 682.3 keV transition directly to the ground-state band, and with 80 % through the intermediate band, which corresponds to the experimental results. The $M1$ to $E2$ branching ratios of the intermediate band are calculated from the transition probabilities in Equations 2.51 and 2.45, which are expressed in terms of reduced transition probabilities $B(M1)$ and $B(E2)$. A gyromagnetic ratio of $g_K = -0.125$ has been used in the expression of $B(M1)$, based on a two-quasiparticle $(5/2^+[622]_\nu \otimes 9/2^-[734]_\nu)_{2^-}$ assignment for the intermediate state, which is discussed in Section 5.4. An electric quadrupole moment of $Q_0 = 1265$ fm^2 is used in the expression of $B(E2)$, as explained in Section 5.4.2. The probability for an intraband transition from the intermediate to the ground-state band is set to 30 %, adjusted to fit best the experimental Clover and Planar spectra. The simulation is repeated 7000 times corresponding to the number of electrons in the spectrum. The probability for detection of single electrons is chosen to be 65 %, giving best agreement of the simulated to the experimental electron spectrum. A substantial number of electrons are expected to escape the DSSSD because of the finite implantation depth of the recoils. The simulated DSSSD summed-electron, and Planar and Clover γ-ray singles spectra are shown in Figures 4.12(a), (b), and (c), respectively. Note that the Clover and Planar spectra are not coincident with detected electrons, but raw ungated singles spectra.

The spectra are reasonably well reproduced and support the proposed level scheme. The electron spectrum has two larger structures centered around 150 keV and 280 keV, which is similar to the experimental spectrum in Figure 4.5(a). There is a third electron distribution centered around 50 keV, which is not seen in the experimental spectrum, as they lie below the constant fraction discriminator (CFD) threshold. The Planar spectrum is dominated by the three ground-state band transitions. In comparison to Figure 4.8, the 82 keV and 152 keV intraband transitions are also present, and the K-X rays and the 129 keV transition are visible. Other intraband transitions have fewer counts, and are overwhelmed by the Compton background from higher-lying peaks in the experimental spectrum. The L-X ray intensities are clearly overestimated, which could be caused by an overestimation of the efficiency in the lower energy part of the simulated efficiency curve of Figure 3.13. Considering the intensities of the interband transitions at high energy, the Clover spectrum agrees well with the experimental spectrum in Figure 4.9(a). The 871/876 keV peaks constitute the largest peak of the spectrum, 836 keV and 682 keV slightly smaller and almost identical in strength, and 818 keV and 789 keV clearly smaller, even though still larger than in the experimental spectrum. The ground-state band transitions at 212 keV and 158 keV have much larger strength than in the experimental spectrum, which could again be caused by the overestimation of the efficiency
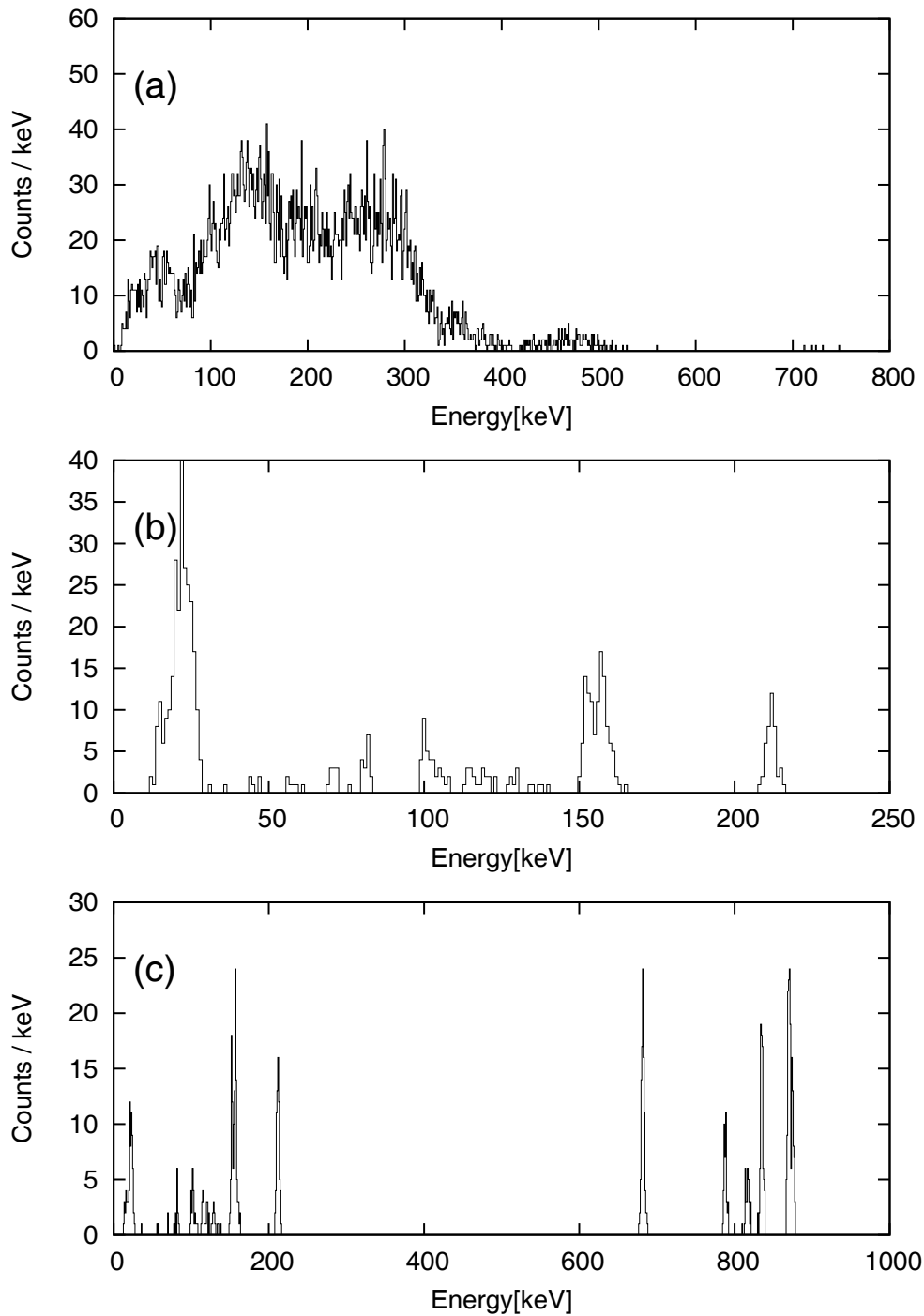
Figure 4.12: Simulated electron and γ-ray spectra for the decay of the $K = 8$ isomer in ^{250}Fm using CALOBRANCH. (a) Conversion electron spectrum in the DSSSD, (b) γ-ray singles spectrum in the Planar germanium detector, and (c) γ-ray singles spectrum in the Clover germanium detector. The simulated spectra should be compared to the experimental spectra in Figures 4.5(a), 4.8(a), and 4.9, respectively.
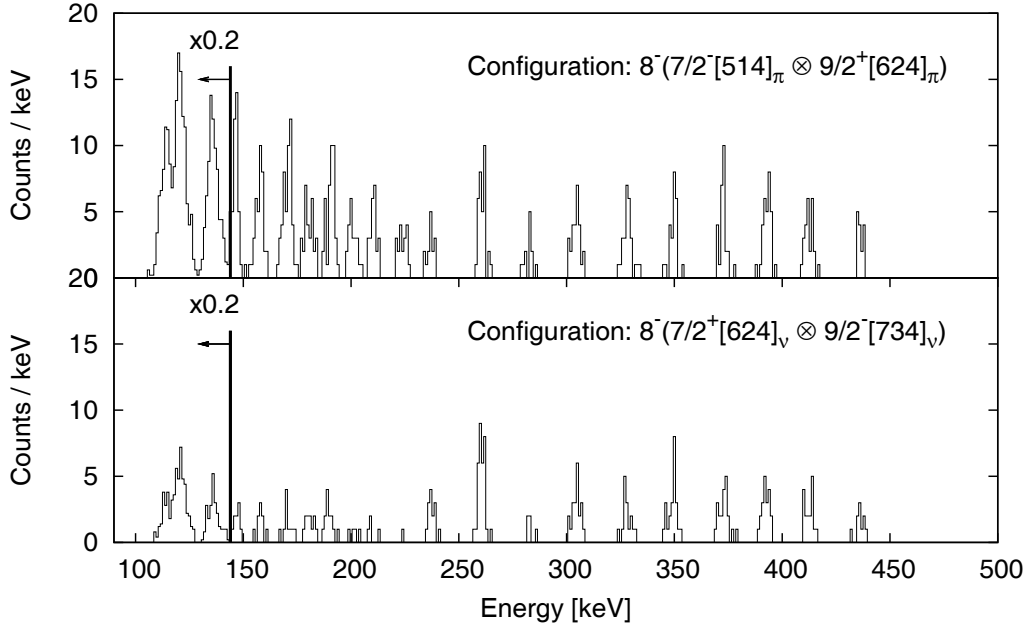
Figure 4.13: Simulated JuroGam γ ray singles spectra of the band built on top of the $K = 8$ isomer in ^{250}Fm. The calobranch code has been used, and branching ratios have been derived for a 2-proton quasiparticle assignment of the isomer (upper panel), and 2-neutron quasiparticle assigment (lower panel). The number of repetitions was chosen such that the intensity of the peak at 260 keV agrees with experiment.

for lower energies. The efficiency curves for the focal plane detectors bear uncertainties, as they are based only on simulation (see Figure 3.13), and efficiency simulation is made for the great Clover only, and the contributions of the VEGA Clovers added by assuming 50 % of the great Clover efficiency each.

A large source of uncertainty for the simulation is the above-mentioned simulated efficiency curve. Another source is the branching in the band built on the 2^- intermediate state, which is calculated for a pure 2-quasiparticle excitation. In the discussion section it will be outlined, that it is a collective octupole state with a dominant 2-quasiparticle structure. This would change the $B(M1)/B(E2)$ ratios of the band built on top of it. Furthermore the feeding out of the band is set to 30 %, which is an adjustment to the experimental spectrum. Compton scattering is not taken into account at all, which increases the background and covers small peaks in the spectrum. It should also be noted, that the γ-ray spectra are not electron-tagged. With an electron efficiency below 100 %, the probability for detecting a γ ray depends on the number of conversion electrons in the whole cascade, which is not taken into account here. Despite the rough estimates, the simulation agrees well with experiment and supports the level scheme.

Using the same code, the band built above the $K^\pi = 8^-$ isomer has been simulated up to spin 19^-. The simulations are shown in Figure 4.13. The energies are taken from the level scheme in Figure 4.10. The $E2$ transitions are taken from the fit values of the peaks. The

relative position of the signature partners is fixed by the three $M1$ transitions seen in the experimental spectrum, which allowed calculation of the remaining $M1$ energies. The feeding of the band members is estimated based on the intensity ratio of the ground-state band. The band-head configuration is assigned to either the two-proton $8^-(7/2^-[514]_\pi \otimes 9/2^+[624]_\pi)$, or the two-neutron $8^-(7/2^+[624]_\nu] \otimes 9/2^-[734]_\nu)$ quasiparticle state, shown in the upper and lower panel of the figure, respectively. They are two possible two-quasiparticle assignments for the $K = 8$ isomer, as will be discussed in Section 5.4. The $T(M1)/T(E2)$ branching of the transitions is calculated based on these configurations. The simulations were repeated until the largest peak of the spectrum at 260 keV has an intensity identical to the experimental one.

In the simulation based on the 2-quasiproton assignment, the contribution of $M1$ transitions is much greater than in the experimental spectrum, which makes this assignment unlikely. The spectrum based on the 2-quasineutron assignment on the other hand agrees nicely with experiment. The three $M1$ transitions at 170, 179, and 192 keV are stronger than the rest, though still weaker than the $E2$ transitions, and with similar strength than in experiment. In the experiment, the $E2$ transitions have a characteristic intensity distribution, with the transition at 236 keV and 283 keV much weaker than the 260 keV transition. This is reproduced in the simulation. The K-X rays are underestimated by approximately 50 %. 280 K_α and 116 K_β-X rays are present in the simulation compared to 429 K_α and 152 K_β-X rays in the experiment. This might be due to unknown transitions feeding the band.

4.4 In-beam and Focal-Plane Spectroscopy of ^{248}Fm

4.4.1 Alpha-Particle Energy Spectrum

Figure 4.14 shows a spectrum of events correlated to the implantation of a recoil in the same pixel of the DSSSD within a maximum search time of 200 s. The data were obtained through the ^{202}HgS$(^{48}$Ca,2n$)^{248}$Fm reaction, as described in Section 4.2. Only two peaks are present, belonging to ^{248}Fm and its α decay daughter ^{244}Cf.

The α decay of ^{248}Fm was previously studied by Nurmia *et al.* [80], and two α decay energies were assigned, 7.87(2) MeV (80 % intensity) and 7.83(2) MeV (20 %). The measured peak energy of 7915(10) keV lies approximately 50 keV above the weighted mean value, within errors equal to the expected offset of 60 keV deduced in Section 3.5.1.

In the inset of Figure 4.14, the time between recoil event and subsequent ^{248}Fm α particle is shown. The background in this spectrum is measured in the same way as for ^{250}Fm, by correlating recoil and α particle of different pairs of pixels (see Section 4.3.1). A background rate of 0.00086 min^{-1} is deduced, almost half of the rate measured in the ^{250}Fm experiment. The half life is measured within the first 150 s of the decay curve. As only 3 background counts are expected in this interval, the background rate can be neglected, and a single-exponential fit is sufficient. It is shown together with the data in the inset of Figure 4.14. From the fit, a half life of 32.3(1.5) s is measured, which is an improvement to the previously known half-life of 36(3) s.

The second peak at an uncorrected energy of 7266(10) keV belongs to ^{244}Cf, the daughter of ^{248}Fm. ^{244}Cf decays mainly via α decay with energies of 7174(4) keV (25 % intensity) and 7214(2) keV (75 %) [87]. In this case, the offset is $\approx$ 60 keV of the mean value, which is similar to the estimated value in Section 3.5.1. ^{244}Cf has a long half life of 19.4(6) min, far
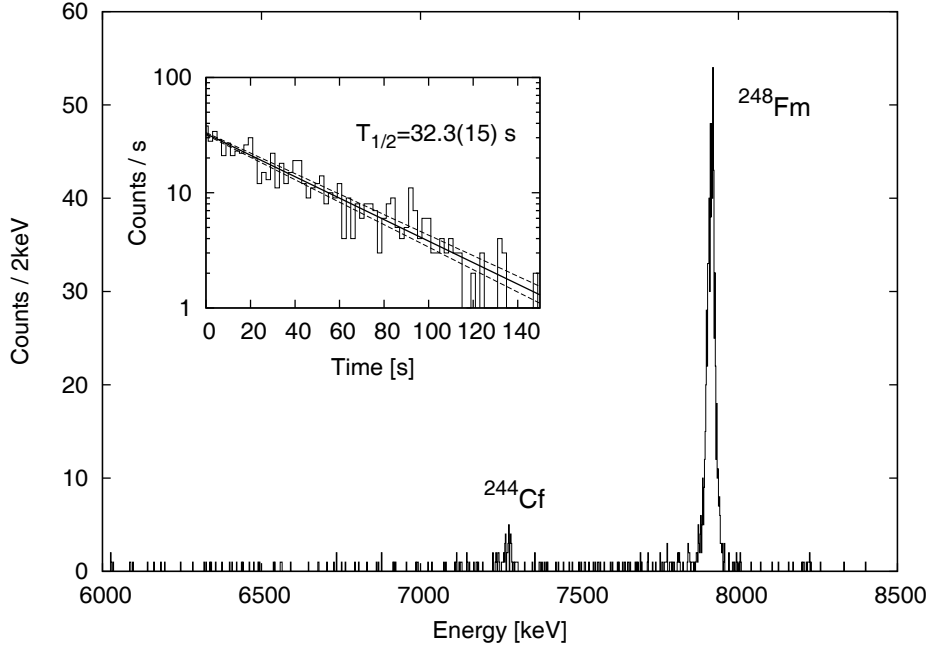
Figure 4.14: Spectrum of events correlated to a recoil arriving in the same pixel of the DSSSD within a maximum search time of 200 s. Inset: Time distribution between recoils and subsequent ^{248}Fm α particles, fitted by a single exponential.

longer than the maximum correlation time. As a consequence, its intensity in the spectrum is weak, even though fission branching is weak and no β decay has been measured so far.

4.4.2 In-beam Spectroscopy

Recoil-gated and α-tagged γ-ray singles spectra from JUROGAM are shown in Figure 4.15(a) and (b), respectively. The spectra are dominated by a sequence of peaks, which are evenly spaced and can be assigned to the ground-state band. The peak energies and intensities are taken from fits in the recoil-gated spectrum, and are listed in Table 4.6. In Figure 4.15(c), the recoil-gated sum-of-gates spectrum is drawn with gates on the first five transitions of the proposed band, 165 keV, 221 keV, 274 keV, 323 keV, and 369 keV. The statistics are very low, but the spectrum is almost free of background, so that almost all γ-ray events up to 500 keV are measured at the position of the proposed band members or K X rays.

Four transitions are observed in the recoil-gated spectrum, which do not belong to the ground-state band. They are marked by diamonds in the spectrum, and their fitted energies are given in Table 4.6. Of these peaks, only the one at 181 keV is coincident with transitions in the ground-state band, as seen from the sum-of-gates spectrum.

In order to determine the spins of the ground-state band, the spin-fitting method introduced by Wu $et\ al.$ has been used [88]. The fitting method is based on the phenomenologically-derived energy-spin relation in a rotational band found by Holmberg and Lipas [89]:

$$E(I) = a\left[\sqrt{1 + bI(I+1)} - 1\right] . \tag{4.2}$$

Here, a and b are fit parameters. The formula takes into account the deviation of the rotational
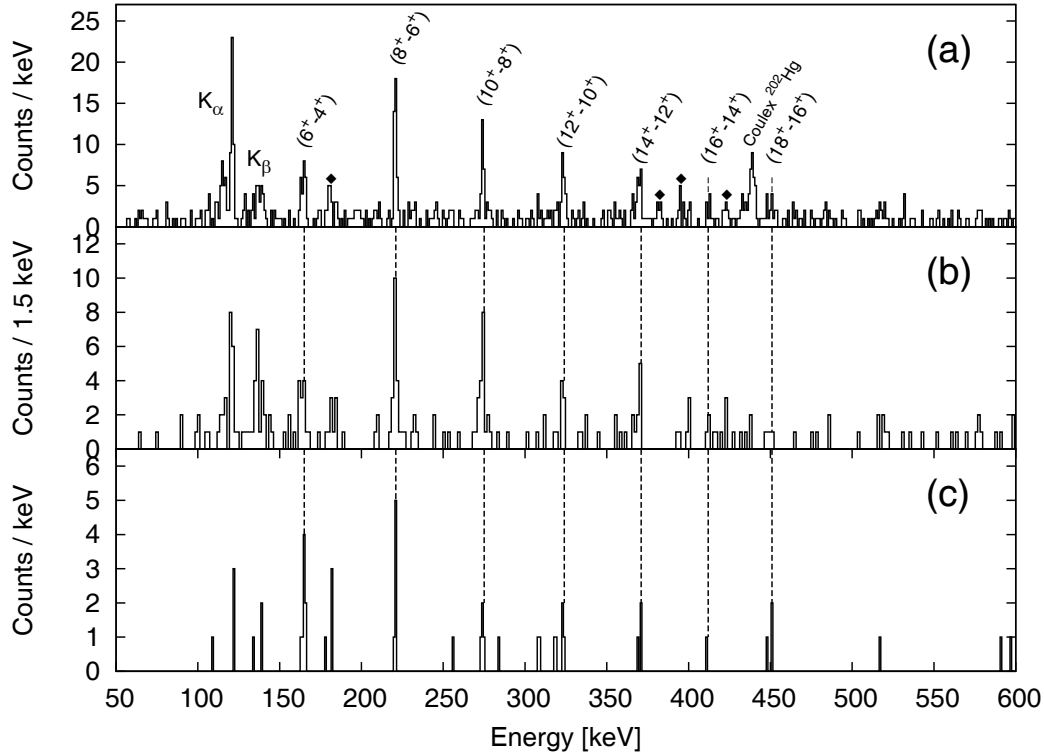
Figure 4.15: JuroGam γ-ray singles spectra of ^{248}Fm. (a) Recoil-gated γ-ray singles spectrum, (b) α-tagged γ-ray singles spectrum and (c) Sum-of-gates recoil-gated γ-ray spectrum with gates on 165 keV, 221 keV, 274 keV, 323 keV, and 369 keV. The peaks in the recoil-taged spectrum marked by diamonds could not be placed in the level scheme so far. Lines are inserted at the position of the ground-state band transitions.

Energy [keV]	Intensity		Transition
	of peak	corrected	
165.2(3)	20(5)	100(25)	$(6^+ \rightarrow 4^+)$
181.1(4)	11(4)		
221.4(2)	37(6)	86(14)	$(8^+ \rightarrow 6^+)$
274.7(3)	23(5)	42(9)	$(10^+ \rightarrow 8^+)$
324.0(3)	19(5)	32(8)	$(12^+ \rightarrow 10^+)$
370.4(3)	18(5)	30(8)	$(14^+ \rightarrow 12^+)$
383(1)	7(3)		
396(1)	8(3)		
413(1)	7(3)	12(5)	$(16^+ \rightarrow 14^+)$
423(1)	7(3)		
451(1)	6(3)	10(5)	$(18^+ \rightarrow 16^+)$

Table 4.6: Fit results of the peaks in the recoil-gated spectrum in ^{248}Fm. The intensities of the proposed ground-state band transitions in the third column are corrected for detector efficiency and conversion coefficients. Relative values are given with respect to the $6^+ \rightarrow 4^+$ transition. Proposed transition assignment in the right column.
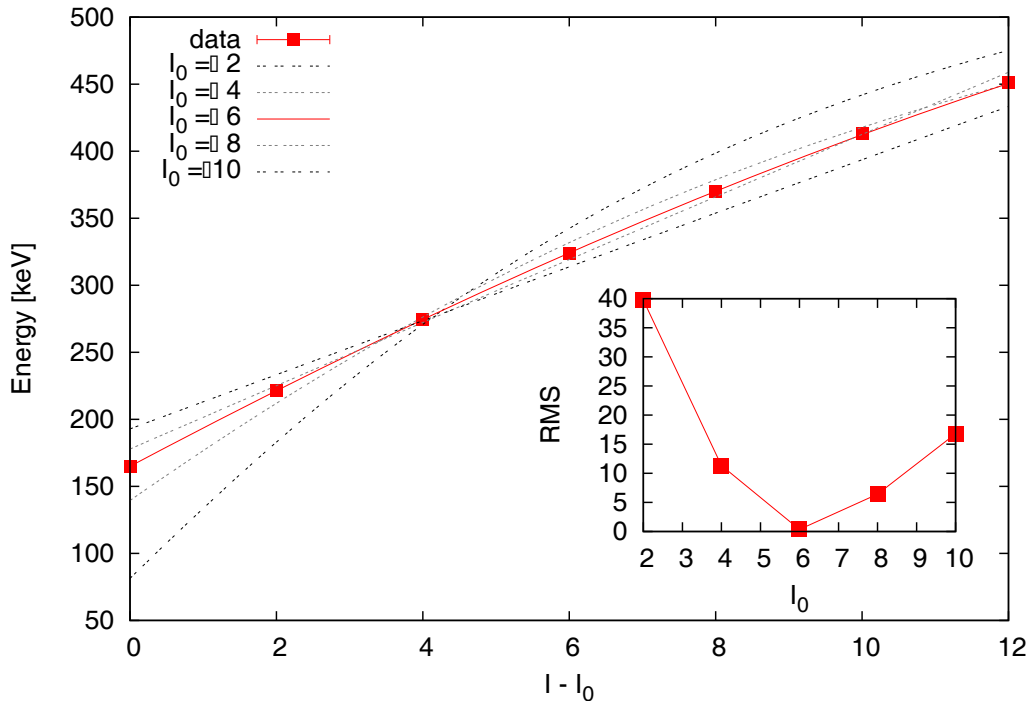
Figure 4.16: Spin fit of the ground-state band of ^{248}Fm using the method proposed by Wu *et al.* [88]. I_0 indicates the initial spin of the lowest transition in the band. Inset: Root-mean square (RMS) deviation from the data against choice of initial spin I_0 in the fit.

formula in Equation 2.27 from purely quadratic behaviour, as explained in Section 2.3.3. In the first step of the spin-fit method, the transition energies are fitted to the data for different spin assumptions:

$$E_\gamma(I \to I-2) = E(I) - E(I-2) = a\left[\sqrt{1 + bI(I+1)} - \sqrt{1 + b(I-1)(I-2)}\right]. \quad (4.3)$$

The root-mean square deviation of the fit to experimental data is then calculated and plotted for the different cases. It increases drastically away from the true value for the spin. The result of the fits is shown in Figure 4.16.

The transition seen in Figure 4.15 can thus be assigned the spins from $6^+ \to 4^+$ to $18^+ \to 16^+$, as indicated in the figure. The parity is positive, as we are investigating the ground-state band.

The optimal spin fit provides values for the lowest two transitions as well. Using the optimal spin-assumption, we get energies of 46(1) keV for the $2^+ \to 0^+$, and 106(1) keV for the $4^+ \to 2^+$ transitions.

This spin assignment is supported by the energy systematics of known ground-state bands in the region around ^{254}No. Note that for ^{250}Fm and ^{254}No the $2^+ \to 0^+$ transition energies, and for ^{248}Fm and ^{252}No as well the $4^+ \to 2^+$ and $2^+ \to 0^+$ transition energies are fitted by Harris- and Wu-type spin-fitting procedures. The energies are close to each other, within 40 keV up to spin 12. The growing divergence above spin 10 and a deeper discussion of low-spin energy differences will be given in the discussion part.

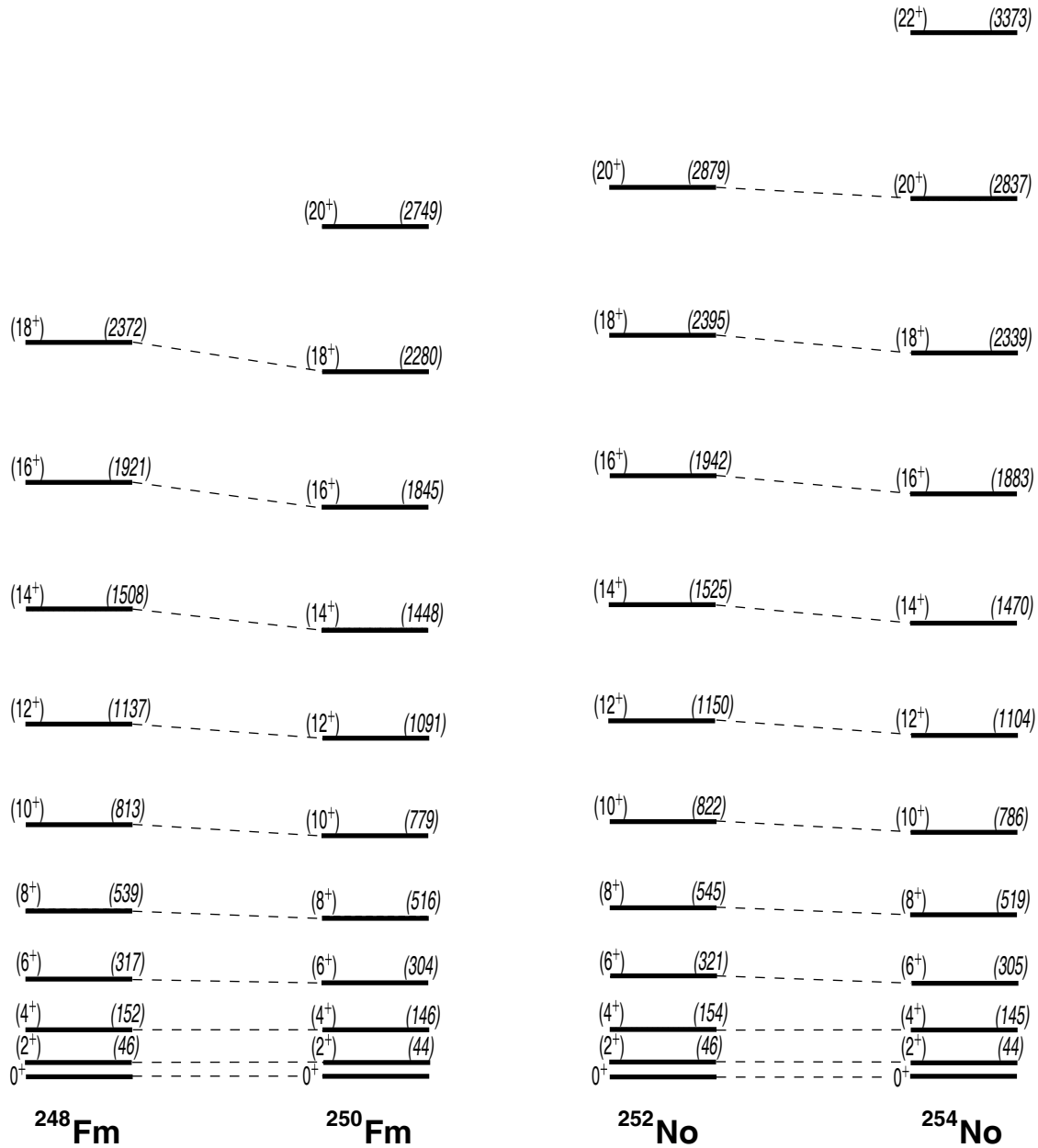Figure 4.17: Comparison of the ground-state rotational band structures of ^{248}Fm, ^{250}Fm (both this work), ^{252}No [15], and ^{254}No [90]. Note that for ^{250}Fm and ^{254}No the 2^+ energies and for ^{248}Fm and ^{252}No even the 4^+ energies are extrapolated, which introduces an uncertainty to the absolute energies.
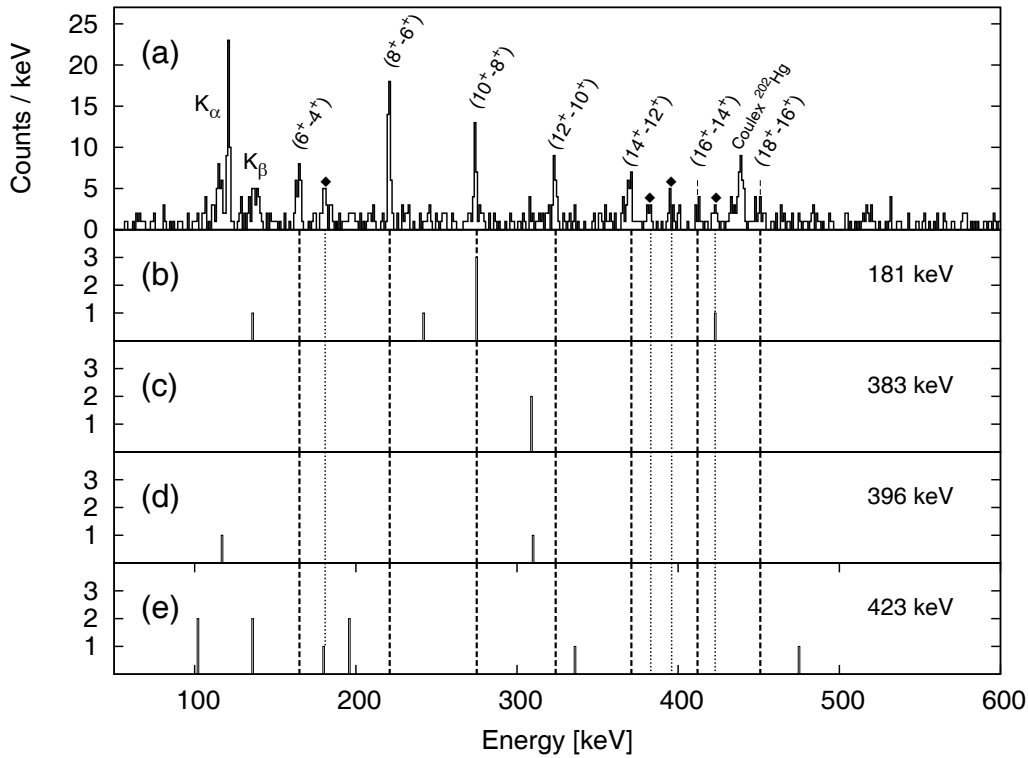
Figure 4.18: (a) Recoil-gated γ-ray singles spectrum. (b)-(e) Recoil-gated JuroGam spectra with gates set on the unidentified peaks in Figure 4.15. Dashed lines indicate ground-state band transitions, dotted lines the four unidentified transitions in the recoil-gated spectrum.

In Figure 4.18, the unassigned peaks in the recoil-gated singles spectrum are further investigated. In order to find possible links to the ground-state band, gates are set on the four peaks at 181 keV, 383 keV, 396 keV, and 423 keV; the resulting spectra are shown in Figure 4.18(b) to (e). As already seen from the sum-of-gates spectrum, only the 181 keV transition is in coincidence with the ground-state band, to the transition at 274 keV. One coincidence between 181 keV and 423 keV is found, as can be seen from Figures 4.18(b) and (e). Both spectra show as well counts at the position of the ^{248}Fm K X-rays, which confirms their assignment to ^{248}Fm. However, the level of statistics does not allow a proper analysis, and the four transitions cannot be placed into the level scheme.

4.4.3   Decay Spectroscopy

As discussed in Section 4.3.3, the isomeric decay of ^{248}Fm has been investigated using the signals of summed electrons in the DSSSD. The spectrum of the time difference between recoils and correlated electrons in the same pixel of the DSSSD is plotted in Figure 4.19(a) with logarithmic scale on the x axis. The spectrum is displayed up to $ln(t_{electron} - t_{recoil}[\mu s]) = 12$, which corresponds to approximately 165 ms, above which only random correlations are registered. In Figure 4.19, a correction is made to account for the dead time of the read-out electronics.

The spectrum contains two distinct peaks, a smaller one at short times, and a dominating one at longer times, which can be fitted by exponential curves. Exponential fits give a half
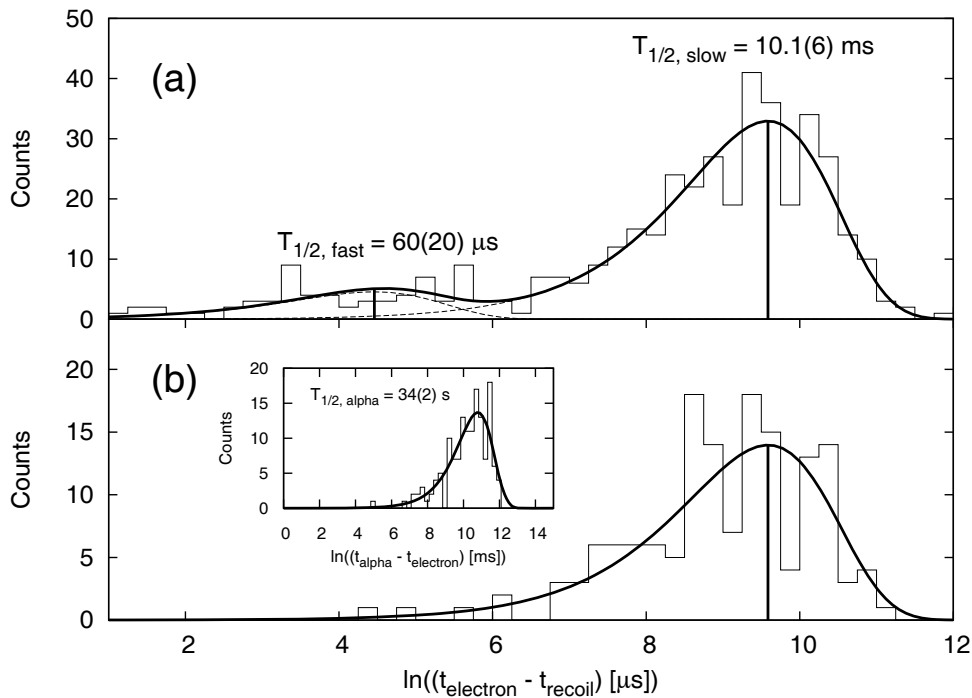
Figure 4.19: (a) Time spectra of recoils and correlated electrons detected in the same pixel of the DSSSD. (b) Same as (a), but only showing recoil-electron pairs, which are correlated to subsequent ^{248}Fm α decay. Inset of (b): Time between correlated electrons and ^{248}Fm α particles. The maximum correlation time is 1000 s.

life of the smaller peak of 60(20) μs, and of the larger one of 10.1(6) ms.

The 10.1(6) ms peak is also present in Figure 4.19(b), which shows the recoil-electron time distribution with the same condition as in Figure 4.19(a), but with the additional constraint that the recoil-electron pairs are correlated to ^{248}Fm α particles arriving within a search time of 1000 s in the same pixel. The time distribution of the α particles is given in the inset. The obtained half-life agrees with the half-life of ^{248}Fm α decay, and no background is seen within the correlation time. Therefore, the 10.1(6) ms peak can be assigned to a new isomer in ^{248}Fm.

The population of the isomer can be estimated with the aid of the electron events in the 10.1(6) ms peak of Figure 4.19(a). 420(20) events are assigned to the correlated electrons of the 10.1 ms isomer, which compares to 790(30) correlated α events. The efficiency of detection of α particles can be approximated to 55 %, and that for electrons is taken from the discussion in Section 4.3.3 as 90(5) %. This gives a population of the isomer of 32(3) %, close to the value for the $K^{\pi} = 8^{-}$ isomer in ^{250}Fm.

The energies of the recoil-correlated electrons are displayed in Figure 4.20(a), which have a recoil-electron time gate of 1 ms to 100 ms and are therefore equivalent to the electrons of the 10.1 ms isomer. The spectrum in Figure 4.20(b) shows the same electrons, but with the further condition that the recoils are followed by α particles within a search time of 1000 s. Single transitions can unfortunately not be spotted, which could be due to the diminished resolution of the DSSSD for electrons (see for example Figure 3.11 for a calibrated ^{133}Ba spectrum).

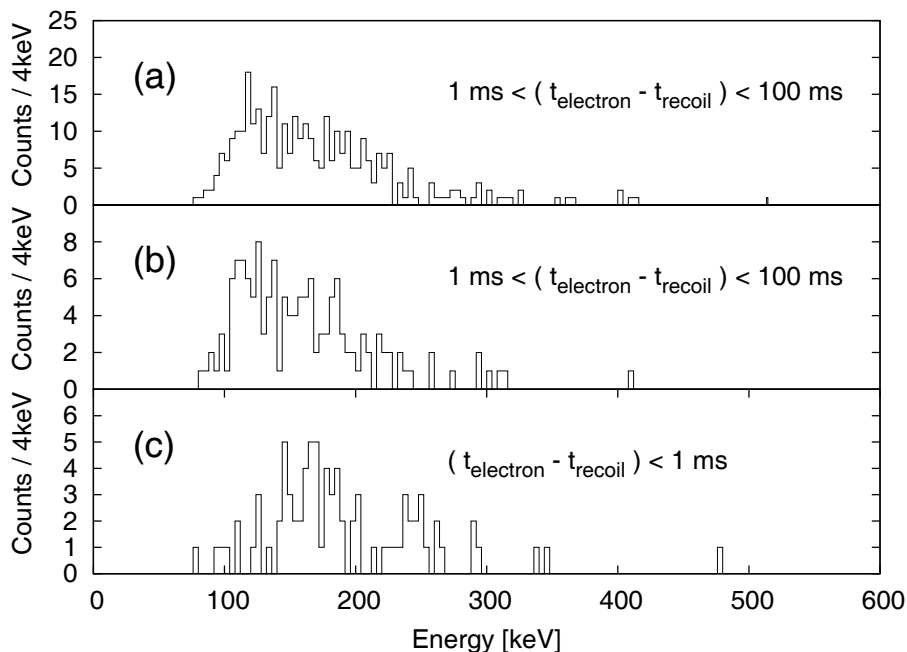Figure 4.20: Energy distribution of the recoil-correlated electrons. Electrons measured (a) between 1 ms and 100 ms after arrival of a recoil, (b) between 1 and 100 ms after arrival of a recoil, and followed by a ^{248}Fm α particle, and (c) within 1 ms after arrival of a recoil.

In order to get information on the decay path of the isomer, the γ rays which are coincident with the $T_{1/2} = 10.1(6)$ ms electrons were investigated. Due to the limited amount of statistics, it is not possible to delineate the exact decay path, but some conclusions can be drawn anyway.

The Planar germanium γ-ray spectrum does not show any distinct peaks, but in the Clover spectrum, peaks are observed at 805(1) keV and 904(1) keV (see Figure 4.21(a)). These transitions are similar to high-energy γ rays in ^{250}Fm ([35] and this work), ^{252}No [91], and ^{254}No [21]. Similar to these cases, they are proposed to decay from the isomer or an intermediate state into the ground-state band. However, the energy difference between these two transitions does not correspond to the energy of the $4^+ \rightarrow 2^+$ transition, which is deduced from the spin fit to be 106(1) keV, or to any other ground-state band transition. As the 905 keV transition is the strongest transition, it is proposed to decay directly from the isomer or from an intermediate state. If the initial state of this transition had odd spin I, it would decay into the ground-state band at spin $I - 1$ or $I + 1$. Then another transition should be seen, to $I + 1$ or $I - 1$, respectively, using similar reflections as for the interband transitions of ^{250}Fm in Section 4.3.3. As this is not seen, the initial spin of the 905 keV transition, and thus the isomer or intermediate state, probably has even spin. The γ rays in the 905 keV peak in the Clover germanium γ-ray spectrum are coincident with electrons of energy up to ≈ 170 keV. This allows a minimum value for the excitation energy of the isomer to be given which is $E_{exc} > 170 + 905 = 1075$ keV.

The 60(20) μs peak in Figure 4.19(a) vanishes, when demanding a subsequent ^{248}Fm α particle in the same pixel of the DSSSD, as done in Figure 4.19(b). It is therefore not assigned as an isomer in ^{248}Fm. Further evidence is found by searching for chains of electrons (R-e_1-e_2)
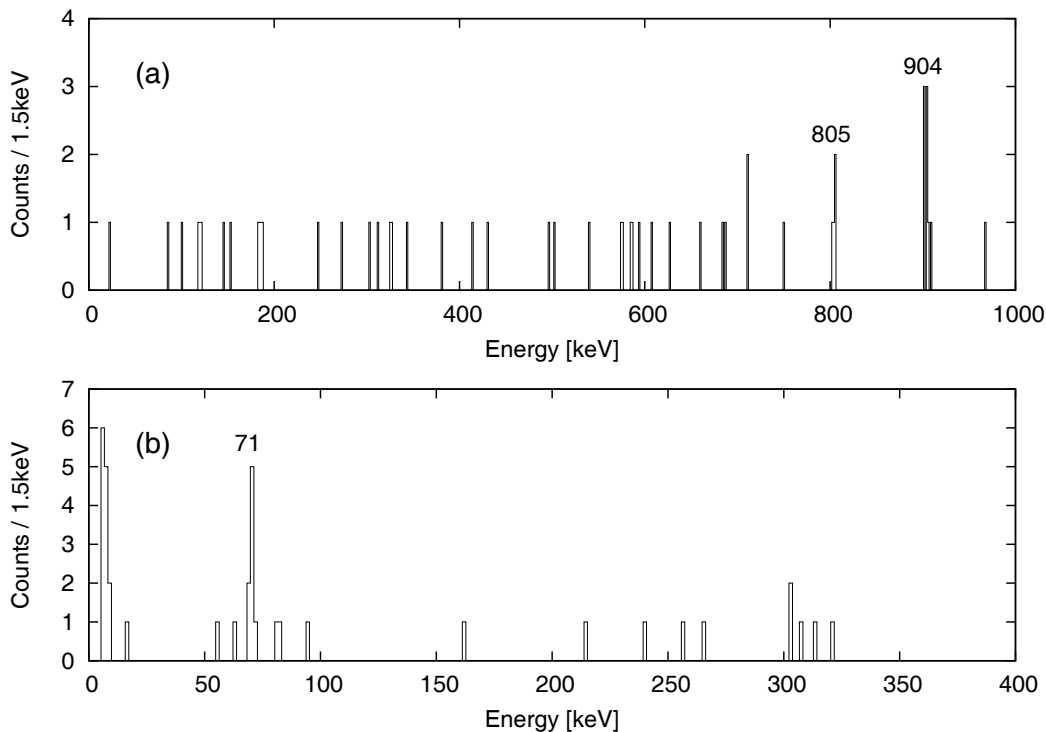
Figure 4.21: (a) Clover spectrum of γ rays in coincidence with electrons between 1 and 100 ms. (b) Planar spectrum of γ rays in coincidence with electrons up to 1 ms after arrival of the recoil.

subsequent to recoil implantation. No evidence was found for the 60(20) μs electrons to be followed by electrons from the 10.1 ms isomer, or vice versa.

In order to find a candidate for the 60(20) μs isomer, electron and γ ray spectra are investigated. The energy distribution of correlated electrons is plotted in Figure 4.20(c), which arrive within 1 ms in the same pixel of the DSSSD as the recoils. The distribution is roughly similar as that of the slow component, which supports the assignment as an isomer. It peaks at a higher energy, and is divided into two components centered around 170 keV and 240 keV.

The spectrum of γ rays in the Planar germanium detector which are coincident with the correlated electrons in Figure 4.20(c), is plotted in Figure 4.21(b). One peak is clearly visible at 71(1) keV. The equivalent Clover spectrum does not show any peaks.

As mentioned in the analysis of the ^{250}Fm isomer decay, the K_α and K_β X rays of mercury are 70.8 keV and 68.9 keV, respectively. An isomer can be found in ^{201}Hg, which has a half-life of 94 μs, and decays in a chain of 219 keV $M2$, 521 keV $E2$, and 26 keV $M1$ transitions to the ground state. Taking into account the large uncertainty of the fit in Figure 4.19, this half life is close to the measured one of 60(20) μs. The 219 keV $M2$ transition is highly converted, and cannot be seen in the γ spectrum, but can produce a strong K X-ray peak. No indication of peaks from the 219 keV transition are found in the electron spectrum, which can be due to the low resolution in the detector. The expected intensity of the 521 keV in the focal-plane Clover array can be estimated from the number of electrons. 84(9) correlated electrons are present in the spectrum in Figure 4.20(c), and taking into account the efficiency of the focal-plane

Clover array at 521 keV of 6.9 %, 6(1) counts are expected. However, electrons might pass the gate, which are not from the isomer in ^{201}Hg. Another estimate can be given using the 71 keV peak in the Planar spectrum. Taking into account the Planar efficiency of 16.8 % at 71 keV, the 8(3) γ rays in the peak correspond to 47(17) electron events in the DSSSD and 3(1) counts in the 521 keV peak of the focal-plane Clover array. As the Clover efficiencies are only simulated, and might be overestimated, the 521 keV peak is not necessarily expected to be seen.

Chapter 5

Discussion

In the following chapter, the results from the in-beam and delayed spectroscopy will be discussed and compared to neighbouring nuclei. In the first section, the ground-state band and the $K = 8$ band in ^{250}Fm will be discussed in terms of the moment of inertia. The deformation of ^{248}Fm is deduced from the ground-state band energies in Section 5.2. The moments of inertia are used in Section 5.3 to calculate the energies of the first 2_1^+ energies with help of Harris fits, and the resulting energies are compared to neighbouring isotopes and isotones in the region of ^{248,250}Fm. The following three sections elaborate on the K isomers in ^{248}Fm and ^{250}Fm. The isomer in ^{250}Fm is assigned in Section 5.4, and a tentative assignment for the isomer of ^{248}Fm is made in Section 5.5. Finally, the systematics of two-quasiparticle states of K isomers in this region are investigated in terms of energy and hindrance in Section 5.6.

5.1 Moment of Inertia

In our experiments, transitions in the ground-state bands of ^{248}Fm and ^{250}Fm are seen from 4^+ to 18^+ and from 2^+ to 20^+, respectively. The spin of the transitions in the ^{248}Fm band are verified by the spin-fitting method introduced by Wu *et al.*, and by comparison to bands of neighbouring nuclei. Knowing the transition energies and spins, the kinematic and dynamic moments of inertia $\mathscr{I}^{(1)}$ and $\mathscr{I}^{(2)}$ of these bands can be calculated with Equations 2.36 and 2.37.

The moments of inertia of ^{248}Fm and ^{250}Fm are plotted in Figure 5.1 against the rotational frequency ω. In the same figure, the moments of inertia of ^{252}No, ^{254}No, and ^{246}Fm are given for comparison. They are calculated from transition energies and spins published in [15], [90], and [27] for ^{252}No, ^{254}No, and ^{246}Fm, respectively, which are all based on γ-ray spectroscopy. The energy of the $4^+ \rightarrow 2^+$ transition in ^{254}No is an exception, it is only available from electron-spectroscopy data published by Humphreys *et al.* [92]. They measured a γ-transition energy of 101.1(6) keV, within errors identical to 102(1) keV, which Reiter *et al.* deduced with the help of a Harris fit [14]. However, comparison of the ground-state band transitions between 10^+ and 4^+ as measured by conversion-electron spectroscopy by Humphreys *et al.* to a γ-ray measurement by Eeckhaudt *et al.* shows an average offset of 0.8(8) keV [90]. The difference could be caused by an offset in the calibration, or by the somewhat worse energy resolution in electron spectroscopy. The offset could explain why the lowest data point for ^{254}No does not follow the curve in a smooth way for both $\mathscr{I}^{(1)}$ and $\mathscr{I}^{(2)}$, even when taking into account the error bars.
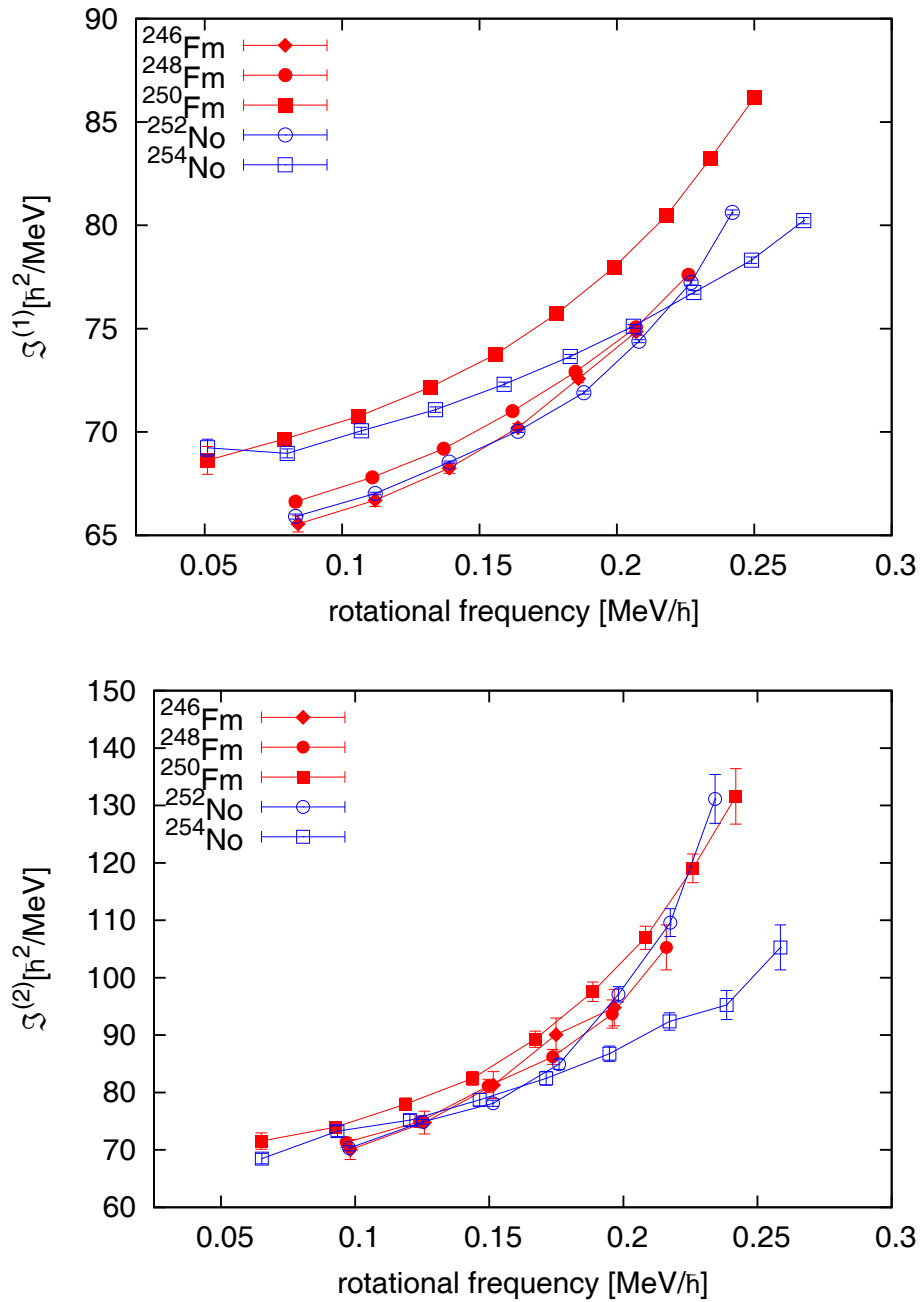
Figure 5.1: Kinematic and dynamic moment of inertia of rotational bands in even-even nuclei in the vicinity of ^{248,250}Fm, calculated from measurements reported in this work (^{248,250}Fm), in [27] (^{246}Fm), in [15] (^{252}No), and in [90] (^{254}No).
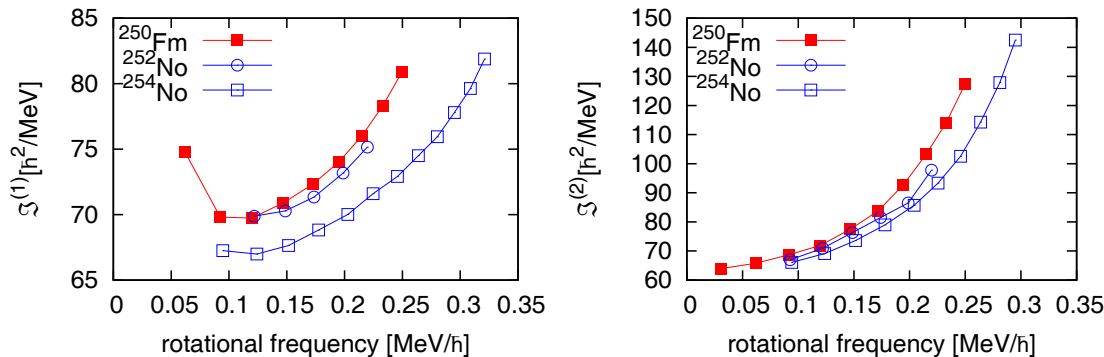
Figure 5.2: Self-consistent mean-field calculations of the moment of inertia of ^{250}Fm and ^{252,242}No using the Skyrme SLy4 interaction. Values adopted from Bender *et al.* [94].

The kinematic moments of inertia $\mathscr{I}^{(1)}$ can be sorted into two groups for low ω. ^{248}Fm and ^{252}No on the one hand and ^{250}Fm and ^{254}No on the other hand have very similar moments of inertia. The low-frequency part of the ^{246}Fm curve is close to the former group, but has a high uncertainty. For higher frequency, the slopes of ^{248}Fm, ^{250}Fm, and ^{252}No, are comparable, with ^{252}No bending up a little faster at ≈ 0.2 MeV/$\hbar$. All three show an upbend at ≈ 0.15 MeV/$\hbar$ when compared to ^{254}No.

The dynamic moments of inertia $\mathscr{I}^{(2)}$ confirm this trend. The curves of ^{248}Fm, ^{250}Fm, ^{252}No, and ^{254}No have approximately the same starting point at low frequencies. The differences visible in $\mathscr{I}^{(1)}$ are not as distinct here. At ≈ 0.15 MeV/$\hbar$, the same upturn of ^{248}Fm, ^{250}Fm, and ^{252}No as compared to ^{254}No is seen, with ^{252}No rising even more steeply at somewhat higher ω.

Duguet *et al.* investigated rotational properties of nobelium isotopes using the Hartree-Fock Bogoliubov (HFB) theory with Skyrme forces [93]. Quasi- and single-particle Routhians are calculated for ^{254}No, in which the $9/2^-[734]_\nu$ neutron and above $\hbar\omega \geq 0.2$ MeV the $7/2^+[633]_\pi$ proton orbitals are lowest in energy. These orbitals stem from the high-spin neutron $j_{15/2}$ and proton $i_{13/2}$ intruders, respectively. They are both hole states, and are therefore candidates for alignment in the lighter isotones and isotopes of ^{254}No. Dynamic moments of inertia $\mathscr{I}^{(2)}$ were calculated for ^{252}No and ^{254}No and agree rather well with experiment. Even the upslope of ^{252}No at $\hbar\omega \approx 0.2$ MeV is reproduced, but much weaker than in experiment. An explanation for the upslope is not given.

Bender *et al.* explain the upslope by an overestimation in energy of the $j_{15/2}$ level, which is responsible for the alignment [94]. As a consequence, the $9/2^-[734]_\nu$ level, which is situated between N=150 and N=152 in the single-particle spectrum, is lowered. This leads to a faster alignment of ^{252}No with respect to ^{254}No. The results of his calculation are given in Figure 5.2.

Another calculation on the rotational properties of ^{254}No was performed by Laftchiev *et al.* [95]. Similar to Duguet *et al.*, they used the HFB method with Skyrme interaction. Single-particle Routhians are calculated, in which the $9/2^-[734]_\nu$ neutron level lies below $7/2^+[624]_\nu$, and is thus lower than in the spectrum of Duguet *et al.*, in accordance to the suggestion made by Bender *et al.* The moments of inertia of ^{254}No are very well reproduced, which gives confidence in their calculations.

Unfortunately, no calculation has been performed for ^{248}Fm so far. To draw more definite conclusions, data up to higher spin is needed, if possible to see the maximum of the alignment
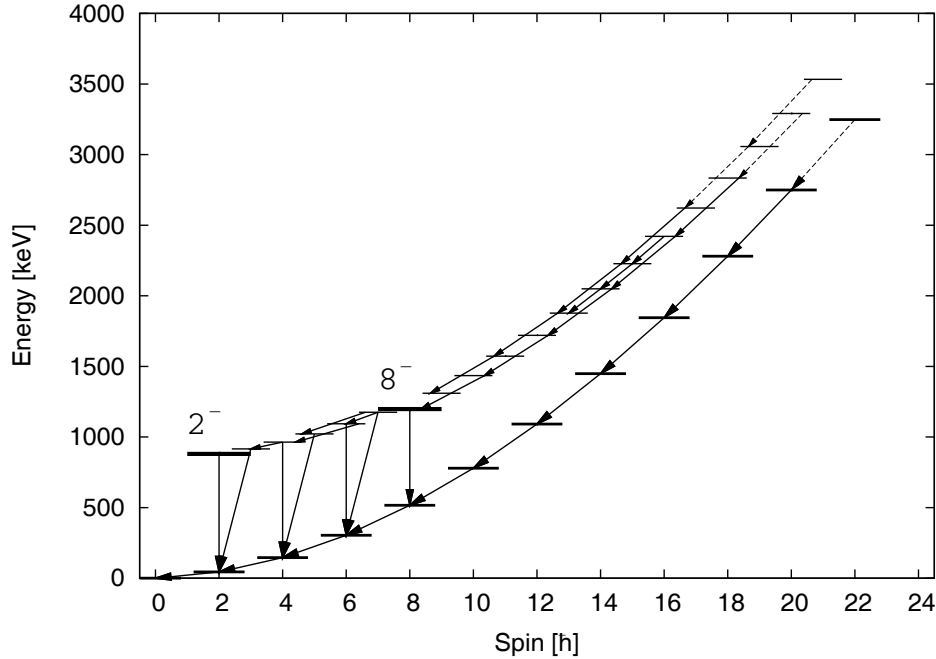
Figure 5.3: Excitation energy against spin of the states observed in ^{250}Fm. The plot includes the observed transition in the ground-state band, octupole 2^- band, and $K = 8$ band, and interband transitions.

in the $\mathscr{I}^{(2)}$ plot. More information could be drawn, if more systematic data on isotones and isotopes would be available, possibly of ^{252}Fm and ^{250}No. On the other hand, theoretical calculations are needed which cover all known fermium (and nobelium) isotopes.

Moment of Inertia of the $K^\pi = 8^-$ Band

The decay path of the isomer in ^{250}Fm can be followed in the energy-spin plot in Figure 5.3, which contains the ground-state, 2^- octupole and $K = 8$ bands. The ground-state band is yrast all the way up to spin $I = 22$, but the energy difference decreases for higher excitation energies due to the smaller slope of the isomeric band. The smaller slope is caused by the blocking effect of the two-quasiparticle excitation, which inhibits pairing of the two correlated states. The nucleus is thus more "rigid", the band has a higher moment of inertia, and the energy differences between band members are smaller. If the $K = 8$ band is populated, the decay follows the rotational band, where 80 percent of the decay of the band head goes via the intermediate band to the ground-state band. Decay to the intermediate band is highly unfavoured in energy, but because of its K value (2) the hindrance is reduced by four orders of magnitude as compared to decay into the ground-state band, as seen from Equation 2.56. The $K = 2$ band is non-yrast and relatively high up in energy. It is excited as well in the fusion-evaporation reaction, probably populated from higher-lying non-yrast bands, with strong feeding into the lower-spin part of the band.

The moments of inertia $\mathscr{I}^{(1)}$ and $\mathscr{I}^{(2)}$ are shown in comparison to the ground-state band in Figure 5.4. The low-frequency values of $\mathscr{I}^{(1)}$ and $\mathscr{I}^{(2)}$ are around 10 units of $\hbar$ higher than for the ground-state band at $\omega \approx 0.12$ MeV/$\hbar$, a consequence of the blocking effect
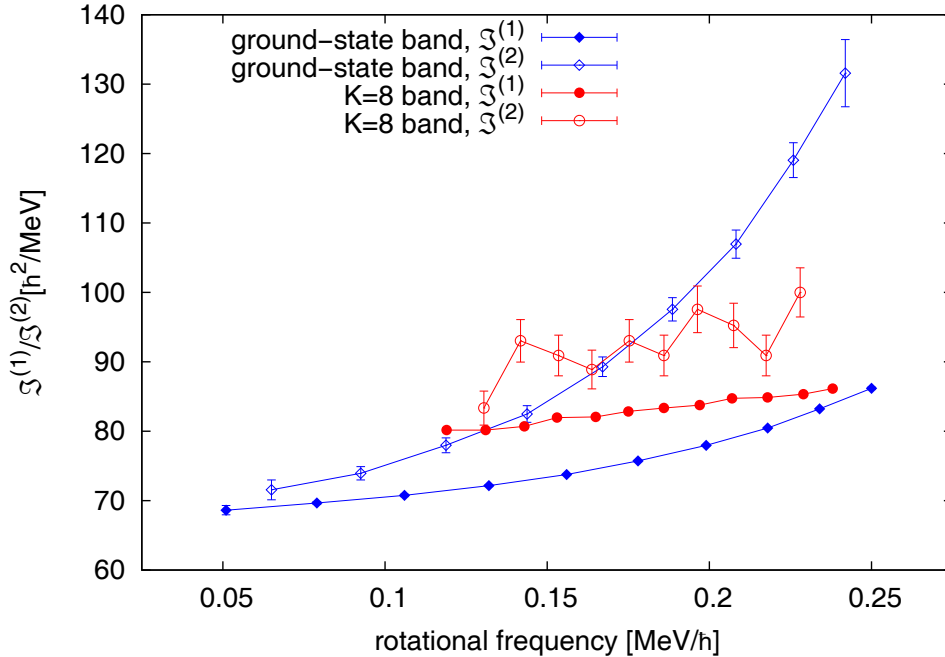
Figure 5.4: Moment of inertia of the $K = 8$ band (red curves) compared to the ground-state band (blue curves) in ^{250}Fm. The $\mathscr{I}^{(1)}$ values are given with closed symbols, the $\mathscr{I}^{(2)}$ values with open symbols.

discussed above. At higher frequencies, the slope is smaller, and the curves for $\mathscr{I}^{(1)}$ approach and even cross each other for $\mathscr{I}^{(2)}$. The slope for the $K^\pi = 8^-$ band is comparable to the low-spin part of the ground-state band, up to $\omega \approx 0.10 - 0.12$ MeV$/\hbar$. This could be due to blocking effects as well, as the isomer is suggested to be built of neutrons in the $9/2^-[734]$ and $7/2^+[624]$ Nilsson orbits (see next section). The $9/2^-[734]$ neutron stems from the $j_{15/2}$ spherical shell, and is thought to be responsible for the alignment in ^{250}Fm, as explained above. As this neutron cannot take part in the alignment any more, a smaller upbend than in the ground-state band is expected.

5.2 Ground-State Deformation in ^{248}Fm

The 2^+ energy, which is calculated from the spin fit of the ground-state band, can be used to give an experimental value for the deformation of ^{248}Fm. For this purpose, relations are used between the lowest 2^+ state in the nuclear spectrum and its decay lifetime. These relations are found in fits of data of a broad range of nuclei, have therefore a large uncertainty and should be taken as a rough estimate.

Grodzins performed a fit of 2^+_1 lifetimes to energy in nuclei between ^{16}O and ^{234}U, excluding closed shell cases. It was found that the 2^+ lifetimes are inversely proportional to $E^4_{2^+_1}$, which can also be derived from the hydrodynamical model by Bohr and Mottelson [96]. Furthermore, the lifetimes are proportional to Z^{-2} and $A^{1/3}$, where Z is the element number

	τ_γ[ns]	Q_0[eb]	β_2
Grodzins	152	11.46	0.26(3)
Raman *et al.*	125	12.61	0.28(3)
Herzberg *et al.*	124	12.66	0.28(3)
Local Fit	125	12.63	0.28(2)

Table 5.1: Experimental lifetime, electrical quadrupole moment Q_0, and deformation β_2 of ^{248}Fm calculated with the approaches from Equations 5.1, 5.2, 5.3, and 5.4.

and A the atomic mass number:

$$\tau_\gamma = (2.74 \pm 0.91) \cdot 10^{14} E_{2_1^+}^{-4} Z^{-2} A^{1/3} \, . \tag{5.1}$$

The constant in front of the expression is derived from a later fit by Raman *et al.* [97].

Raman *et al.* developed this formula further by allowing the exponents of E_{2^+} and A to vary in their so-called "Best Fit" [97]:

$$\tau_\gamma = (1.25 \pm 0.50) \cdot 10^{14} E_{2_1^+}^{-4.00 \pm 0.03} Z^{-2} A^{0.69 \pm 0.05} \, . \tag{5.2}$$

The fit of Equations 5.1 and 5.2 was performed based on data of 458 nuclei published in [98] in 1987. Herzberg *et al.* performed a new fit similar to the one by Raman *et al.*, but on the improved data available in 2002 [15]:

$$\tau_\gamma = (2.9 \pm 1.50) \cdot 10^{12} E_{2_1^+}^{-3.807 \pm 0.023} Z^{-2} A^{1.237 \pm 0.065} \, . \tag{5.3}$$

In addition, Herzberg *et al.* performed a new fit, in which only nuclei in the heavy element region were used. The fitted data were limited to nuclei with $A > 200$ and $E_{2_1^+} < 150$ keV:

$$ln\left(\tau_\gamma Z^2\right) = (65.15 \pm 4.22) - (4.017 \pm 0.111)ln(E_{2_1^+}) - (5.23 \pm 0.70)ln(A) \, . \tag{5.4}$$

The uncertainties of these approaches are discussed in [15]. The fit results of the lifetimes by the three first approaches have been compared to the experimental values of 247 2^+ states in even-even nuclei with mass $A > 56$. The lifetimes were found to agree within 30 %, giving an uncertainty for the quadrupole deformation of approximately 15 %. Equation 5.4 gives somewhat better results due to the local approach. Comparing data and the fit of 23 nuclei with mass $A > 200$ and 2^+ energy below 150 keV, Herzberg *et al.* found that the lifetimes agree within 14 % and the deformation β_2 therefore has an uncertainty of 7 %.

The ground-state band transitions have $E2$ multipolarity. From the theory of electromagnetic decay, one finds a relation between the lifetime and reduced transition probability (see Equation 2.15):

$$1/\tau_\gamma = T_{fi}^{E2} = 1.225 \cdot 10^9 \cdot E_{2_1^+}^5 [MeV] \cdot B(E2)[e^2 fm^4]s^{-1} \, . \tag{5.5}$$

Here, the reduced transition probability has to be given in $e^2 fm^4$, and the energy in MeV. $B(E2)$ is related to the quadrupole moment, as can be seen from Equation 2.44. The latter is in turn related to the deformation by Equation 2.43, where $R_0 \approx 1.2$ fm.

The results of the analysis are given in Table 5.1. All four values for the deformation are within error bars of each other and agree well. The deformation can be compared to experimentally deduced deformations of neighbouring nuclei. Deformations have been calculated

for ^{250}Fm to be 0.28(2), ^{252}No to be 0.28(2), and ^{254}No to be 0.29(2) by use of the same method as above [13, 15]. The deformation of ^{248}Fm fits well with the systematics. This is evidence for the stable deformation of nuclei in the region of ^{254}No.

Theoretical calculations have been made by Cwiok *et al.* using a Nilsson-Strutinsky approach [99]. They predict the quadrupole deformation at $\beta_2 = 0.246$, and small octupole and hexadecapole deformations $\beta_4 = 0.048$, and $\beta_6 = -0.045$. The quadrupole deformation is slightly smaller than the experimental one. This seems to be a trend for the whole region, as deformation parameters are predicted to be ($\beta_2 = 0.247$, $\beta_4 = 0.035$, $\beta_6 = -0.049$), (0.249, 0.025, -0.51) and (0.252, 0.014, -0.053) for ^{250}Fm, ^{252}No, and ^{254}No, respectively.

5.3 Systematics of 2_1^+ Energies

The low-frequency behaviour of $\mathscr{I}^{(1)}$ can be studied in terms of the energies of the first 2^+ states E_{2^+}. Both are directly related to each other through Equations 2.36.

The 2_1^+ energies of ^{246}Fm, ^{248}Fm, ^{250}Fm, ^{252}No, and ^{254}No are extracted by Harris Fits of the moment of inertia curves. Fits for $\mathscr{I}^{(1)}$ and $\mathscr{I}^{(2)}$ are obtained with the Harris parametrisation [14]:

$$\mathscr{I}^{(1)} = J_0 + J_1\omega^2 , \tag{5.6}$$
$$\mathscr{I}^{(2)} = J_0 + 3J_1\omega^2 . \tag{5.7}$$

The fit gives the parameters J_0 and J_1. These are inserted into Equation 5.6, and after $\mathscr{I}^{(1)}$ and ω are replaced by E_{2^+} using Equations 2.36 and 2.38, the equation can be solved for E_{2^+}. An approximation is given by $J_0 \approx \frac{3\hbar^2}{E_{2_1^+}}$, when neglecting ω^2 in Equation 5.6.

Fits have been performed on $\mathscr{I}^{(1)}$, because it has a smoother behaviour than $\mathscr{I}^{(2)}$. As an example, the fit is shown for the ground-state band of ^{250}Fm in Figure 5.5. Clearly seen is the upbend above $\omega^2 = 0.03$ MeV^2/$\hbar^2$, corresponding to spin $I = 12$, which has been discussed above. The fit is restricted to data below this rotational frequency for all five nuclei, as it deviates from the regular behaviour assumed for the Harris parametrisation. The curve through the dynamic moment of inertia $\mathscr{I}^{(2)}$ agree well with the data and demonstrates the quality of the fit.

The 2_1^+ energies are plotted for four different isotopic chains in Figure 5.6(a). The E_{2^+} systematics of californium and curium have dips at $N = 152$. For fermium, data is missing at this position, as there is no accurate measurement of the 2^+ energy for ^{252}Fm. However, the energies of $^{246-250}$Fm and ^{254,256}Fm confine the minimum to be either at $N = 150$ or $N = 152$. The two isotopes of nobelium support the observation of a dip in the 2^+ energies at $N = 152$, as the energy of ^{252}No is smaller than of ^{254}No. Data for ^{256}No would be needed to confirm the minimum in nobelium isotopes.

Ishii *et al.* relate the dip in 2_1^+ energies to the deformed shell gap at $N = 152$ [31], which is discussed in the introduction in Chapter 1, and observed for example in spontaneous-fission decay half-life systematics [106]. The lowering is caused by weakened pairing correlations at the gap, as was first proposed by Sobiczewski *et al.* [107]. The gap parameter Δ is dependent on the matrix element $< j_1^2, 0^+ | V_{pair} | j_2^2, 0^+ >$. The higher the overlap of initial and final state, the larger the matrix elements. At the deformed shell gap, the nuclear levels are further apart. Therefore, the overlap of non-diagonal matrix elements is smaller, and consequently
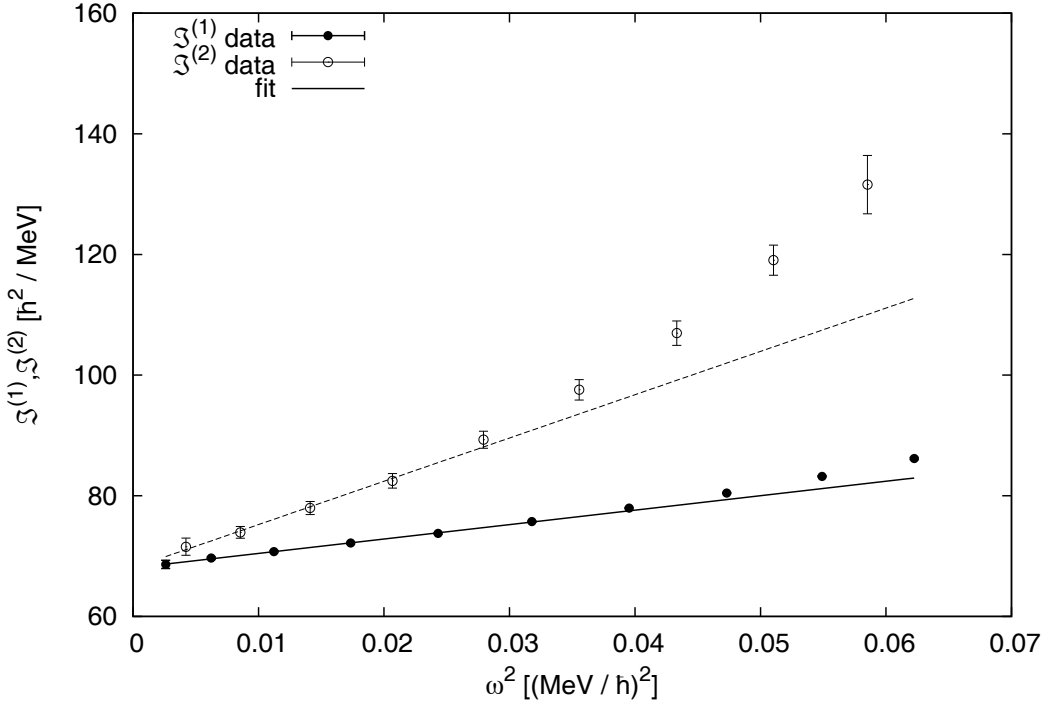
Figure 5.5: Harris fit of the kinematic moment of inertia $\mathscr{I}^{(1)}$ of the ground-state band of ^{250}Fm, using the equations given in the text, and data from this work. The experimental data for $\mathscr{I}^{(1)}$ is given by filled circles, the data of $\mathscr{I}^{(2)}$ by open circles, the fit result as continuous ($\mathscr{I}^{(1)}$) and dashed ($\mathscr{I}^{(2)}$) line.

Δ is weakened. This in turn increases the moment of inertia in Equation 2.31 by decreasing the denominator and increasing the numerator, and the 2_1^+ energies are lowered.

Below $N = 152$, the 2_1^+ energies of californium and curium continue to decrease with smaller slope than before. The same trend is found in plutonium and uranium isotones. However, the fermium isotopes break this trend. A large increase is observed from ^{250}Fm to ^{248}Fm in Figure 5.6(a). The trend is continued almost linearly for ^{246}Fm, and followed by the nobelium isotopes. Note as well that the 2^+ energy of ^{252}No is larger than the one of ^{250}Fm, indicating that the trend could be stronger for nobelium isotopes.

In order to study the Z dependence of the 2_1^+ energies, the isotonic chains for $N = 146, 148, 150, 152$ and 154 are sketched in Figure 5.6(b). The only complete set of data from plutonium to nobelium is available for $N = 150$, including ^{250}Fm from this study. This chain has a clear minimum at $Z = 98$. The same minimum is observed in the $N = 152$ data, but data is missing for $Z = 100$, or ^{252}Fm. In the $N = 154$ isotones, a dip in the systematics is evident at $Z = 98$, but the energies further decrease, so that a minimum is situated at $Z \geq 100$.

Calculations of 2_1^+ energies have been performed by Sobiczewski *et al.* [107]. The calculations are based on the macroscopic-microscopic model, using the Yukawa-plus-exponential model for the macroscopic part, and a Woods-Saxon potential for the Strutinsky shell correction. Variations in the shell structure are associated with quadrupole and higher-order deformations, which strongly influence the shell structure and play a crucial role in the for-
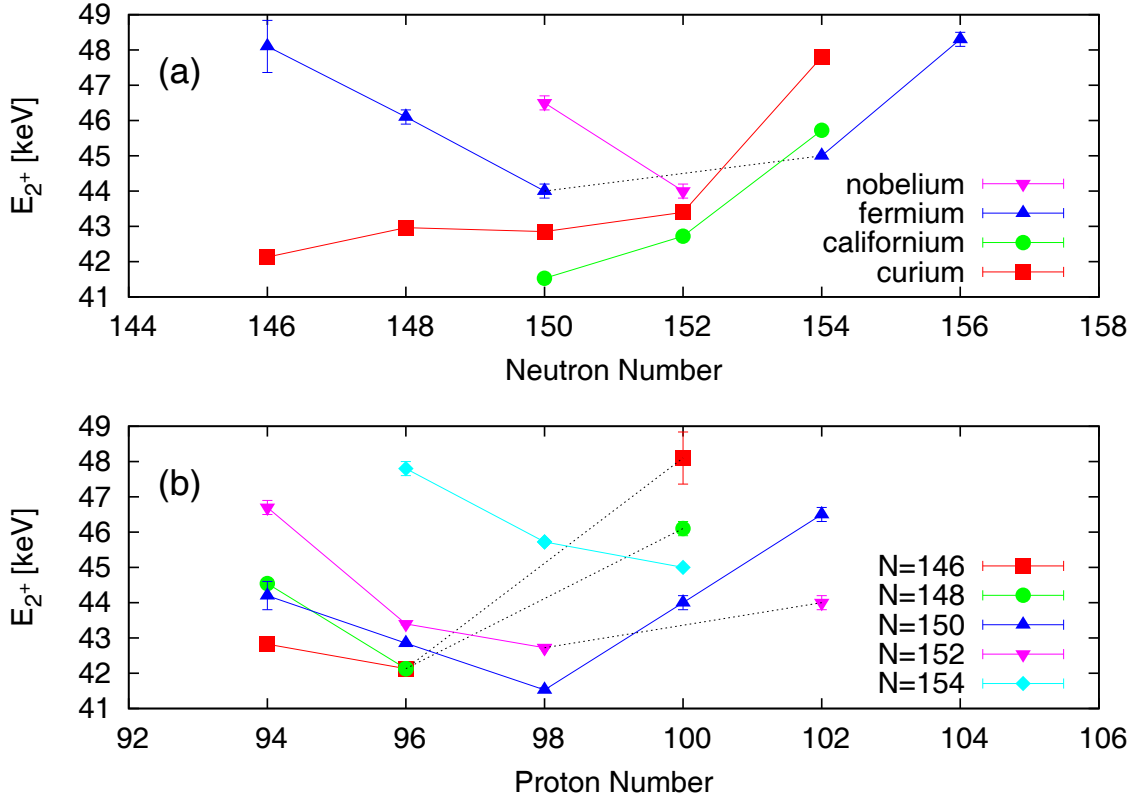
Figure 5.6: (a) Systematics of measured $E_{2_1^+}$ energies in isotopic chains of curium, californium, fermium, and nobelium. (b) Same as (a), but for isotonic chains of even-even nuclei from $N = 146$ to 154. The energies of ^{246}Fm, ^{248}Fm, ^{250}Fm, ^{252}No, and ^{254}No have been extracted by Harris fit in this work, using data from [15, 27, 90]. The remaining data is taken from [31, 100–105].

mation of a shell gap at $N = 152$.

The results of the calculations are presented in Figure 5.7. The isotopic chains in (a) drop at $N = 152$ for nobelium and fermium, as in the experimental data. The minimum is smaller for the lighter elements, and vanishes for curium. This is associated with a smaller shell gap at $Z = 100$ seen in the calculated single-particle level scheme of ^{254}No in [107]. The $Z = 100$ gap is present in the isotonic chains of the 2^+ energies shown in Figure 5.7(b), though less pronounced. There is no minimum at $Z = 98$, which is in disagreement with the experimental data, in which a clear minimum is seen at $Z = 98$ for the $N = 150$ chain.

In order to determine if the 2^+ energies correlate to the shell structure, the two-neutron and two-proton separation energies S_{2n} and S_{2p} are investigated. They are defined in the following way:

$$S_{2n}(Z, N) = B(Z, N) - B(Z, N - 2), \qquad (5.8)$$

$$S_{2p}(Z, N) = B(Z, N) - B(Z - 2, N). \qquad (5.9)$$

Here, $B(Z, N)$ stands for the binding energy of a nucleus with Z protons and N neutrons. Large energy gaps in the single-particle spectrum are seen as drops in the isotopic or isotonic
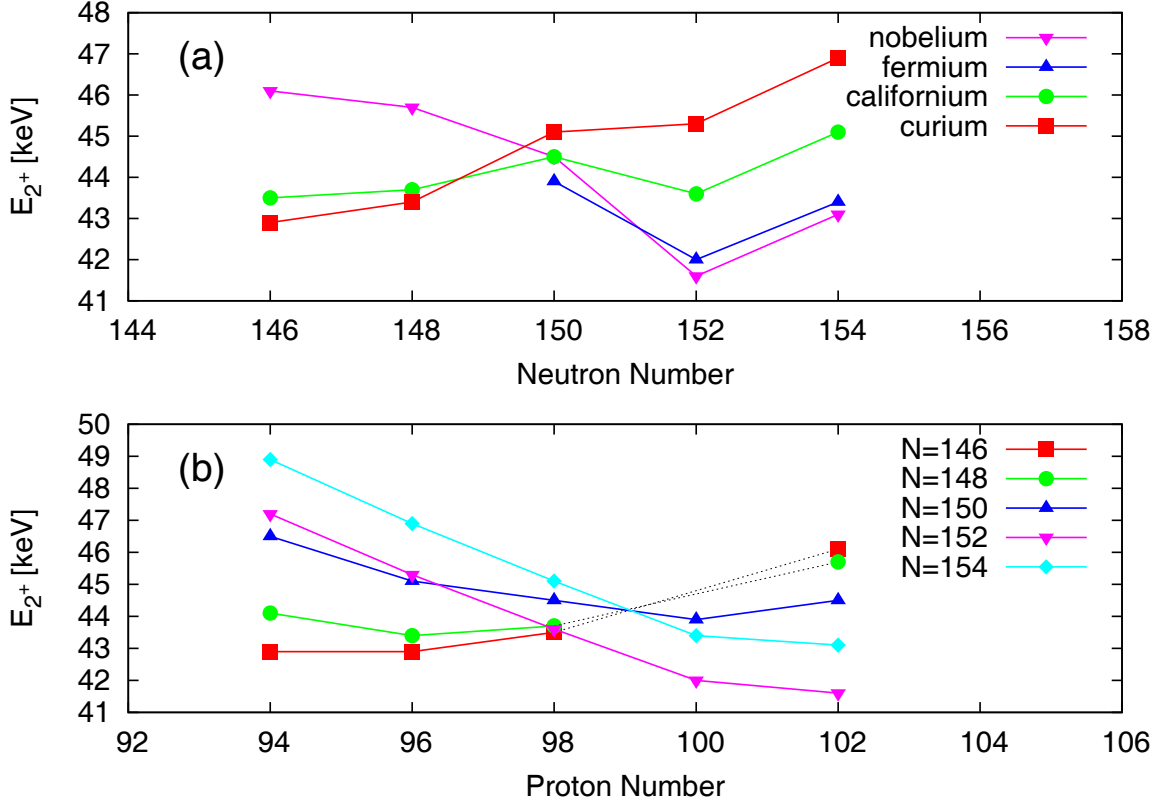
Figure 5.7: Systematics of calculated $E_{2_1^+}$ energies of (a) isotopic and (b) isotonic chains in the vicinity of ^{248,250}Fm. The calculations were performed by Sobiczewski, Muntian, and Patyk using the macroscopic-microscopic approach with a Woods-Saxon single-particle potential [107]. No energies were calculated for ^{248}Fm and ^{246}Fm, which is indicated by dashed lines in (b).

systematics of S_{2n} or S_{2p}. If energy gaps are small, δ_{2n} and δ_{2p} are more sensitive, which are related to the derivative of the separation energies and defined as:

$$\delta_{2n}(Z,N) = S_{2n}(Z,N) - S_{2n}(Z,N+2), \tag{5.10}$$
$$\delta_{2p}(Z,N) = S_{2n}(Z,N) - S_{2n}(Z+2,N). \tag{5.11}$$

The two-neutron separation energies and δ_{2n} values of isotopic chains of even-even nuclei between curium and nobelium are shown in Figure 5.8. A clear drop is seen at $N = 152$ in the chains of fermium and nobelium, which is not longer visible for curium and californium. The $N = 152$ shell gap appears in the δ_{2n} chains in the lower panel of the figure as a clear peak for fermium and nobelium. Even the curium and californium δ_{2n} values have a small peak at this position, showing the sensitivity of δ_{2n} compared to S_{2n}. These observations agree with the results from experimental and calculated 2^+ energies in Figures 5.6(b) and 5.7(b), where the minima are more pronounced for fermium and nobelium.

The two-proton separation energies for isotonic chains of even-even nuclei between $N = 146$ and $N = 154$ give less pronounced drops (see Figure 5.9(a)), which indicates less pronounced shell structure. A clear drop is seen only at $Z = 100$ for the $N = 152$ chain. The

Figure 5.8: Two-neutron separation energies S_{2n} (a) and δ_{2n} (b) in isotopic chains from curium to nobelium. The data for S_{2n} is taken from the 2003 atomic mass evaluation [108], and δ_{2n} is calculated from the separation energies using Equation 5.10.

Figure 5.9: Two-proton separation energies S_{2p} (a) and δ_{2p} (b) in isotopic chains from curium to nobelium. The data for S_{2n} is taken from the 2003 atomic mass evaluation [108], and δ_{2p} is calculated from the separation energies using Equation 5.11.

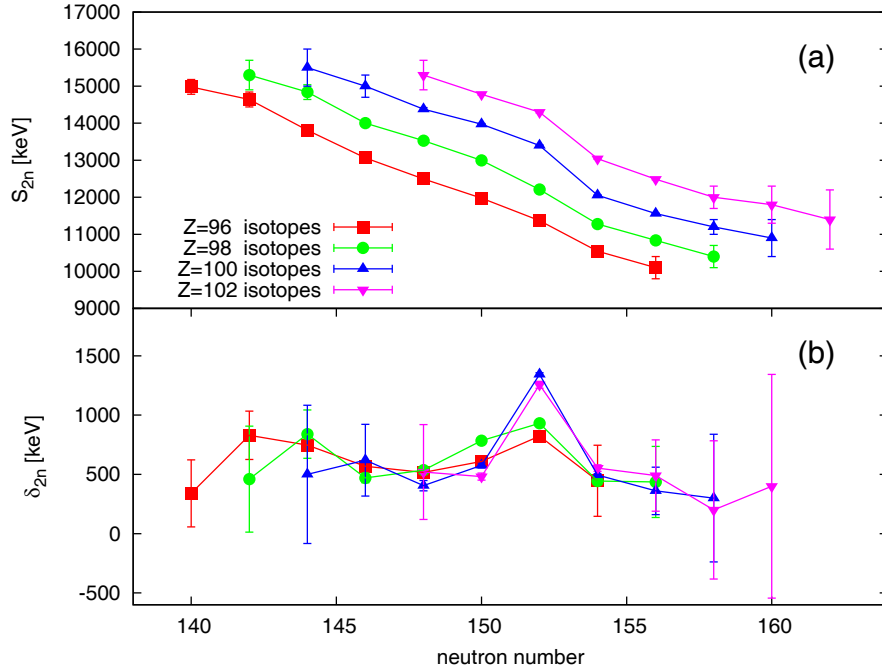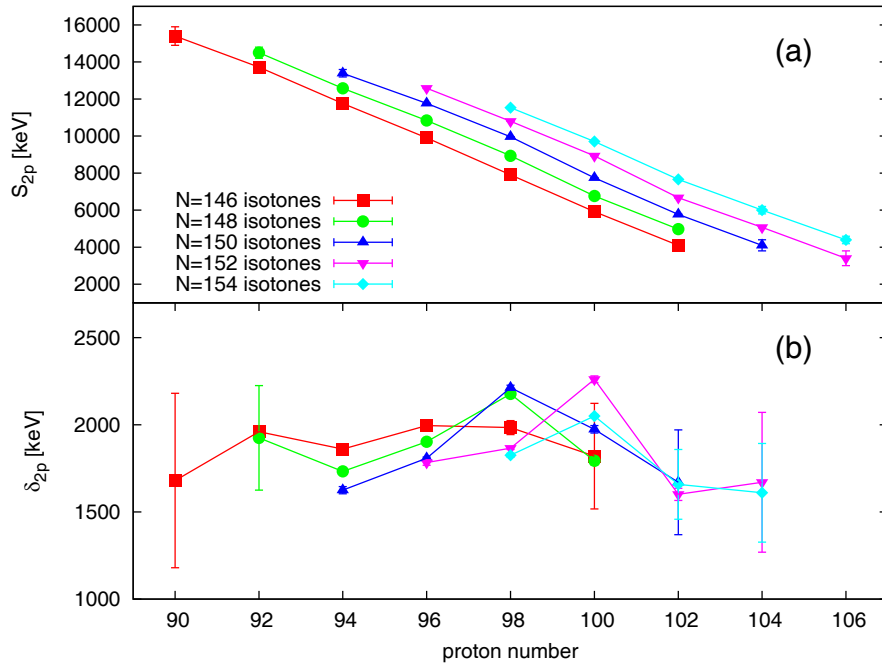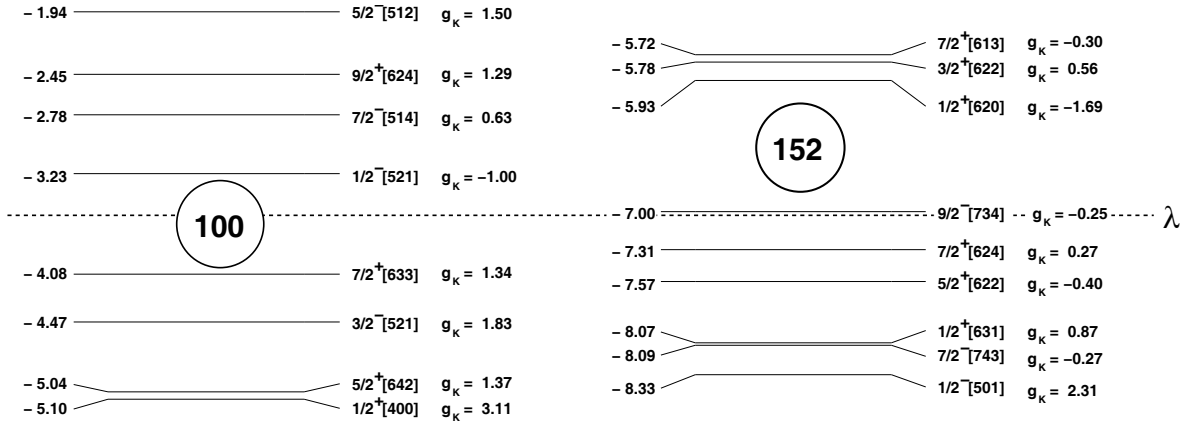Figure 5.10: Single-particle spectrum of ^{250}Fm calculated based on a Woods-Saxon potential using "universal" parameters and deformation parameters $\beta_2 = 0.247$, $\beta_4 = 0.035$ taken from [99].

drop corresponds to the largest peak in the isotonic chains of δ_{2p} values in Figure 5.9(b). A peak is present as well for $N = 154$, but vanishes for smaller neutron numbers below 152. Instead, the chains for $N = 150$ and $N = 148$ peak at $Z = 98$. The peaks agree well with the minima in the experimental 2^+ energies in Figure 5.6(a), especially with the chains for $N = 150$ and $N = 154$.

One should keep in mind that the data for the isotopic chains in Figure 5.6(b) is still sparse, and the chain for $N = 150$ is the only one containing five data points in a row, and a clear minimum. Note as well, that the shell gaps are not very pronounced, which makes it more difficult to draw conclusions. In order to make firm conclusions, more data is needed. Most beneficial would be data on ^{252}Fm, which would complete the fermium isotopic and $N = 152$ isotonic chain, and on ^{256}No, which could confirm a minimum at $N = 152$ in the nobelium chain, and continue the $N = 154$ isotonic chain to higher proton numbers.

5.4 The $K^\pi = 8^-$ Isomer in ^{250}Fm

In this section, two-quasiparticle excitations are calculated with a Woods-Saxon code. These are compared with predictions based on mean-field calculations using the Gogny D1S force performed by Delaroche *et al.*, and with the experimental results in terms of g_K values in order to find the right assignment.

5.4.1 Theoretical Prediction

The single-particle spectrum of ^{250}Fm is shown in Figure 5.10. It is calculated with the code WSBETA based on a Woods-Saxon potential [43]. The "universal" parametrisation has been used, with the deformation parameters $\beta_2 = 0.247$, $\beta_4 = 0.035$, and $\beta_6 = -0.047$ taken from [99]. The levels have been calculated with the experimental deformation $\beta_2 = 0.28$ for comparison, but the differences are negligible.

The energies, Nilsson assignments and g_K values of the single-particle levels are given in Figure 5.10. The Fermi energy λ is marked by a dashed line. Shell gaps open up at $Z = 100$
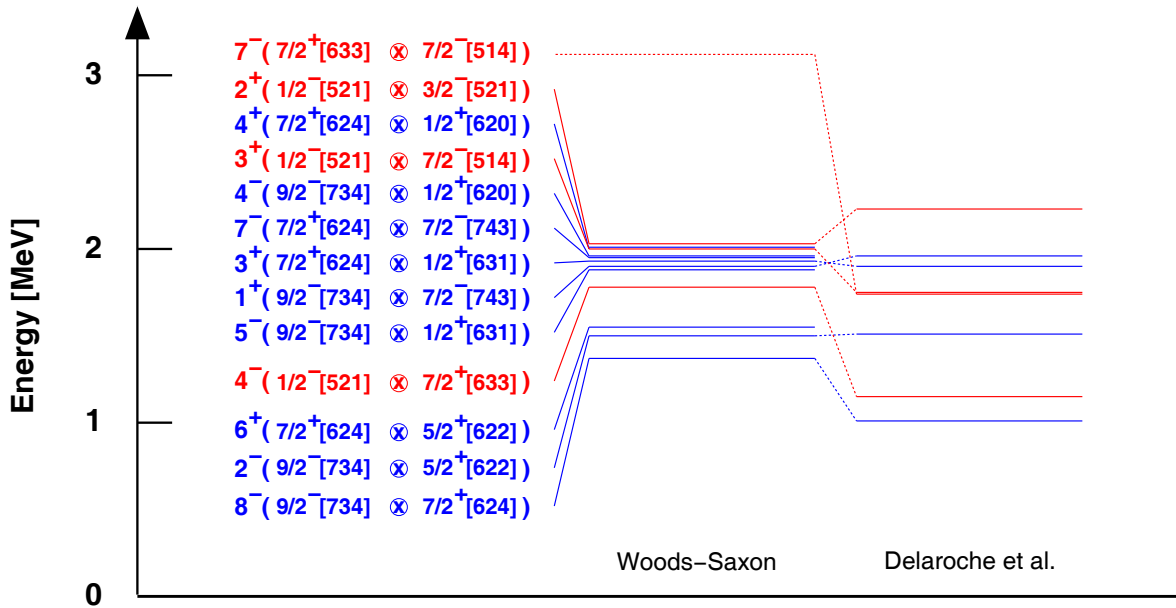
Figure 5.11: Two-quasiparticle excitations in ^{250}Fm calculated with the Woods-Saxon code (left side), and taken from Delaroche *et al.* [109] (right side). Neutron quasiparticle configurations are given in blue, proton quasiparticle configurations in red.

and $N = 152$. Due to the proton shell gap at $Z = 100$, the high-Ω single-particle levels for neutrons are closer to the Fermi surface than the ones for protons, and therefore low-lying neutron two-quasiparticle excitations may be expected.

From the single-particle spectrum, the two-quasiparticle excitations can be deduced. The energy is calculated taking into account the pairing gap Δ:

$$E_{2qp} = E_1^{qp} + E_2^{qp} = \sqrt{(\epsilon_1 - \lambda)^2 + \Delta^2} + \sqrt{(\epsilon_2 - \lambda)^2 + \Delta^2} \qquad (5.12)$$

Here, ϵ_ν is the single-particle energy, and λ the Fermi energy. The favoured spin is calculated using the Gallagher rules introduced in Section 2.5, and the parity is the product of the single-particle parities. A pairing gap energy is calculated using the five-point mass formula, see Equation 5.13. For neutrons, the pairing gap is $\Delta_n = 657$ keV, and for protons $\Delta_p = 784$ keV.

The calculated energies of two-quasiparticle configurations based on the Woods-Saxon calculation is shown in Figure 5.11. As expected, the neutron excitations lie lower in energy than the proton ones. The lowest two-quasiparticle excitation is a coupling of the $9/2^-[734]$ and $7/2^+[624]$ neutron levels to form a 8^- state. In the calculation using the Woods-Saxon code, the lowest two-quasiproton configuration with $K = 8$ is the one with $8^-(7/2^-[514]_\pi \otimes 9/2^+[624]_\pi)$, which is not shown in the figure. Besides this, no other low-lying excitation with $K = 8$ is present.

In the same figure, two-quasiparticle excitations from calculations performed by Delaroche *et al.* are given for comparison [109]. In this calculation, the Hartree-Fock Bogoliubov mean field method is used together with the Gogny D1S force. It is performed for heavy elements between thorium and nobelium. The figure contains the lowest four two-quasiparticle excitations for each neutrons and protons. The result supports the observation from the

Woods-Saxon calculation, that the 8^- state lies lowest in energy, and no state with same spin is available. Therefore, we propose the $K^\pi = 8^- (7/2^+[624]_\nu \otimes 9/2^-[734]_\nu)$ two-neutron configuration to be the band head of the isomeric band in ^{250}Fm.

Both calculations give a low-lying 2^- state from coupling of $9/2^-[734]$ and $5/2^+[622]$ neutrons, the former quasiparticle being the same as in the $K^\pi = 8^-$ state. This is the only low-lying level with $K = 2$, and we therefore propose this to be the dominating configuration of the intermediate octupole band.

5.4.2 Comparison of Experimental and Theoretical $B(M1)/B(E2)$ Ratios

A conclusive test of the two-quasiparticle excitation can be made by comparing calculated and experimental ratios of the reduced transition probabilities $B(M1)$ and $B(E2)$. $B(M1)$ can be calculated by Equation 2.50, containing the rotational and intrinsic nuclear g factors g_R and g_K. The intrinsic g factor g_K can be calculated from Equation 2.47 using the single-particle g_K values, which are given in Figure 5.10. The rotational g factor g_R is approximately Z/A, as explained in Section 2.4.2. The reduced transition probability $B(E2)$ is deduced from Equation 2.44. The electrical quadrupole moment Q_0 is almost constant over a wide range of nuclei around ^{254}No, as is seen from the very similar band structures in the low-spin part of the even-even nuclei, which point towards almost identical deformation. The quadrupole deformation parameter of $\beta_2 = 0.28$ is taken from the experimental work of Bastin *et al.* [13]. This gives an electric quadrupole moment of $Q_0 = 1265$ fm^2 by solving Equation 2.43.

The experimental transition probabilities are taken directly from the strength of the transitions corrected for efficiency. Absolute and reduced transition probabilities are related through Equation 2.15. Both $E2$ and $M1$ transitions are observed experimentally from decays of initial states with $I = 14, 15, 16$ in the $K = 8$ band, see Figure 4.11 and Table 4.5. In the $K = 2$ band, the decay from the $I = 7$ state occurs both through $M1$ and $E2$ transitions and gives a possibility to compare to theoretical values, as seen in Figure 4.8 and Table 4.3.

The configuration $8^- (7/2^+[624]_\nu \otimes 9/2^-[734]_\nu)$ with $g_K = -0.023$ is a first candidate for a possible K isomer in ^{250}Fm. It is lowest in energy for both calculations in Figure 5.11, it has a sufficiently high K value to be isomeric, and $K^\pi = 8^-$ matches the spectroscopic result in contrast to the other states in Figure 5.11. This is supported by calculations of Xu *et al.*, who give as an alternative the proton $7^- (7/2^+[633]_\pi \otimes 7/2^-[514]_\pi)$ configuration, which is ruled out by our spectroscopic results [110].

The $K^\pi = 8^-$ neutron configuration is compared to the $8^- (7/2^-[514]_\pi \otimes 9/2^+[624]_\pi)$ state with $g_K = 1.001$, which is the configuration for the K isomer found in ^{254}No, and the lowest proton two-quasiparticle excitation with $K^\pi = 8^-$ according to the Woods-Saxon calculations. Only the $2^- (5/2^+[622]_\nu \otimes 9/2^-[734]_\nu)$ is taken into account for the $K = 2$ intermediate state, which is by far the lowest state with $K^\pi = 2^-$ in both calculations in Figure 5.11.

The results are presented in Figure 5.12 and listed in Table 5.2. The experimental result gives clear evidence for the two-quasineutron configuration. In the figure, the data points are close to the calculations for this configuration. As can also be seen from the table, one point lies on the curve, while the other two are almost within 1σ of the calculated value. On the other hand, they differ by more than 2σ from the calculated values for the proton configuration.

The interpretation of the isomer as being a two-quasineutron excitation is also supported from the simulation presented in Figure 4.13. The simulation is based on the calculated $B(M1)/B(E2)$ ratios from Figure 5.12. The upper part of the simulation figure shows the
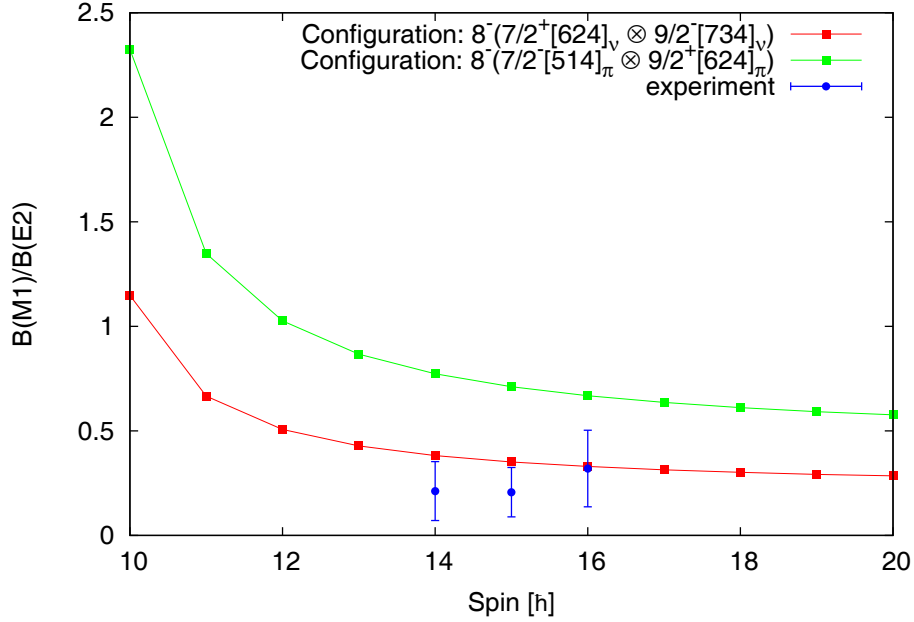
Figure 5.12: Comparison of experimental and calculated $B(M1)/B(E2)$ ratios in the $K^\pi = 8^-$ band. The red and green curves are calculated using g_K factors given by the Woods-Saxon code. The experimental values are calculated from the measured transition intensities.

initial state	$\left(\frac{\mathrm{B(M1)}}{\mathrm{B(E2)}}\right)_{\nu 8^-,\text{theory}}$	$\left(\frac{\mathrm{B(M1)}}{\mathrm{B(E2)}}\right)_{\pi 8^-,\text{theory}}$	$\left(\frac{\mathrm{B(M1)}}{\mathrm{B(E2)}}\right)_{\nu 2^-,\text{theory}}$	$\left(\frac{\mathrm{B(M1)}}{\mathrm{B(E2)}}\right)_{\text{exp}}$
16^-	0.330	0.668	-	0.3(2)
15^-	0.351	0.711	-	0.2(1)
14^-	0.382	0.773	-	0.2(1)
7^-	-	-	0.055	0.03(1)

Table 5.2: Comparison of theoretical to experimental $B(M1)/B(E2)$ values in the isomeric $K^\pi = 8^-$ and intermediate $K^\pi = 2^-$ bands. The theoretical values have been calculated assuming a neutron $8^-(7/2^+[624]_\nu \otimes 9/2^-[734]_\nu)$ and a proton $8^-(7/2^-[514]_\pi \otimes 9/2^+[624]_\pi)$ configuration, respectively, for the $K^\pi = 8^-$ isomer, and a neutron $2^-(5/2^+[622]_\nu \otimes 9/2^-[734]_\nu)$ for the intermediate state.

spectrum for the two-proton configuration. Here, $M1$ transitions contribute strongly to the spectrum, almost all of the transitions being at least as strong as the weak $E2$ ones. The strongest peak in the spectrum is even a $M1$ transition at $E_\gamma = 171$ keV. This prediction contradicts the experimental spectrum (see Figure 4.11), in which only three $M1$ transitions are weakly visible. The lower part of the simulation figure contains the two-neutron case. Here, the $M1$ transitions are much smaller, with the largest three at 171, 181, and 191 keV, and thus in agreement with experiment.

The comparison of experimental $B(M1)/B(E2)$ ratios to calculated ones is based on relatively low experimental statistics. The comparison to the simulation on the other hand is more qualitative than quantitative. In order to make a quantitative analysis with higher
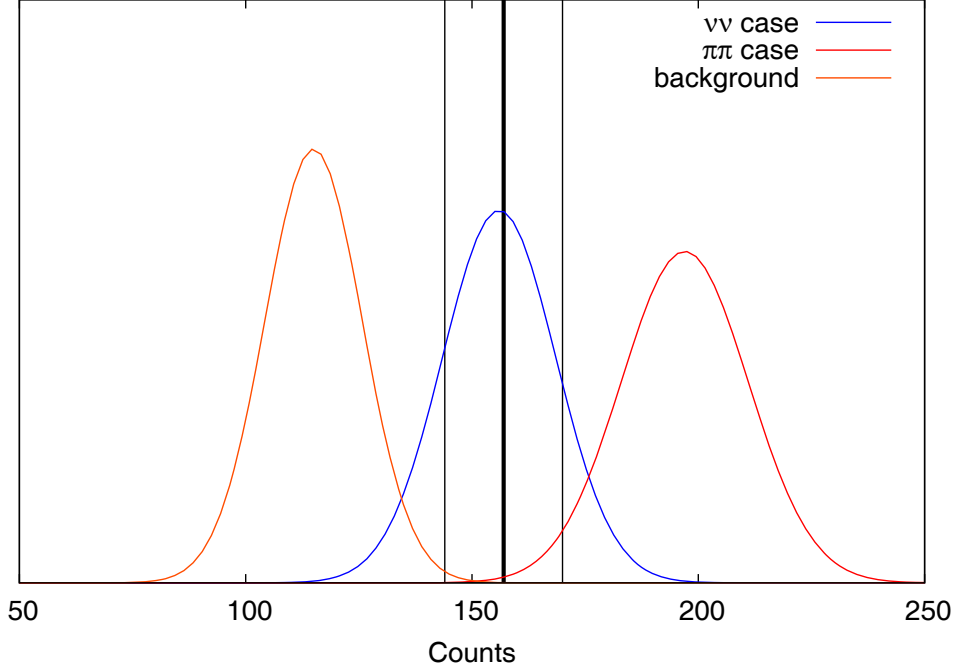
Figure 5.13: Comparison of the total number of counts in recoil-electron tagged γ spectrum between 165 and 215 keV to estimations based on the intensity of the $E2$ transitions assuming two-proton or two-neutron quasiparticle configuration for the $K = 8$ isomer. The number of counts in the spectrum is indicated by vertical lines, the measured background counts by an orange curve, the background plus $M1$ transition counts for the neutron case by a blue curve and for the proton case by a red curve.

statistics, the number of events in the region of $M1$ transitions can be added up and compared to what we would expect in the case of two-neutron or two-proton configurations, respectively. This is done in Figure 5.13 for the region of 165 keV to 215 keV. The orange curve represents the background, which is estimated based on events in the 165 to 215 keV interval, which are free from peaks. In the blue and red curve, the $M1$ transition strengths are added for peaks in this interval. They are calculated from the known $E2$ strength and $B(M1)/B(E2)$ ratios in Figure 5.12. The width of the Gaussians is defined by the square root of the number of counts. The total number of counts measured in the interval is marked in the figure by a vertical line. The uncertainty is calculated again as the square root of the number of counts.

The experimental value is positioned on top of the distribution representing the neutron-neutron case, and lies at the lower tail of the proton-case distribution. It thus agrees with the interpretation given above, that the band is built on top of a two-quasineutron excitation. Note though, that the background is difficult to measure, and very sensitive to the intervals from where it is taken. This can cause a systematic error, which is not taken into account in the error bars. Together with the measurement of single $B(M1)/B(E2)$ ratios, and the simulations, this gives strong support for an assignment of the isomer to the $8^-(7/2^+[624]_\nu \otimes 9/2^-[734]_\nu)$ two-neutron quasiparticle excitation.

Figure 5.14: Two-quasiparticle excitations in ^{248}Fm calculated with a Woods-Saxon code, and taken from Delaroche *et al.* [109].
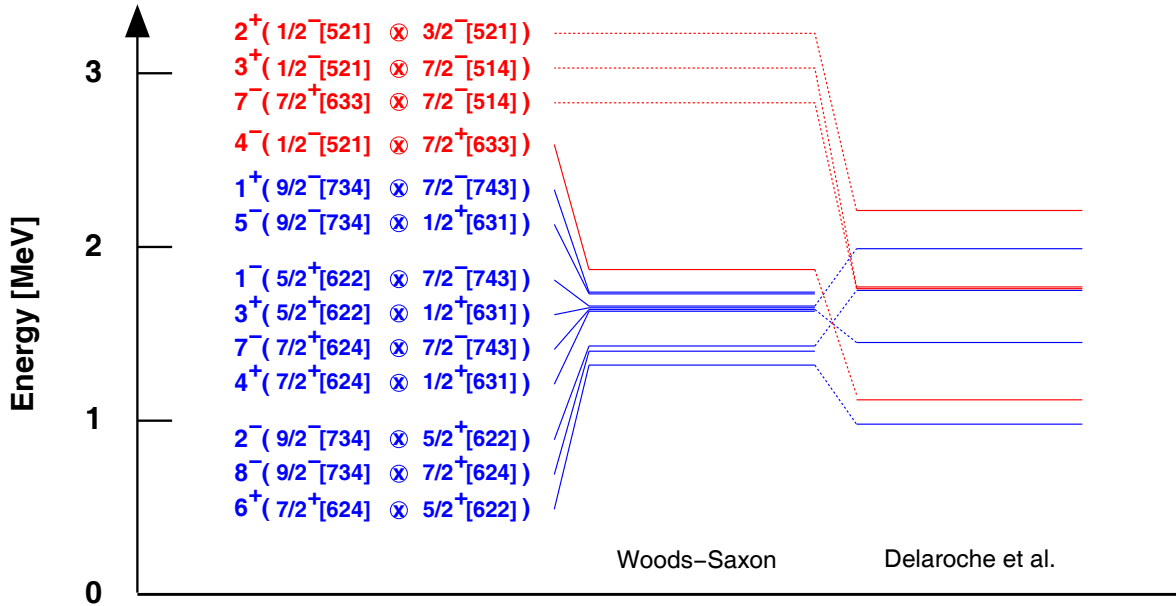
5.5 The K Isomer in ^{248}Fm

A firm assignment of the isomer in ^{248}Fm is not possible due to the low statistics, which did not allow the construction of its decay path. However, theory gives a few possibilities which can be discussed with help of the experimental results, and suggestions can be made.

As for ^{250}Fm, we calculate the two-quasiparticle excitation of ^{248}Fm with a code based on the Woods-Saxon single-particle potential. For this calculation, the single-particle spectrum for ^{248}Fm is almost identical to the one of ^{250}Fm presented in Figure 5.10. Since it has two neutrons less, the Fermi surface has to be lowered for neutrons below the $7/2^+$[624] Nilsson state. The ordering and spacing of the proton levels remain roughly the same. Again, we expect low-lying two-neutron excitations because of the proton gap at $Z = 100$. As the Fermi surface is moved between the $7/2^+$[624] and $5/2^+$[622] single-particle neutron levels, the $6^+(7/2^+[624]_\nu \otimes 5/2^+[622]_\nu)$ configuration is lowered below the $8^-(7/2^+[624]_\nu \otimes 9/2^-[734]_\nu)$ configuration, as is evident from Figure 5.14. This is supported by the calculation of Delaroche *et al.* drawn in the same figure. They calculated the lowest four two-quasineutron and -proton excitations. In their calculation, the $8^-(7/2^+[624]_\nu \otimes 9/2^-[734]_\nu)$ configuration is missing completely, while the $6^+(7/2^+[624]_\nu \otimes 5/2^+[622]_\nu)$ configuration is the lowest similar to the Woods-Saxon calculation. Besides these two, low-lying high-K excitations are calculated for $7^-(7/2^+[624]_\nu \otimes 7/2^-[743]_\nu)$, and $7^-(7/2^+[633]_\pi \otimes 7/2^-[514]_\pi)$ configurations, of which the former is seen in both, the latter only in the low-lying states calculated by Delaroche *et al.*

These configurations are compared in terms of reduced hindrance in Table 5.3. We assume $M1$ multipolarity for the $6^+ \to 6^+$ transition, and $E2$ multipolarity for the $7^- \to 6^+$ and $8^- \to 8^+$ transitions to the ground-state band. The reduced hindrance is calculated with two different assumptions for each configuration: In a first naive approach, the transition energy is fixed at 904 keV, which is the strongest line in the γ-ray spectrum. However, as we see a

Configuration	$6^+_{\nu\nu}$		$7^-_{\nu\nu}, 7^-_{\pi\pi}$		$8^-_{\nu\nu}$	
E_{trans}[keV]	904	760	904	760	904	540
$T_{1/2,WE}$ [fs]	27.3	38.8	0.23	0.388	0.23	1.08
f_ν	206	258	187	224	87	90

Table 5.3: Reduced hindrance f_ν for the four proposed configurations for the isomer of ^{248}Fm.

transition at 805 keV as well, there is a possibility that the isomer deexcites via an intermediate state. To take this into account, the excitation energy of the isomer is approximated by adding 904 keV to the maximum energy of the electrons, which are recorded in the DSSSD in coincidence to this transition, which is ≈ 180 keV. In the second approach, the transition energy is then calculated from the difference of this excitation energy of ≈ 1080 keV and the excitation of the 6^+ and 8^+ members of the ground-state band, respectively. Furthermore, similar to the case of ^{250}Fm, a branching of 20 % is assumed for direct deexcitation into the ground-state band.

The Weisskopf estimates for the half life, $T_{1/2,WE}$ can now be calculated using the transition multipolarity and energy. It is given in Table 5.3 and is used to deduce the hindrance factor f_ν with help of Equations 2.56.

It is obvious from the table, that the two approaches do not cause large deviations of the f_ν values. They lie around 200 for the 6^+ and 7^- configurations, slightly higher for 6^+ than for 7^-. Both values for the hindrance for 8^- on the other hand are around 90, close to the prediction by Löbner. Thus, from the point of view of hindrance factors, the $8^-_{\nu\nu}$ value is favoured. It should be noted, though, that f_ν values of 213 and 192 are derived for ^{250}Fm (see next Section and [35]). Other high-lying f_ν values are observed in other nuclei as well, as will be discussed in the next Section. Firm conclusions can therefore not be drawn from this method.

5.6   Systematics of K Isomers in the Region of ^{254}No

In the previous sections the isomers in ^{250}Fm and ^{248}Fm, and their possible assignment have been discussed. In recent years, many new isomers have been found in this region, which allows systematic studies of the assignments, energies and hindrances to be made.

A summary of K isomers in even-even nuclei in the vicinity of ^{248,250}Fm can be found in Table 5.4. The table gives spin and parity, half life, excitation energy and proposed assignments for each isomer. Most of them are populated in fusion-evaporation reactions, except for ^{244,246}Cm, which have been produced by β decay, ^{246,248}Cm by deep-inelastic reactions, and ^{256}Fm by transfer reactions. Assignments of ^{244,246,248}Cm, ^{250,256}Fm, and ^{252,254}No are based on the measured spin and parity, while the ones for ^{250}No, ^{256}Rf, ^{270}Ds, the second isomer in ^{254}No, and ^{248}Fm are tentative or not known. The assignments of ^{254}No and ^{250}Fm are supported by the measurements of $B(M1)/B(E2)$ ratios.

The excitation energies of the two-quasiparticle isomers lie between 1 and 1.5 MeV. The pairing gap energy can be calculated for comparison with help of the 5-point mass formula, which is for neutrons:

$$\Delta_n = -\frac{1}{8}\left[M(Z, N+2) - 4M(Z, N+1) + 6M(Z, N) - 4M(Z, N-1) + M(Z, N-2)\right]$$

(5.13)

Nucleus	K, I^π	$t^m_{1/2}$	E^* [MeV]	Proposed Configuration	Reference
^{244}Cm	$6, 6^+$	$34(2)$ms	1.042	$7/2^+[624]_\nu \otimes 5/2^+[622]_\nu$	[111, 112]
^{246}Cm	$8, 8^-$	$1.12(24)$s	1.180	$7/2^+[624]_\nu \otimes 9/2^-[734]_\nu$	[91, 113]
^{248}Cm	$8, 8^-$	$146(18)\mu$s	1.459		[113]
^{248}Fm	-	$10.1(6)$ms	-	-	this work
^{250}Fm	$8, 8^-$	$1.92(5)$s	1.198	$7/2^+[624]_\nu \otimes 9/2^-[734]_\nu$	[35],this work
^{256}Fm	$7, 7^-$	$70(5)$ns	1.425	$5/2^+[622]_\nu \otimes 9/2^+[725]_\nu,$	[101, 110]
				$7/2^-[514]_\pi \otimes 7/2^+[633]_\pi$	
^{250}No	$(6, 6^+)$	$43(20)\mu$s	-	$7/2^+[624]_\nu \otimes 5/2^+[622]_\nu$	[114]
^{252}No	$8, 8^-$	$109(6)$ms	1.255	$7/2^+[624]_\nu \otimes 9/2^-[734]_\nu$	[91, 115]
^{254}No	$8, 8^-$	$266(2)$ms	1.293	$9/2^+[624]_\pi \otimes 7/2^-[514]_\pi$	[21, 116]
^{254}No	-	$184(3)\mu$s	≥ 2.917	-	[21, 116–118]
^{256}Rf	-	$25(2)\mu$s	-	-	[119]
^{256}Rf	-	$17(2)\mu$s	-	-	[119]
^{256}Rf	-	$27(5)\mu$s	-	-	[119]
^{270}Ds	$(9, 9^-),$	$6.0^{+8.2}_{-2.2}$ ms	(1.13)	$11/2^-[725]_\nu \otimes 7/2^+[613]_\nu,$	[110, 120]
	$(10, 10^-)$			$11/2^-[725]_\nu \otimes 9/2^+[615]_\nu$	
	$(10, 10^-)$			$11/2^+[615]_\pi \otimes 9/2^-[505]_\pi$	

Table 5.4: Even-even K isomers observed in the vicinity of ^{248,250}Fm. Their spin and parity assignment, half-life, excitation energy, and configuration assignment are given in the following columns.

This gives a pairing gap energy of $\Delta_n = 657$ keV for ^{250}Fm. The excitation energy of a two-quasiparticle excitation is given by Equation 5.12 and is is of the order of twice the pairing gap energy, which agrees with the experimental excitation energies.

It is apparent, that all configurations have one partner with aligned spin projection Σ and angular momentum projection Λ, while the other one is antialigned. This is a consequence of the Gallagher rules in Equations 2.53 and 2.54. If one pair of Σ and Λ is aligned, the other antialigned, the two-quasiparticle excitation with $\Omega = \Omega_1 + \Omega_2$ is favoured, allowing low-energy high-K excitations to be formed. If on the other hand Σ and Λ are aligned or antialigned in both cases, the the two-quasiparticle excitation with $\Omega = |\Omega_1 - \Omega_2|$ will be lower in energy, and no low-lying high-K states are formed.

The relatively large amount of data allows the study of single-particle levels over a wide range. Several questions arise from the assignments of spin, parity and two-quasiparticle configurations:

- What happens between ^{254}No and ^{250}Fm, where the isomers are assigned two-proton and two-neutron excitations, respectively?

- How does the structure evolve for different isotonic chains?

- How well are changes and systematics explained and predicted by theory?

The assignment for ^{250}Fm was derived with the help of the single-particle spectrum in Figure 5.10. The two-neutron $K^\pi = 8^-$ assignment is explained by a gap in the proton spectrum at $Z = 100$ and the proximity of the $7/2^+[624]$ and $9/2^-[734]$ levels in the neutron spectrum. Note that no proton gap opens up at $Z = 100$ in most parametrisations of Hartree-Fock Bogoliubov-type mean-field calculations, but $Z = 98$ and 104 are favoured instead (see
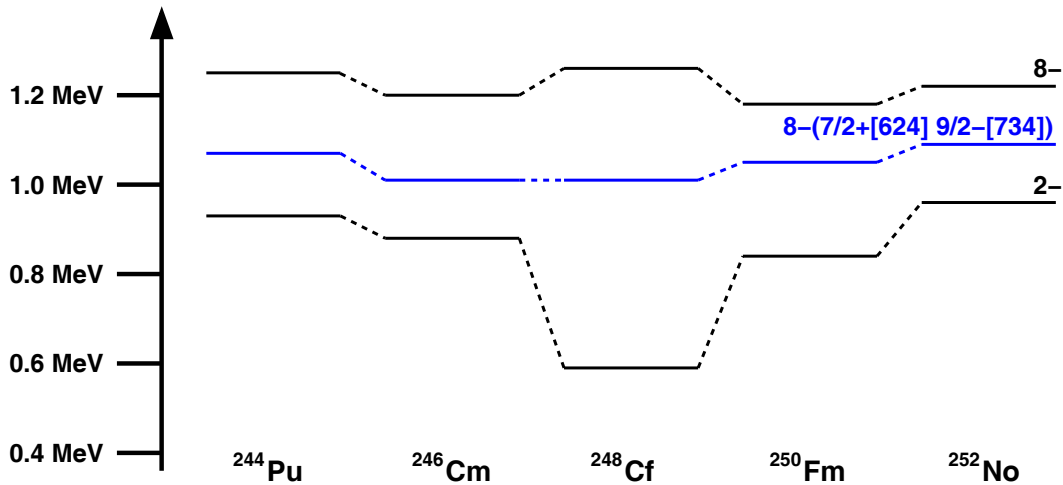
Figure 5.15: Energies of $K^\pi = 8^-$ and $K^\pi = 2^-$ states in $N = 150$ isotones (in black) in comparison to calculated $K^\pi = 8^-$ states by Delaroche *et al.* (in blue) [109]. The references for experimental data are: ^{244}Pu [122, 123], ^{246}Cm [91], ^{248}Cf [124, 125], ^{250}Fm [[35],this work], ^{252}No [91, 115].

for example [121]). ^{254}No has two protons and two neutrons more than ^{250}Fm. In the single-particle spectrum, the Fermi surface will move two nucleons up in both cases. It reaches the well-established deformed neutron shell at $N = 152$, which is known for example from fission half lives, see [106]. Any two-neutron excitation will thus lie high in energy. On the other hand, the proton levels at $9/2^+[624]$ and $7/2^-[514]$ get closer to the Fermi surface and can combine to form a low-energy high-K state, which is why this state is favoured.

The energy systematics of $K^\pi = 8^-$ isomers and $K^\pi = 2^-$ intermediate states is shown in Figure 5.15 for isotones with $N = 150$. The 8^- states form K isomers built on the $7/2^+[624]_\nu \otimes 9/2^-[734]_\nu$ two-neutron excitation. The 2^- states are assigned to octupole vibrational states with a main contribution from the two-neutron $5/2^+[622]_\nu \otimes 9/2^-[734]_\nu$ quasiparticle excitation (see [35, 91]). ^{244}Pu and ^{248}Cf are not listed as isomers in Table 5.4, as the half life has not been measured.

The $K^\pi = 8^-$ states form an impressively long chain of states with almost constant energy. This is strong evidence for the interpretation as two-neutron excitation, which is not affected by the change of proton number. The assignment as $8^-(7/2^+[624]_\nu \otimes 9/2^-[734]_\nu)$ is supported by calculations of Delaroche *et al.*, who predict the state to be almost constant over this chain of isotones [109]. Compared to the experimental values, the energies have an offset of approximately 200 keV. They are the lowest high-K two-quasiparticles for these nuclei in the calculation.

The energies of the 2^- states are constant as well, except for ^{248}Cf, where a pronounced minimum occurs. The state was first investigated by Yates *et al.*, who populated two bands with $K^\pi = 2^-$ at energies of 593 keV and 1477 keV. From agreement with cross-section calculations, it was deduced that both bands contain $2^-(5/2^+[622]_\nu \otimes 9/2^-[734]_\nu)$ components. As only one $K^\pi = 2^-$ state is expected below 2 MeV according to Yates *et al.*, the states are mixed with a 2^- octupole-vibrational component. Robinson *et al.* explained the exceptional low energy of 593 keV in ^{248}Cf by further mixing with a two-proton quasiparticle state, as the sudden change is seen in the isotones [91]. The $7/2^+[633]_\pi$ and $3/2^-[521]_\pi$ proton states are
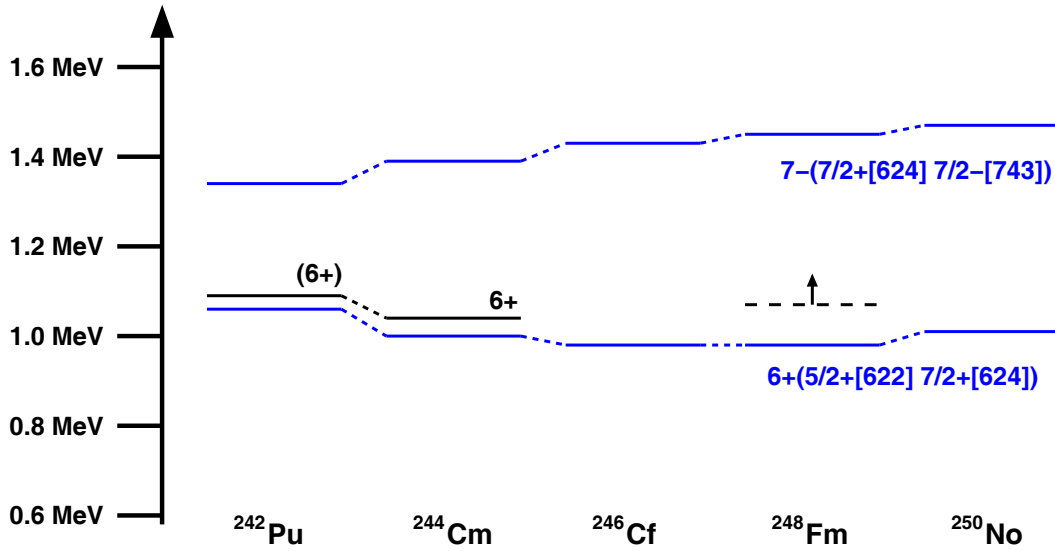
Figure 5.16: Energies of K isomers in $N = 148$ isotones (in black) in comparison to $6^+(7/2^+[624]_\nu \otimes 5/2^+[622]_\nu)$ and $7^-(7/2^+[624]_\nu \otimes 7/2^-[743]_\nu)$ states calculated by Delaroche *et al.* (in blue) [109]. The experimental energies and assignments of ^{242}Pu and ^{244}Cm are taken from [111, 127].

very close in energy, which is evident for example in the level scheme of ^{247}Bk extracted by Ahmad *et al.* [126]. Therefore, mixing with the two-quasiproton $2^-(7/2^+[633]_\pi \otimes 3/2^-[521]_\pi)$ excitation causes the drop in excitation energies in ^{248}Cf.

The energies of K isomers in isotones of ^{248}Fm are displayed in Figure 5.16. Experimental excitation energies have been measured only for ^{242}Pu and ^{244}Cm, and in this work, a minimum energy of 1070 keV is deduced for ^{248}Fm. An isomer was found as well in ^{250}No by Peterson *et al.* [114]. They identified two fission components, of which the one with a longer half life has a lower cross section, which was interpreted as a 30 % population of an isomeric state similar to ^{254}No and ^{250}Fm. An excitation energy could not be measured.

Peterson *et al.* performed a shell model calculation using the deformed Woods-Saxon model with universal parameters (see [114] and references therein) and deformation parameters of $\beta_2 = 0.235$, $\beta_4 = 0.032$ and $\beta_6 = -0.035$. The pairing correlations were treated using the Lipkin-Nogami prescription with fixed strength of $G_\pi = 24/A$ MeV and $G_\nu = 17.8/A$ MeV. A two-quasineutron $6^+(7/2^+[624]_\nu \otimes 5/2^+[622]_\nu)$ excitation was predicted at 1050 keV and tentatively assigned to the isomer in ^{250}No. This is identical to the proposed two-quasiparticle excitation in ^{244}Cm [111]. The isomer in ^{248}Fm is expected to have the same configuration and a similar excitation energy.

In the same Figure 5.16, the $6^+(7/2^+[624]_\nu \otimes 5/2^+[622]_\nu)$ and $7^-(7/2^+[624]_\nu \otimes 7/2^-[743]_\nu)$ two-quasiparticle excitations calculated by Delaroche *et al.* are presented for the isotonic chain between plutonium and nobelium [109]. They are the lowest-lying high-K two-quasiparticle excitations for these nuclei. The experimental 6^+ energies of ^{242}Pu and ^{244}Cm lie very close to the theoretical values. While the 6^+ energies remain constant in the whole isotonic chain, with an energy spread of only $\Delta E \approx 100$ keV, the 7^- energies increase monotonically from approximately 300 keV above the 6^+ state for ^{242}Pu, to almost 500 keV for ^{250}No. Therefore, based on the calculation, the isomer in ^{248}Fm can tentatively be assigned to the

Nucleus	$(K_i, I_i^+) \rightarrow (K_f, I_f^+)$	E_γ [keV]	Multipolarity	f_ν
^{244}Cm	$(6, 6^+) \rightarrow (0, 6^+)$	746	E2	206
^{246}Cm	$(8, 8^-) \rightarrow (0, 8^+)$	679	-	212 [113]
^{248}Cm	$(8, 8^-) \rightarrow (0, 8^+)$	953	-	56 [113]
^{250}Fm	$(8, 8^-) \rightarrow (0, 8^+)$	682.3	E1	212
^{250}Fm	$(8, 8^-) \rightarrow (2, 7^-)$	23	M1	193
^{256}Fm	$(7, 7^-) \rightarrow (0, 8^+)$	861.8	E1	30.2 [101]
^{256}Fm	$(7, 7^-) \rightarrow (0, 6^+)$	1092.9	E1	38.6 [101]
^{252}No	$(8, 8^-) \rightarrow (0, 8^+)$	709	E1	178
^{254}No	$(8, 8^-) \rightarrow (3, 7^-)$	53	E1	804
^{254}No	$(8, 8^-) \rightarrow (0, 8^+)$	778	E1	214

Table 5.5: f_ν values for K isomers in the region of the fermium isotopes. Furthermore, the initial and final states the energies of the transition, which depopulate the isomer, are given in the third and fourth column. If no reference is given, the f_ν values are extracted using the data found in references given in Table 5.4.

$6^+(7/2^+[624]_\nu \otimes 5/2^+[622]_\nu)$ two-quasiparticle excitation.

Reduced hindrance factors f_ν for the decay of K isomers in the region are presented in Table 5.4. These are the isotopes for which the decay path of the isomer could be fully determined. The results are partly calculated using the published decay scheme, partly taken directly from literature. The values can be roughly classified in three groups.

The first group contains isotopes with a reduced hindrance of clearly below 100, namely ^{248}Cm, and ^{256}Fm. These are lower than what is expected due to Löbner (see Equation 2.56). Hall *et al.* interpret the low values by admixtures of lower-K values to the $K^\pi = 7^-$ isomer in ^{256}Fm [101].

Isomers with a reduced hindrance of between 170 and 220 can be put into a second group. They are found in ^{244,246}Cm, ^{250}Fm, and ^{252,254}No. The isotopes ^{246}Cm, ^{250}Fm, and ^{252}No are members of the same isotonic chain with $N = 150$. As can be seen from Figure 5.15, the K isomers and 2^- states have the same assigned configuration, and their energies are very stable throughout the chain. Thus, similar hindrances can be expected. An exception to this is ^{248}Cf, which has a lowered 2^- state, as discussed above.

^{254}No is an exception, as f_ν for the decay into the intermediate $K^\pi = 3^-$ band is as high as 804. However, similar cases have been measured in other regions of the nuclear chart before, for example in ^{234}U [128].

From comparison with the isotones we can conclude, that ^{250}Fm fits well into the systematics. The stability of hindrance factors supports the interpretation of the similar structure of the isotones with $N = 150$. The large scatter of f_ν throughout the region demonstrates on the other hand, that level assignment in ^{248}Fm is not possible based on hindrance factors.

Chapter 6

Summary and Outlook

A spectroscopic investigation of the two transuranium isotopes ^{248,250}Fm has been made in this work. The ground-state band of ^{248}Fm could be established, and the ground-state band of ^{250}Fm has been extended up to spin $I^\pi = 20^+$, and tentatively up to 22^+. The energies of the rotational states of ^{250}Fm show an offset of approximately 0.5 keV compared to a preceding measurement by Bastin *et al.* [13], which persists after reanalysing and refitting of the data. With the help of the rotational energies, the ground-state deformation of ^{248}Fm has been measured and compared to nuclei in the region. The value of $\beta = 0.28(2)$ fits well into the systematics and supports the picture of stable deformation of nuclei in the vicinity of ^{254}No. The bands have been interpreted in terms of alignment of $i_{13/2}$ protons and $j_{15/2}$ neutrons, and in terms of the energies of the 2^+ states in the ground-state band. The 2^+ energies show a minimum at $N = 152$, which is caused by the reduced pairing energy at the position of the deformed shell gap at this neutron number. No such clear minimum is found for protons, where a deformed shell gap is predicted at $Z = 100$. Instead, a dip is seen at $Z = 98$ or $Z = 100$, depending on the neutron number N.

An 1.92(5) s isomer has been found in ^{250}Fm, and its decay path to the ground-state band has been established. The isomer is deduced to have the two-quasiparticle $8^- (7/2^+[624]_\nu \otimes 9/2^-[734]_\nu)$ configuration. 20 % of the decay of the isomeric state feeds directly into the ground-state band, while 80 % feeds a 2^- octupole band with a dominant $2^-(5/2^+[622]_\nu \otimes 9/2^-[734]_\nu)$ two-quasiparticle excitation. An $K^\pi = 8^-$ rotational band has been measured above the isomer. The two-quasiparticle assignment of the isomer has been unambiguously proven by comparison of calculated and measured B(M1)/B(E2) ratios of transitions in this band. The band is further studied in terms of moment of inertia. At low frequencies, $\mathscr{I}^{(1,2)}$ are higher for the isomeric than for the ground-state band, but increase with smaller slope, which is due to blocking effects of the unpaired nucleons.

An isomer has also been found in ^{248}Fm with a half life of 10.1(6) ms. The decay path could not be established due to lack of statistics. From the electron energy distribution and γ rays in the clover detector, a minimum excitation energy of 1075 keV has been deduced. Several possibilities are discussed for the assignment of this isomer with spin between 6 and 8.

The two-quasiparticle isomers in the proximity of the fermium region have been presented. The excitation energies of the isomeric states have been compared with their isotones with $N = 150$ and $N = 148$, and to theoretical predictions. While the energy of the isomeric 8^- state is remarkably constant for the $N = 150$ isotones, the energy of the 2^- intermediate state

has a clear minimum at ^{248}Cf. A possible explanation is a proton $2^-(7/2^+[633]_\pi \otimes 3/2^-[521]_\pi)$ two-quasiparticle excitation, which comes down in energy and mixes with the octupole state at $Z = 98$. The systematics of the $N = 148$ isotones suggests a $6^+(7/2^+[624]_\nu \otimes 5/2^+[622]_\nu)$ configuration for the isomer in ^{248}Fm.

The results of the two fermium isotopes add to the experimental data, which has been collected in the region of ^{254}No in recent years. Systematic data on K isomers and rotational bands give a basis for future calculations in this region, with the aim of explaining the properties of heavy and superheavy elements and prediction of the long-sought island of stability. In this respect it is beneficial to have data on the same levels in chains of isotones and isotopes.

In the case of the 2^+ energy of the ground-state band, data on ^{252}Fm would complete the isotonic chain of $N = 152$, and clarify the position of the deformed proton shell gap. The isotopic chain for fermium would benefit from data of this isotope, as it is the only missing one at $N = 152$ in chains from curium to nobelium, and could give further proof for the shell gap at this position. Knowledge of the ground-state band of ^{250}No could provide a test, if the anomalous rise of the 2^+ energy of the light fermium isotopes persists in the nobelium isotopes. Both nuclei would also give useful complementary data for the systematic study of the alignment in the nobelium region.

An impressive chain of data for the 2^- octupole states and $K = 8$ isomers is available for the $N = 150$ isotones. In four of the five isotones of $N = 148$ in Figure 5.16, isomers have been measured as well. But only one of the measurements give a firm assignment of spin and energy, the other ones need a remeasurement. This includes ^{248}Fm from this work, and again ^{250}No.

Both ^{252}Fm and ^{250}No are difficult cases to study, as there is no projectile-target combination available, which provides sufficiently large fusion-evaporation cross sections. Especially for in-beam studies, this is crucial, as the germanium detectors are limited in count rate, which is in the case of JuroGam 10 kHz per detector. This limits the beam current, as the count rate is mainly due to instantaneous fission of the compound system and transfer reactions, which are independent of the fusion cross section. However, new developements in in-beam spectroscopy will raise this limit. The new setup JuroGamii in Jyväskylä was comissioned in 2008. It consists of 24 clover and 15 Phase 1 germanium detectors and is equipped with digital electronics, which improves the count-rate limit to approximately 40 kHz per detector, thus allowing a much increased beam current. JuroGamii is expected to be able to detect nuclei from fusion-evaporation reactions with cross sections as low as a few nanobarn. As a proof of principle, the rotational band of ^{246}Fm could be measured in December 2009 with a reaction cross section of approximately 15 nb [27, 129]. The production cross-section of two fission components of ^{250}No was reported to be 12^{+18}_{-4} nb and 5^{+3}_{-2} nb [114], which is thus in the range of the new setup.

Next generation germanium detector arrays are AGATA in Europe and GRETA in the United States. They use the principle of gamma-ray tracking, which works completely without Compton suppression, thus increasing the solid angle covered by the germanium detectors. The scattered single γ rays are tracked down in order to get full photopeak energy. The final AGATA array will have an efficiency of 43 % at 1.3 MeV (JuroGam: 4.2 %) [130].

The assignment of the $K = 8$ isomer in ^{250}Fm is based on relatively low statistics for the M1 transitions. The in-beam spectrometer SAGE combines the highly-efficient γ-detector array JuroGamii with a conversion-electron spectrometer. In the case of ^{250}Fm, the setup will allow the electrons of the highly converted M1 transitions in coincidence with the γ rays to be measured, and enable B(M1)/B(E2) ratio measurements on much improved statistics.

Bibliography

[1] M. G. Mayer, Phys. Rev. **75**, 1969 (1949).

[2] O. Haxel, J. H. D. Jensen, and H. E. Suess, Phys. Rev. **75**, 1766 (1949).

[3] M. Goeppert-Mayer, nobel prize lecture 1963.

[4] M. Bender, W. Nazarewicz, and P.-G. Reinhard, Phys. Lett. B **515**, 42 (2001).

[5] S. Ćwiok *et al.*, Nucl. Phys. A **611**, 211 (1996).

[6] K. Rutz *et al.*, Phys. Rev. C **56**, 238 (1997).

[7] M. Bender *et al.*, Phys. Rev. C **60**, 034304 (1999).

[8] S. G. Nilsson and I. Ragnarsson, *Shapes and Shells in Nuclear Structure*, first paperback ed. (Cambridge University Press, Cambridge, 2005).

[9] Y. T. Oganessian *et al.*, Phys. Rev. C **74**, 044602 (2006).

[10] Y. T. Oganessian *et al.*, Phys. Rev. Lett. **104**, 142502 (2010).

[11] S. Cwiok, P.-H. Heenen, and W. Nazarewicz, Nature **433**, 705 (2005).

[12] R. Firestone *et al.*, *Table of Isotopes*, eigth ed. (John Wiley & Sons, New York, 1996).

[13] J. Bastin *et al.*, Physical Review C **73**, 024308 (2006).

[14] P. Reiter *et al.*, Phys. Rev. Lett. **82**, 509 (1999).

[15] R.-D. Herzberg *et al.*, Phys. Rev. C **65**, 014303 (2001).

[16] A. Chatillon *et al.*, Eur. Phys. J. A **30**, 397 (2006).

[17] K. Hauschild *et al.*, Phys. Rev. C **78**, 021302 (2008).

[18] A. Ghiorso, K. Eskola, P. Eskola, and M. Nurmia, Phys. Rev. C **7**, 2032 (1973).

[19] P. Butler *et al.*, Acta Physica Polonica B **34**, 2107 (2003).

[20] G. Mukherjee *et al.*, AIP Conference Proceedings **764**, 243 (2005).

[21] R.-D. Herzberg *et al.*, Nature **442**, 896 (2006).

[22] M. Leino *et al.*, Eur. Phys. J. A **6**, 63 (1999).

[23] A. Chatillon *et al.*, Phys. Rev. Lett. **98**, 132503 (2007).

[24] P. Reiter *et al.*, Phys. Rev. Lett. **95**, 032501 (2005).

[25] R. D. Herzberg *et al.*, Eur. Phys. J. A **42**, 333 (2009).

[26] S. Ketelhut *et al.*, Phys. Rev. Lett. **102**, 212501 (2009).

[27] J. Piot *et al.*, to be published.

[28] T. Ishii *et al.*, Phys. Rev. C **76**, 011303 (2007).

[29] T. Ishii *et al.*, Phys. Rev. C **72**, 021301 (2005).

[30] H. Makii *et al.*, Phys. Rev. C **76**, 061301 (2007).

[31] T. Ishii *et al.*, Journal of the Physical Society of Japan **75**, 043201 (2006).

[32] R. Takahashi *et al.*, Phys. Rev. C **81**, 057303 (2010).

[33] K. Abu Saleem *et al.*, Phys. Rev. C **70**, 024310 (2004).

[34] G. Hackman *et al.*, Phys. Rev. C **57**, R1056 (1998).

[35] P. T. Greenlees *et al.*, Phys. Rev. C **78**, 021303 (2008).

[36] T. Mayer-Kuckuk, *Kernphysik - Eine Einführung*, seventh ed. (B.G. Teubner, Stuttgart/Leipzig/Wiesbaden, 2002).

[37] K. Heyde, *Basic Ideas and Concepts in Nuclear Physics*, 3rd ed. (Institute of Physics Publishing, Bristol and Philadelphia, 2004).

[38] R. Casten, *Nuclear Structure from a Simple Perspective*, 2nd ed. (Oxford University Press, Oxford, 2005).

[39] C. Amsler *et al.*, Physics Letters B **667**, 1 (2008), review of Particle Physics.

[40] T. Bengtsson and I. Ragnarsson, Nuclear Physics A **436**, 14 (1985).

[41] S. Nilsson, Dan. Mat. Fys. Medd. **29**, 16 (1955).

[42] B. Nilsson, Nuclear Physics A **129**, 445 (1969).

[43] S. Ćwiok *et al.*, Computer Physics Communications **46**, 379 (1987).

[44] V. Strutinsky, Nuclear Physics A **95**, 420 (1967).

[45] T. Kibédi *et al.*, Nuclear Instruments and Methods in Physics Research Section A: Accelerators, Spectrometers, Detectors and Associated Equipment **589**, 202 (2008).

[46] BrIcc v2.2b: Conversion Coefficient Calculator.
http://physics.anu.edu.au/nuclear/bricc/.

[47] ENSDF Isotope Explorer version 3.0 b1.
http://ie.lbl.gov/ensdf/.

[48] A. Bohr, B. Mottelson, and D. Pines, Physical Review **110**, 936 (1958).

[49] S. Belyaev, Dan. Mat. Fys. Medd. **31**, 11 (1959).

[50] A. Davydov and A. Chaban, Nuclear Physics **20**, 499 (1960).

[51] R. Diamond, F. Stephens, and W. Swiatecki, Physics Letters **11**, 315 (1964).

[52] S. Harris, Physical Review **138**, B 509 (1965).

[53] M. Mariscotti, G. Scharff-Goldhaber, and B. Buck, Physical Review **178**, 1864 (1969).

[54] P. Walker and G. Dracoulis, Nature **399**, 35 (1999).

[55] C. Gallagher, Physical Review **126**, 1525 (1962).

[56] K. Löbner, Physics Letters **26B**, 369 (1968).

[57] P. Fröbrich and R. Lipperheide, *Theory of Nuclear Reactions* (Oxford University Press, Oxford, 1996).

[58] R. Bass, Nuclear Physics A **231**, 45 (1974).

[59] H. Gäggeler *et al.*, Nuclear Physics A **502**, 561c (1989).

[60] P. Nolan, Nuclear Physics A **520**, 657c (1990).

[61] C. Beausang *et al.*, Nuclear Instruments and Methods in Physics Research A **313**, 37 (1992).

[62] D. Bazzacco, in *Proc. Int. Conf. Nuclear Structure at High Angular Momentum, Ottawa, May 1992* (AECL research, Chalk River, 1992), Vol. 2, p. 376.

[63] C. N. Davids *et al.*, Nuclear Instruments and Methods in Physics Research Section B: Beam Interactions with Materials and Atoms **70**, 358 (1992).

[64] M. Leino, Nuclear Instruments and Methods in Physics Research B **204**, 129 (2003).

[65] M. Leino, Nuclear Instruments and Methods in Physics Research B **99**, 653 (1995).

[66] R. Page *et al.*, Nuclear Instruments and Methods in Physics Research B **204**, 634 (2003).

[67] M. G. Itkis, Y. T. Oganessian, and V. I. Zagrebaev, Phys. Rev. C **65**, 044602 (2002).

[68] G. Jones, Nuclear Instruments and Methods in Physics Research A **488**, 471 (2002).

[69] I. Lazarus *et al.*, IEEE Trans. Nucl. Sci. **48**, 567 (2001).

[70] P. Rahkila, Nuclear Instruments and Methods in Physics Research A **595**, 637 (2008).

[71] A. Artna-Cohen, Nuclear Data Sheets **79**, 1 (1996).

[72] S. Rab, Nuclear Data Sheets **75**, 491 (1995).

[73] A. Andreyev *et al.*, Nuclear Instruments and Methods in Physics Research Section A **533**, 422 (2004).

[74] Geant detector Simulation Tool, CERN (1993)
http://wwwinfo.cern.ch/asd/geant.

[75] A. Ghiorso *et al.*, Phys. Rev. **99**, 1048 (1955).

[76] H. Atterling *et al.*, Phys. Rev. **95**, 585 (1954).

[77] G. N. Akap'ev *et al.*, Soviet Journal of Atomic Energy **21**, 908 (1966).

[78] S. Amiel *et al.*, Phys. Rev. **106**, 553 (1957).

[79] Y. A. Lazarev *et al.*, Physica Scripta **39**, 422 (1989).

[80] M. Nurmia, T. Sikkeland, R. Silva, and A. Ghiorso, Physics Letters B **26**, 78 (1967).

[81] A. N. Andreyev *et al.*, Zeitschrift für Physik A **345**, 389 (1993).

[82] A. Druin, N. Skobelev, and V. Rud, Soviet Journal of Nuclear Physics **12**, 24 (1966).

[83] S. Chu, L. Ekström, and R. Firestone, www Table of Radioactive Isotopes, database
version 2/28/1999
http://nucleardata.nuclear.lu.se/nucleardata/toi/.

[84] F. Kondev, Nuclear Data Sheets **105**, 1 (2005).

[85] G. Alaga, K. Alder, A. Bohr, and B. Mottelson, Dan. Mat. Fys. Medd. **29**, 9 (1955).

[86] M. S. Freedman *et al.*, Phys. Rev. C **15**, 760 (1977).

[87] T. Sikkeland, A. Ghiorso, J. Maly, and J. Nurmia, Physics Letters B **24**, 333 (1967).

[88] C. S. Wu *et al.*, Phys. Rev. C **45**, 261 (1992).

[89] P. Holmberg and P. O. Lipas, Nuclear Physics A **117**, 552 (1968).

[90] S. Eeckhaudt *et al.*, Eur. Phys. J. A **26**, 227 (2005).

[91] A. P. Robinson *et al.*, Phys. Rev. C **78**, 034308 (2008).

[92] R. D. Humphreys *et al.*, Phys. Rev. C **69**, 064324 (2004).

[93] T. Duguet, P. Bonche, and P. H. Heenen, Nuclear Physics A **679**, 427 (2001).

[94] M. Bender, P. Bonche, T. Duguet, and P. H. Heenen, Nuclear Physics A **723**, 354
(2003).

[95] H. Laftchiev, D. Samsœn, P. Quentin, and J. Piperova, Eur. Phys. J. A **12**, 155 (2001).

[96] L. Grodzins, Physics Letters **2**, 88 (1962).

[97] S. Raman, C. W. Nestor, S. Kahane, and K. H. Bhatt, Atomic Data and Nuclear Data
Tables **42**, 1 (1989).

[98] S. Raman *et al.*, Atomic Data and Nuclear Data Tables **36**, 1 (1987).

[99] S. Cwiok, S. Hofmann, and W. Nazarewicz, Nuclear Physics A **573**, 356 (1994).

[100] Y. A. Akovali, Nuclear Data Sheets **94**, 131 (2001).

[101] H. L. Hall *et al.*, Phys. Rev. C **39**, 1866 (1989).

[102] Y. A. Akovali, Nuclear Data Sheets **87**, 249 (1999).

[103] A. Artna-Cohen, Nuclear Data Sheets **84**, 901 (1998).

[104] Y. A. Akovali, Nuclear Data Sheets **99**, 197 (2003).

[105] Y. A. Akovali, Nuclear Data Sheets **96**, 177 (2002).

[106] F. P. Heßberger *et al.*, Zeitschrift für Physik A **359**, 415 (1997).

[107] A. Sobiczewski, I. Muntian, and Z. Patyk, Phys. Rev. C **63**, 034306 (2001).

[108] G. Audi, A. H. Wapstra, and C. Thibault, Nuclear Physics A **729**, 337 (2003), the 2003 NUBASE and Atomic Mass Evaluations.

[109] J.-P. Delaroche, M. Girod, H. Goutte, and J. Libert, Nuclear Physics A **771**, 103 (2006).

[110] F. R. Xu, E. G. Zhao, R. Wyss, and P. M. Walker, Phys. Rev. Lett. **92**, 252501 (2004).

[111] S. Vandenbosch and P. Day, Nuclear Physics **30**, 177 (1961).

[112] P. Hansen, K. Wilsky, C. Baba, and S. Vandenbosch, Nuclear Physics **45**, 410 (1963).

[113] S. K. Tandel, private communication.

[114] D. Peterson *et al.*, Phys. Rev. C **74**, 014316 (2006).

[115] B. Sulignano *et al.*, Eur. Phys. J. A **33**, 327 (2007).

[116] S. K. Tandel *et al.*, Phys. Rev. Lett. **97**, 082502 (2006).

[117] F. P. Heßberger *et al.*, Eur. Phys. J. A **43**, 55 (2010).

[118] R. Clark *et al.*, Physics Letters B **690**, 19 (2010).

[119] H. B. Jeppesen *et al.*, Phys. Rev. C **79**, 031303 (2009).

[120] S. Hofmann *et al.*, Eur. Phys. J. A **10**, 5 (2001).

[121] A. V. Afanasjev *et al.*, Phys. Rev. C **67**, 024309 (2003).

[122] R. C. Thompson, J. R. Huizenga, and T. W. Elze, Phys. Rev. C **12**, 1227 (1975).

[123] K. J. Moody *et al.*, Zeitschrift für Physik A Hadrons and Nuclei **328**, 417 (1987), 10.1007/BF01289627.

[124] S. W. Yates *et al.*, Phys. Rev. C **12**, 442 (1975).

[125] K. Katori, I. Ahmad, and A. M. Friedman, Phys. Rev. C **78**, 014301 (2008).

[126] I. Ahmad *et al.*, Phys. Rev. C **71**, 054305 (2005).

[127] E.-M. Franz, S. Katcoff, P. P. Parekh, and L. K. Peker, Phys. Rev. C **23**, 2234 (1981).

[128] S. Bjørnholm *et al.*, Nuclear Physics A **118**, 261 (1968).

[129] M. Venhart, to be published.

[130] AGATA technical design report, 2008.